ALMA MATER STUDIORUM · UNIVERSITY OF BOLOGNA

School of Science
Department of Physics and Astronomy
Master Degree in Physics

Measurement of the $WbWb$ differential cross-section in the dilepton channel with the ATLAS detector at $\sqrt{s}$ =13 TeV

Supervisor:
Chiar.mo Prof. Maximiliano Sioli

Co-supervisors:
Dr. Marino Romano
Dr. Gianluca Bianco

Submitted by:
Mario Orlando Franco

Academic Year 2022/2023

A mia madre e Gilda, per averlo reso possibile

Success is going from failure to failure without losing enthusiasm - Winston Churchill

Il tetto si è bruciato, ora posso vedere la luna - Misuta Masahide

Abstract

In this thesis, a measurement of the inclusive $WbWb$ differential cross section is provided as a function of some basic kinematic variables, making use of the full ATLAS Run-2 dataset at $\sqrt{s} = 13$ TeV and 139 fb^{-1} integrated luminosity. The measurement is performed in the dilepton channel, considering opposite sign (OS) $e\mu$ final states with at least two b-jets. The result will allow to assess and tune new Monte Carlo generators performances. These measurements are required in order to ensure that basic kinematics in the event and the interference effect between $t\bar{t}$ at LO and tW at NLO are properly modelled.

Contents

Introduction

The top quark is one of the fundamental building blocks of the Standard Model (SM) of particle physics and the heaviest known elementary particle. Following its first observation, performed by the CFD and $D\emptyset$ [1, 2] collaborations at the Tevatron proton-antiproton collider at Fermilab, in 1995, the top quark properties have been studied in depth by experiments at the Large Hadron Collider (LHC) at CERN, since 2009, where a larger sample of top quark events has become available for measurements with an unprecedented precision. Indeed, thanks to the high cross-section for top quark production at a centre-of-mass energy of 13 TeV, LHC is considered a "top-factory". Top quark production takes place, at LHC, primarily via gluon-gluon fusion into $t\bar{t}$ pairs. In addition, single-top production is also possible, in three channels: the t-channel, the s-channel and the associated tW production channel.

An in depth knowledge of the top quark properties is of paramount importance for both Beyond Standard Model (BSM) searches and precision physics measurements, where processes involving top quark production and decay are often present as a major background source. To this purpose, the study of the $WbWb$ production mechanism is of particular interest, as it also provides a window to study the effects of the quantum interference between the $t\bar{t}$, and tW production at NLO. In fact, since the two share the same $WbWb$ final state, an accurate description of it and its production differential cross-section measurement are required to take into account both contributions, as well as the effect of interference between them. So far, the available measurement of the $WbWb$ differential cross section, performed by the ATLAS collaboration [3] , were provided as a function of variables explicitly sensitive to the aforementioned interference effects, in particular the m_{bl}^{minimax} variable.

The present thesis work aims to provide a measurement of the differential cross section with the requirement of a total number of final-state b-jets equal or greater than two, in the $WbWb$ phase space, as a function of basic kinematic observable (lepton transverse momentum, jet transverse momentum, number of extra jets and leptons invariant mass). The results presented correspond to the normalised differential cross section. The motivation for this choice relies on the fact that many of the systematic uncertainties considered have a small effect on the shape of the distribution, and can be cancelled by taking the ratio $\frac{1}{\sigma}\frac{\mathrm{d}\sigma}{\mathrm{d}X}$. The measurement make use the full dataset collected by the ATLAS experiment during the period of Run-2 operations (2015-2018), for a centre-of-mass energy $\sqrt{s} = 13$ TeV and a luminosity of 139 fb^{-1}. Moreover, the dilepton opposite sign (OS) $e\mu$ channel is explicitly investigated, corresponding to the process $pp \to l^+l^-\nu\bar{\nu}b\bar{b}$. This particular choice allows to strongly suppress the $Z \to ll$ background. The measurement of the differential cross section can be used in order to assess and tune new Monte Carlo generators performances.

The general structure of this thesis can be so summarized:

- *Chapter* 1 provides an overview of the physical foundations and introduces the $WbWb$ production, together with all the contributions to this process which have to be taken into account when performing the measurement of the differential cross section. The final part of this chapter is devoted to a brief overview of the state-of-art of the measurement;
- *Chapter 2* describes the general functioning of the LHC and the ATLAS detector and its individual constituting sub-detectors;
- *Chapter 3* introduces how the process of object reconstruction is realized by the ATLAS collaboration. In this chapter, all and only the object of interest for the analysis carried on are explicitly considered: electrons, muons and jets. A particular section is dedicated the b-tagging procedure.
- *Chapter 4* provides a complete description of the dataset considered, the Monte Carlo (MC) samples, the background sources and selection criteria adopted in the analysis. Lastly, the control plots for a comparison between data and available simulation are shown;
- *Chapter 5* : The full analysis strategy is presented in this chapter. First, the procedure applied for the measurement of the differential cross-section is introduced. Then, the tests performed in order to validate such procedure are discussed, with their relative results. The uncertainties considered in the measurement are then presented, followed by the complete overview of the results obtained;
- *Conclusions*: contains a discussion of the results, the final considerations and the future outlook of the measurement;

Chapter 1

Physics fundamenta

1.1 The Standard Model of Particle Physics

Our present understanding of the structure of matter at the fundamental or *elementary* level is based on the *Standard Model of Particle Physics* (SM).
The SM provides a description based on three generations of spin 1/2 particles (*fermions*) constituted by *leptons* :

$$\begin{pmatrix} e \\ \nu_e \end{pmatrix}, \begin{pmatrix} \mu \\ \nu_\mu \end{pmatrix}, \begin{pmatrix} \tau \\ \nu_\tau \end{pmatrix} \tag{1.1}$$

and *quarks* :

$$\begin{pmatrix} u \\ d \end{pmatrix}, \begin{pmatrix} c \\ s \end{pmatrix}, \begin{pmatrix} t \\ b \end{pmatrix} \tag{1.2}$$

These particles interact among each-other via the exchange of *gauge bosons* of *fun-*

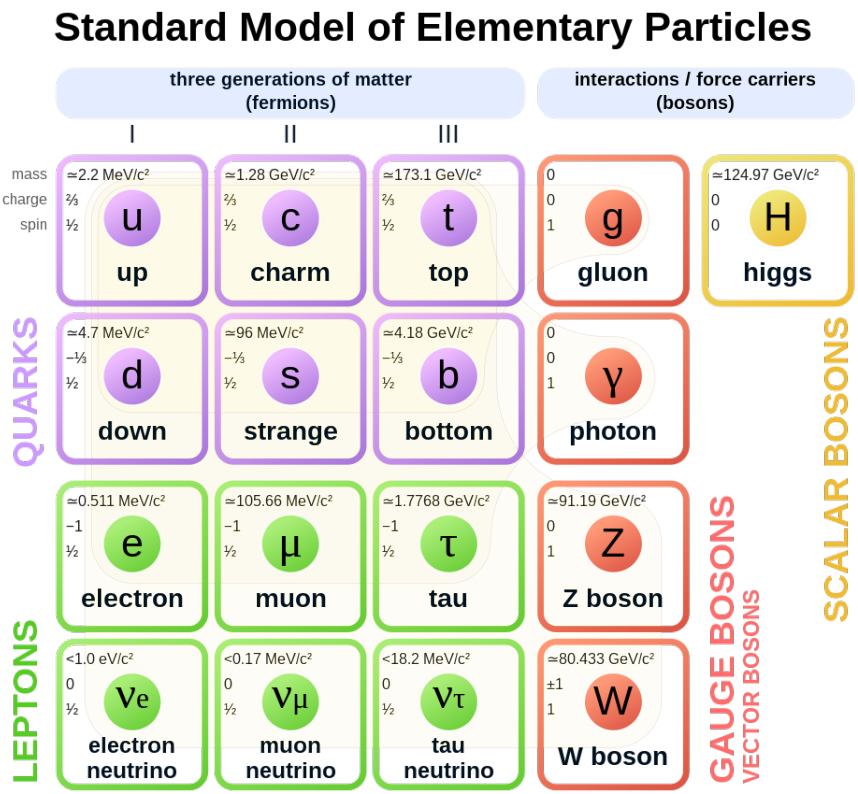

Figure 1.1: Fundamental particles of the SM.

damental forces. The SM of particle physics provides a description of only three out of the four fundamental interactions : the strong force, electromagnetism and the weak force (gravitation is excluded).
The properties of the gauge bosons are shown in table 1.1, where for completeness the Graviton was included, while in figure 1.1, a summary of SM particles is shown.

Quarks carry a strong interaction charge, called *color*, whereas the leptons are colorless. Moreover, quarks are characterized by a fractional electric charge of value +2/3 for the up-type quarks (u, c, t) and -1/3 for the down-type quarks (d, s, b). All the twelve particles undergo weak force interactions.

Table 1.1: Summary of gauge boson properties for the four fundamental interactions. Gravity is not described in the framework of the SM, the graviton inclusion is only for completeness sake.

Interaction	Boson	Symbol	Spin	Mass (GeV/c^2)
Electromagnetism	Photon (1)	γ	1	0
Strong	Gluon (8)	g	1	0
Weak	Ws and Z (3)	W^+, W^-	1	80.377$\pm$ 0.012 [4]
		Z	1	91.1876$\pm$0.0021 [4]
Gravity	Graviton (1)	G	2	0

For each of the fundamental fermions, a corresponding *anti*-fermion exists and is characterized by the same mass and opposite charge. Thus, taking into account the three possible quark colours, together with the gauge bosons and the Higgs boson, we have a total number of 61 fundamental particles.

Formally, the SM is a *Quantum Field Theory* (QFT) possessing a

$$\mathrm{SU(3)_c} \otimes \mathrm{SU(2)_L} \otimes \mathrm{U(1)_Y}$$

gauge symmetry, with c standing for the colour charge, L for left-handed and Y the hypercharge.

1.1.1 QED

There is a profound connection between interactions and symmetries: particle interactions can be derived as the result of *invariance* under *local* gauge transformation. As a first example we consider the case of *Quantum Elctrodynamics* (QED), the QFT of electromagnetic interaction, which be understood as the result of a U(1) local gauge invariance. The QED lagrangian (density) is given by

$$\mathcal{L}_{QED} = \overline{\psi}(i\gamma^\mu \partial_\mu - m)\psi - \mathcal{J}^\mu A_\mu - \frac{1}{4} F_{\mu\nu} F^{\mu\nu} \tag{1.3}$$

for $A_\mu = (A_0, \mathbf{A})$ four potential of the electromagnetic field, $F_{\mu\nu} = \partial_\mu A_\nu - \partial_\nu A_\mu$ field strength tensor, $\mathcal{J}^\mu = q\overline{\psi}\,\gamma^\mu \psi$ conserved (electromagnetic) current density from *global* gauge invariance, $\overline{\psi} = \psi^\dagger \gamma^0$, $\psi(x)$ Dirac field.
Equation (1.3) is *invariant* under U(1) transformations

$$\psi \to e^{i\alpha(x)q}\psi \tag{1.4}$$

The QED lagrangian can be obtained by considering the Dirac Lagrangian

$$\mathcal{L} = \overline{\psi}(i\gamma^\mu \partial_\mu - m)\psi = \mathcal{L}_{free} \tag{1.5}$$

which is *not* invariant under (1.4). In order to recover (1.3), we start by introducing the *covariant derivative*

$$\mathcal{D}_\mu = \partial_\mu + iqA_\mu(x) \tag{1.6}$$

for A_μ transforming according to

$$A_\mu \to A_\mu + \frac{1}{e}\partial_\mu \alpha(x) \tag{1.7}$$

If now we substitute to ∂_μ the expression for the covariant derivative, we recover a U(1) invariant expression, at the cost of adding an *interaction term*, of the form

$$\mathcal{L}_{int} = -\mathcal{J}^\mu A_\mu = -qA_\mu \overline{\psi}\gamma^\mu \psi \tag{1.8}$$

containing a *gauge field* A_μ which couples to the Dirac field. Considering the new field as the physical electromagnetic one, an additional term accounting for the free photon propagation must be included. Such term corresponds to the electromagnetic field lagrangian

$$\mathcal{L}_{EM} = -\frac{1}{4} F_{\mu\nu} F^{\mu\nu} \tag{1.9}$$

No *mass term* for the photon is present in the QED lagrangian, which would have taken the form $\frac{1}{2}m^2 A_\mu A^\mu$. This term would have spoiled the gauge invariance: the fact that the photon is massless can be derived as a consequence of this principle.

1.1.2 QCD

Quantum Chromodynamics (QCD)[5] provides the description of the strong interaction. In QCD a quantum number, the aforementioned *colour charge*, is introduced. Colour charge is carried by quarks and gluons, which can be of three different types: red (r), green (g) and blue (b) (together with the corresponding anticolours for antiquarks). The first hint on the existence of this quantum number came from the observation of the Δ^{++} baryon, in 1951. According to the quark model, the flavour and spin content of this baryon is

$$\left|\Delta^{++}\right\rangle = |u_\uparrow u_\uparrow u_\uparrow\rangle$$

i.e. an highly symmetric configuration, in contrast with the fact that Δ^{++} is a fermion and thus must have an overall anti-symmetric wave-function.Thanks to the introduction of this additional quantum number associated to the SU(3) group, it was possible to arrange the Δ^{++} baryon in an anti-symmetrical colourless-state

$$\left|\Delta^{++}\right\rangle = \epsilon^{ijk}\,|u_{i,\uparrow} u_{j,\uparrow} u_{k,\uparrow}\rangle$$

The idea of QCD is based on an extension of what was discussed for the QED case, considering now the SU(3) group. The corresponding lagrangian is given by, for a generic quark *flavour* :

$$\mathcal{L}_{QCD} = \overline{q}(i\gamma^\mu D_{\mu\nu} - m)q - \frac{1}{4} G_{a\mu\nu} G^{a\mu\nu} \tag{1.10}$$

Where q $= (q_r, q_g, q_b)^T$ is the quark field, γ^μ once again the Dirac matrices, D_μ is the covariant derivative

$$D_\mu = \partial_\mu + igT_a G^a_\mu$$

with $T_a = \frac{1}{2}\lambda_a$ generators of the SU(3) group, λ_a the hermitian traceless Gell-Mann matrices of SU(3), analog to the SU(2) Pauli ones.
$G^a_{\mu\nu}$ is the gluon field strength tensor, for $a \in [1, ..., 8]$, and it is defined as

$$G^a_{\mu\nu} = \partial_\mu G^a_\nu - \partial_\nu G^a_\mu - g f_{abc} G^b_\mu G^c_\nu \tag{1.11}$$

with G^a_μ gluon fields, f_{abc} structure constants of the SU(3) group, i.e. such that the generators satisfy the condition

$$[T_a, T_b] = i f_{abc} T_c$$

Due to the non-Abelian nature of the group, gluon self interaction is possible. An example of gluon self-interaction vertices is shown in figure 1.2.

(a) Triple-boson vertex. (b) Tetra-boson vertex.

Figure 1.2: An example of allowed self interaction vertices in QCD

Such gluon-gluon interaction has a fundamental consequence on the behaviour of the coupling constant for strong interaction, $\alpha_s(Q^2) = \frac{g_s^2}{4\pi}$:

$$\alpha_s(Q^2) = \frac{12\pi}{(33 - 2n_f)\log\left(\frac{Q^2}{\Lambda^2}\right)} \tag{1.12}$$

With n_f equal to the number of (active) quark flavours at the considered energy scale and Λ free parameter. From (1.12) follows that for values of the transferred momentum Q^2 much larger than the parameter Λ^2, the effective coupling of the strong interaction is small. Thus, a perturbative approach makes sense in this limit and we are in a condition known as *asymptotic freedom*. On the other hand, when Q^2 becomes comparable with the parameter, a perturbative approach ceases to be a viable solution: quarks and gluons will arrange into strongly bound configurations, the hadrons. The situation is known as *confinement*.

1.1.3 Weak interactions and ElectroWeak unification

Weak interactions have several unique features with respect to the other two SM model interactions. First, they are mediated by three *massive* gauge bosons, $W^{\pm}$ and Z^0. Depending on the mediator, we distinguish between *charged current weak interactions* (CC) and *neutral current weak interactions* (NC), for the case of the Ws and the Z respectively. The corresponding vertices are shown in figure 1.3
Weak interactions are the only SM ones in which *parity is not conserved*, as demonstrated in 1957 by Wu and collaborators in the study of polarized ^{60}Co β decay [6]. This is reflected by the V-A (*vector - axial vector*) structure of weak interactions.
For instance, the interaction vertices for weak *charged* current processes correspond to a contribution:

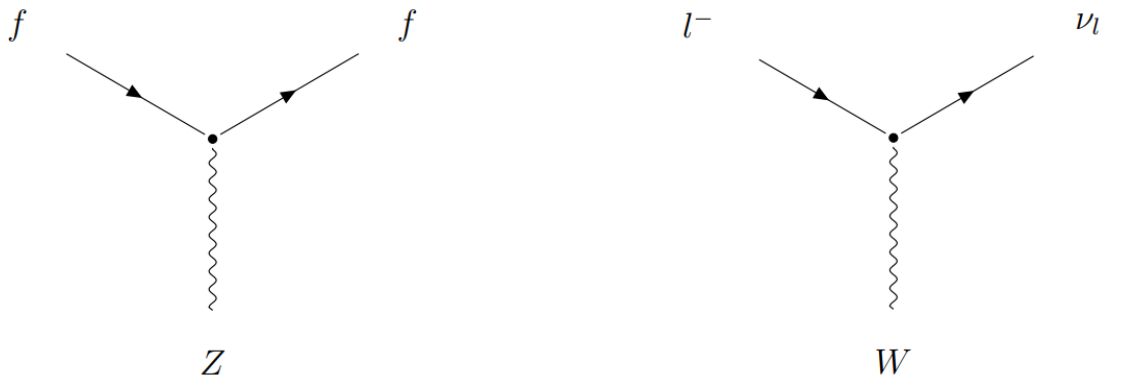

(a) NC interaction vertex. (b) CC interaction vertex.

Figure 1.3: Neutral Current and Charged Current vertices, respectively shown for a generic fermion f and a generic lepton l and the corresponding flavour neutrino ν_l

$$-\frac{ig}{\sqrt{2}}\frac{1}{2}\gamma^{\mu}(1-\gamma^{5}) \tag{1.13}$$

with g weak coupling constant, $\gamma^5 = i\gamma^0\gamma^1\gamma^2\gamma^3$. From the form of *Right-Handed* (RH) and *Left-handed* (LH) *chiral* projection operators

$$P_R = \frac{1}{2}(1+\gamma^5) \qquad\qquad P_L = \frac{1}{2}(1-\gamma^5) \tag{1.14}$$

Satisfying the relations

$$P_L + P_R = 1, \qquad P_R^2 = P_R, \qquad P_L^2 = P_L, \qquad P_R P_L = 0$$

It follows that only LH (RH) chiral *particle* (*antiparticle*) states take part in *weak* interactions .
Quarks weak interactions are described via the Cabibbo-Kobayashi-Maskawa (CKM) matrix, relating the weak and mass eigenstates according to

$$\begin{pmatrix} u' \\ s' \\ b'' \end{pmatrix} = \begin{pmatrix} V_{ud} & V_{us} & V_{ub} \\ V_{cd} & V_{cs} & V_{cb} \\ V_{td} & V_{ts} & V_{tb} \end{pmatrix} \begin{pmatrix} d \\ s \\ b \end{pmatrix} \tag{1.15}$$

The CKM matrix is a unitary matrix of diagonal elements almost equal to one.

Following the same gauge symmetry principle we have used for QED and QCD, it is possible to provide a description of weak interactions in terms of a quantum field theory, know as *Quantum Flavour Dynamics* (QFD), which is symmetric under $SU(2)_L$

rotations. It is convenient to introduce a notation where fermionic fields describing particles are arranged into LH weak isospin doublets and RH weak isospin singlets, according to

$$\psi_1(x) = \begin{pmatrix} u_L \\ d_L \end{pmatrix}_L, \quad \psi_2(x) = u_R, \quad \psi_3(x) = d_R \tag{1.16}$$

and analogously for the remaining quarks as well as for the lepton case.

The unified description of the electromagnetic and weak interactions was developed by Glashow, Salam and Weinberg (GSW) in the 1960. In the GSW model, the $U(1)_{em}$ gauge symmetry of electromagnetism is replaced by the $U(1)_Y$ gauge symmetry, giving rise to a new gauge field B_μ, where $Y = 2(Q - I^3)$ is the *weak hypercharge* and I^3 represents the third component of the weak isospin. Moreover, three gauge fields W^k_μ ($k = 1, 2, 3$) associated to the $SU(2)_L$ are introduced, from which the covariant derivative

$$\mathcal{D}_\mu = \partial_\mu + ig\frac{\sigma_k}{2}W^k_\mu + ig'\frac{Y}{2}B_\mu \tag{1.17}$$

is defined. Here, σ_k are the Pauli matrices, generators of SU(2), while g and g' represent the coupling constants of $SU(2)_L$ and $U(1)_Y$ respectively. From them, one can introduce the field strength tensors

$$W^k_{\mu\nu} = \partial_\mu W^k_\nu - \partial_\nu W^k_\mu - g\epsilon_{ijk}W^i_\mu W^j_\nu \tag{1.18}$$

$$B_{\mu\nu} = \partial_\mu B_\nu - \partial_\nu B_\mu \tag{1.19}$$

Using these, we can write the EW theory lagrangian in the form

$$\mathcal{L}_{EW} = \sum_{k=1}^{3} i\overline{\psi}_k(x)\gamma^\mu\mathcal{D}_\mu\psi_k(x) - \frac{1}{4}W^k_{\mu\nu}W^{\mu\nu}_k - \frac{1}{4}B_{\mu\nu}B^{\mu\nu} \tag{1.20}$$

The first term describes the fermions propagation and interaction, while the next two are respectively the one related to the free $SU(2)_L$ and $U(1)_Y$ field propagation.
The physical W, Z and photon fields are obtained via a linear combination of the gauge ones, respectively as

$$\begin{aligned} W^\pm_\mu &= \tfrac{1}{\sqrt{2}}(W^{(1)}_\mu \mp iW^{(2)}_\mu) \\ Z_\mu &= -B_\mu \sin\theta_W + W^{(3)}_\mu \cos\theta_W \\ A_\mu &= B_\mu \cos\theta_W + W^{(3)}_\mu \sin\theta_W \end{aligned} \tag{1.21}$$

The θ_W mixing angle is known as the *Weinberg angle* ($\simeq 30°$). The Weinberg angle also allows to define the relation between the coupling constants for SU(2)$_L$ (g) and U(1)$_Y$ (g′):

$$e = g \ \sin\theta_W = g' \cos\theta_W \tag{1.22}$$

Spontaneous Symmetry Breaking and BEH mechanism

It is an experimental observation that Ws and Z bosons are massive particles. The lagrangian (1.20) do not contain a term capable to explain such observation. To this purpose, an additional complex scalar field has to be introduced:

$$\phi = \begin{pmatrix} \phi^+ \\ \phi^0 \end{pmatrix} = \frac{1}{\sqrt{2}} \begin{pmatrix} \phi_1 + i\phi_2 \\ \phi_3 + i\phi_4 \end{pmatrix} \tag{1.23}$$

Using this we can add to (1.20) a term

$$\mathcal{L}_{Higgs} = (\mathcal{D}^\mu\phi)^\dagger(\mathcal{D}_\mu\phi) - V(\phi^\dagger\phi) = (\mathcal{D}^\mu\phi)^\dagger(\mathcal{D}_\mu\phi) - \mu^2\phi^\dagger\phi - \lambda(\phi^\dagger\phi)^2 \tag{1.24}$$

With V(ϕ) known as the Higgs potential. For $\mu^2 < 0$ and $\lambda > 0$, the potential has (infinite) degenerate minima

$$\phi^\dagger\phi = -\frac{\mu^2}{2\lambda} = \frac{v^2}{2} \tag{1.25}$$

Choosing a particular minimum leads to a *spontaneous symmetry breaking* of the lagrangian. Taking in particular

$$\phi_0 = \langle 0|\, \phi \,|0\rangle = \begin{pmatrix} 0 \\ \frac{v}{\sqrt{2}} \end{pmatrix} \tag{1.26}$$

And expanding the field around the minimum according to

$$\phi(x) = \frac{1}{\sqrt{2}} \begin{pmatrix} 0 \\ v + h(x) \end{pmatrix} \tag{1.27}$$

for h(x) small excitation (Higgs field), one can obtain the missing mass terms. In particular,the expression for the W boson mass is given by

$$m_W = \frac{1}{2} g v \tag{1.28}$$

While for the Z boson

$$m_Z = \frac{1}{2} v \sqrt{g^2 + g'^2} \tag{1.29}$$

It has to be noted that the mass terms for fermions can be obtained too via the Higgs mechanism.

1.2 The Top quark

The first observation of the top quark was achieved by the CDF [1] and DØ [2] collaborations at Tevatron in 1995 and marked the end of a long journey for the remaining sixth quark of the SM. The LH top quark is the Q= $2/3$, $T_3 = +1/2$ member of a weak isospin doublet containing the botton quark, while the RH top belong to an $SU(2)_L$ singlet [4]. The entire top quark phenomenology is driven by its large mass. In fact, the top quark is, by a large margin, the heaviest fundamental particle, with a mass $= 172.69 \pm 0.30$ GeV [4]. Due to the fact that this mass is close to the *electroweak symmetry breaking scale*, it plays a crucial role in the understanding of this mechanism. Moreover, this large mass implies also a large coupling to the Higgs boson, making the top quark a privileged probe for the Higgs sector.
Furthermore, top quark plays also an important role in the search for physics beyond the Standard Model (BSM), both via its production and decay mechanisms and as a background of many processes considered in this searches. A precise and complete knowledge of this particle is thus important in order to provide constrains on new physics [7].

1.2.1 Top quark pair production

Top quark production in pp or $p\bar{p}$ collisions occurs either in pairs ($t\bar{t}$) or individually (single top) .

The most abundant process for $t\bar{t}$ pairs at hadron colliders is QCD pair production [8]. At Tevatron, the *leading order* (LO) processes for $t\bar{t}$ production occurred predominately via quark-antiquark annihilation, while at LHC the production takes place mostly via gluon fusion (figure 1.4). This is a consequence of the different dominating *parton distribution functions* (PDFs), for the two corresponding different center of mass energies $\sqrt{s}$ and different beam compositions, which lead to distinct values of the dimensionless fraction $x = \frac{Q^2}{2M\nu}$ (*Bjorken x*). Here, Q is the transferred 4-momentum, M is the target nucleon mass, ν is the energy transferred in the collision. Each parton i involved in the collision carries a fraction x_i of the total nucleon momentum. The cross section for the process AB$\rightarrow t\bar{t} + X$ can be written according to

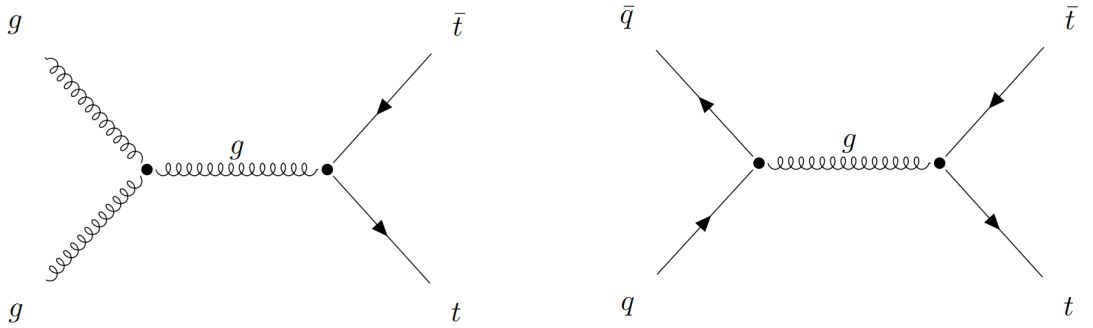

Figure 1.4: Example of Feynman diagrams involved in $t\bar{t}$ production via gluon fusion (on the left-hand side) and quark annihilation (on the right-hand side).

$$\sigma(\hat{s}, m_t) = \sum_{i,j=q,\bar{q},g} \int dx_i dx_j f_i(x_i, \mu_F^2) f_j(x_j, \mu_F^2) \hat{\sigma}^{ij \to t\bar{t}}(\hat{s}, m_t^2, \alpha(\mu_R^2), \mu_R^2). \tag{1.30}$$

Figure 1.5 shows a summary of the $t\bar{t}$ production cross section measurements as performed at LHC and Tevatron.
In (1.30), f_i and f_j represent respectively the A and B hadron PDFs, describing the probability densities of a parton in the corresponding particle of carrying a momentum fraction x, $\hat{\sigma}$ is the *hard* parton-parton scattering cross section, $\hat{s} = (p_i + p_j)^2 = (x_i p_A + x_j p_B)^2$ is the square of the center of mass energy of the colliding partons, while μ_F and μ_R are respectively the *factorization scale*, having the meaning of the energy scale defining the separation between the physical processes at short and long distance, and the *renormalization scale*, which corresponds to an additional energy scale resulting from the renormalization procedure applied in order to treat the *ultra violet* (UV) divergences appearing in the perturbative calculation of $\hat{\sigma}$. Conventionally, the two scales[1] are chosen to be equal both to m_t [8].

1.2.2 Single top quark production

The top quark can also be produced individually via *ElectroWeak* (EW) processes (purely EW at LO), with an inclusive cross section about two or three times smaller than the strong $t\bar{t}$ one [8]. Figure 1.7 provides summary of the measured and predicted single top production cross sections, for the different possible channels, at LHC energies. The EW vertex for top quark production contains the V_{tb} CKM matrix element, providing a way to measure it directly in single quark production.
Three different mechanisms lead to single top production: the s-channel, the t-channel

[1] In the analysis however a dynamical scale was adopted in the MC simulations employed

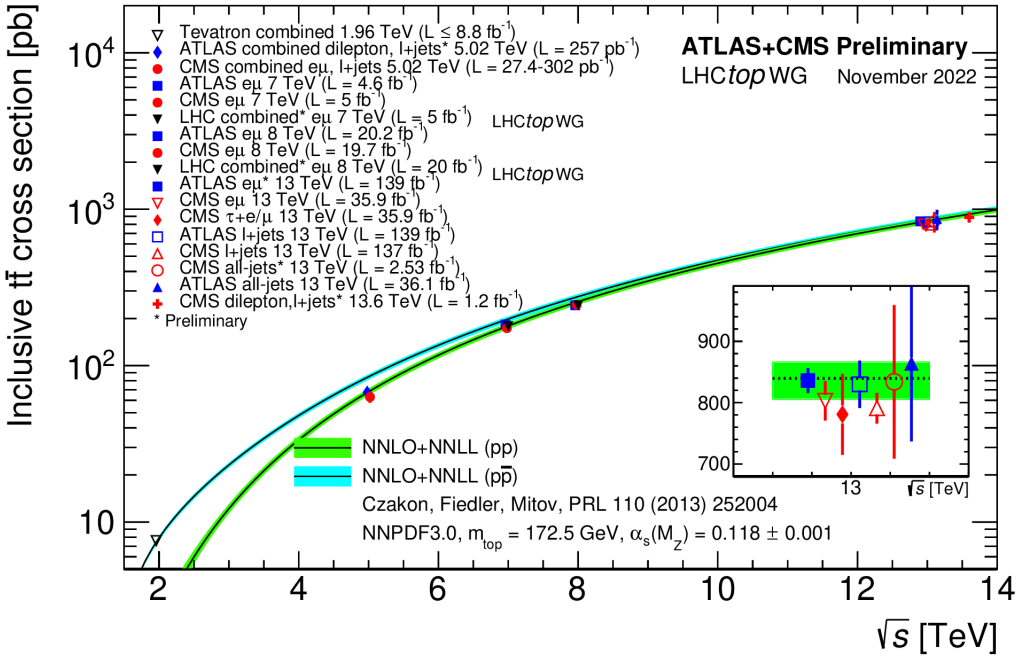

Figure 1.5: Measured and predicted $t\bar{t}$ production cross sections from Tevatron ($p\bar{p}$) and LHC (pp) collisions [9].

and the associated tW-channel, which includes an on-shell W boson. An example of diagrams for the corresponding channels at LO is shown in figure 1.6
The definition of the latter requires some care: the inclusion of higher order (already at NLO) corrections for this channel leads to interference with the $t\bar{t}$ processes, which can become extremely large in certain phase-space regions, spoiling the perturbative calculations on the tW [10]. In fact, when considering the NLO correction to tW, an additional b quark is present, leading to a tWb vertex. Thus, an *identical* $WbWb$ final state is observed both in the tW decay at NLO and in the $t\bar{t}$ decay at LO. The problem of interference between tWb and $t\bar{t}$ will be discussed in section 1.3.

While production at Tevatron occurred predominantly through the s- and t- channels, at LHC the t-channel is the dominant one. The single top production can be calculated according to two different PDF schemes: a first one in which the initial state is characterized by the presence of a b quark (*five flavour scheme* or (5FS)), with a LO production process corresponding to $qb \to q't$, or a second one in which the initial state gluon splits into a $b\bar{b}$ pair and one of the b quarks interacts with the *virtual* W boson, called *four flavour scheme* (4FS), with a LO process corresponding to $qg \to q't\bar{b}$. In the 4FS, the spectator q' quark is emitted at a relatively small angle with respect to

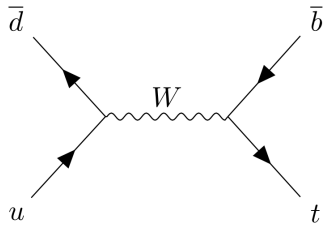

(a) s-channel

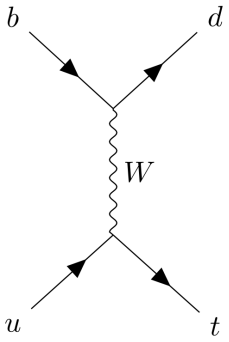

(b) t-channel

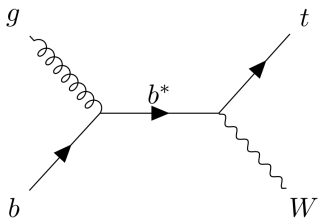

(c) tW

Figure 1.6: Single top production channels at leading order

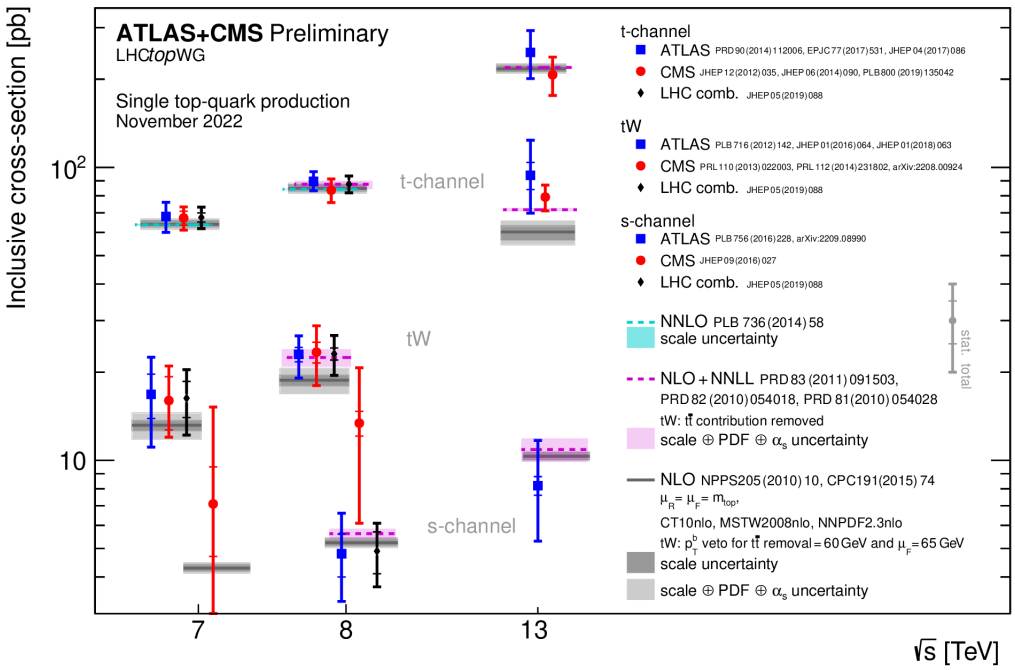

Figure 1.7: Measured and predicted single top production cross sections at LHC energies in pp collisions [9].

the beam axis, leading to a jet of large $|\eta|$, which represents the characteristic signature of the t-channel.

1.2.3 Top quark decay

A distinctive feature of the top quark is its extremely short lifetime, of approximately $0.5\times10^{-24}s$ [4]. In the SM, its decay occurs via an EW charged-current process:

$$t \to W^+ q \tag{1.31}$$

for q down-type quark. Let V_{tq} be the corresponding CKM matrix element. Assuming $|V_{tb}| \gg |V_{td}|, |V_{ts}|$ and a mass above the Wb threshold, the decay width of the top quark is expected to be dominated by the two body channel corresponding to $t \to Wb$. If we neglect the terms of order α_s^2, m_b^2/m_t^2 and $(\alpha_s/\pi)M_W^2/m_t^2$, the width at NLO is given by [4]:

$$\Gamma_t = \frac{G_F m_t^3}{8\pi\sqrt{2}} \left(1 - \frac{M_W^2}{m_t^2}\right)^2 \left(1 + 2\frac{M_W^2}{m_t^2}\right)^2 \left[1 - \frac{2\alpha_s}{3\pi}\left(\frac{2\pi^2}{3} - \frac{5}{2}\right)\right] \tag{1.32}$$

Where G_F is the Fermi constant and m_t the top quark pole mass. Experimentally, the

condition $|V_{tb}| \gg |V_{td}|, |V_{ts}|$ holds, and the Wb is indeed the dominating decay mode, with a branching ratio [4]:

$$\frac{\Gamma(t \to Wb)}{\sum_{q=b,s,d} \Gamma(t \to Wq)} = 0.957 \pm 0.034. \tag{1.33}$$

Due to its short lifetime, shorter than the typical time scale for hadronization, which can be estimated from the inverse of the Λ_{QCD} energy scale at which perturbative QCD ceases to be applicable $(1/\Lambda_{QCD}) \simeq 3 \times 10^{-34}$ s [8], bound states of the top quark are not possible. Therefore, top mesons of the form $t\overline{q}$ as well as the so-called *Toponium* $t\bar{t}$ bound state are, in principle, excluded.

The classification of the $t\bar{t}$ final states is based on the final decay of the two resulting W bosons. Three cases are considered [4]:

$$t\bar{t} \to W^+bW^-\bar{b} \to q\overline{q}'bq''\overline{q}''\bar{b} \tag{1.34}$$

$$t\bar{t} \to W^+bW^-\bar{b} \to q\overline{q}'bl^-\overline{\nu_l}\bar{b} + l^+\nu_l bq''\overline{q}''\bar{b} \tag{1.35}$$

$$t\bar{t} \to W^+bW^-\bar{b} \to l^+\nu_l bl'\nu_{l'}\bar{b} \tag{1.36}$$

Which are referred to respectively as the *all hadronic* (with a branching ratio of 45.7%), *lepton+jets* (43.8%) and *dilepton* (10.5%). In principle, the lepton contribution above could refer to any one among e, μ, τ leptons. However, most analyses make a further distinction between the e, μ cases and the τ channel, since the latter is more difficult to reconstruct. Furthermore, additional jets can be present, as a consequence of extra QCD radiation coming from colored particles present in the event. Figure 1.8 shows an example of Feynman diagram for the decay of a top quark.

1.2.4 Top quark properties

The top quark has several notable properties, one of which (its lifetime) and the related consequences have already been discussed in the context of the top quark decay. Among the many other characteristics, we can highlight:

1. *Top quark mass*: The top quark mass represents one of the fundamental parameters of the SM. It is connected to both the W and Higgs boson masses. For instance, a precise measurement of the top mass is important for constraining the radiative corrections of the W boson propagator, which appear in the corresponding expression for the boson's mass:

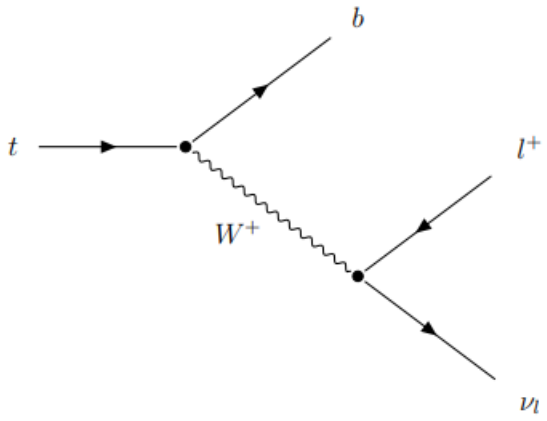

Figure 1.8: Decay of a top quark into a W^+b, leading to a $l^+\nu$ final state.

$$M_W^2 = \frac{\pi \alpha_{EM}}{\sqrt{2} G_F \sin^2 \theta_W} \frac{1}{1 - \Delta r} \tag{1.37}$$

Where the one-loop corrections Δr can be expressed as

$$\Delta r \sim \Delta \rho_0 - \frac{\Delta \rho}{\tan^2 \theta_W} \approx 3\% \tag{1.38}$$

$\Delta \rho_0$ accounts for the running of the coupling constant α_s and

$$\Delta \rho = \frac{3 G_F m_t^2}{8\sqrt{2}\pi^2} \tag{1.39}$$

An example of the one-loop corrections is presented in figure 1.9.

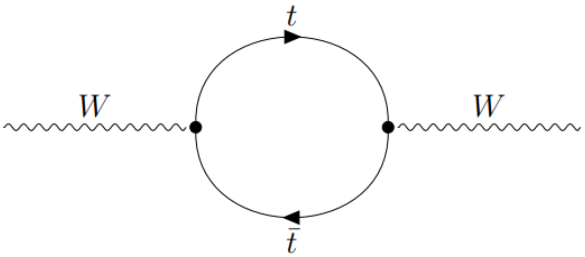

Figure 1.9: Virtual top quark one loop contributing to the W mass.

Moreover, combined measurements of the top quark mass and of the W boson mass allow to constrain the values of the Higgs boson mass, thus testing the global consistency of the standard model. An example of such constraint is shown in figure 1.10.

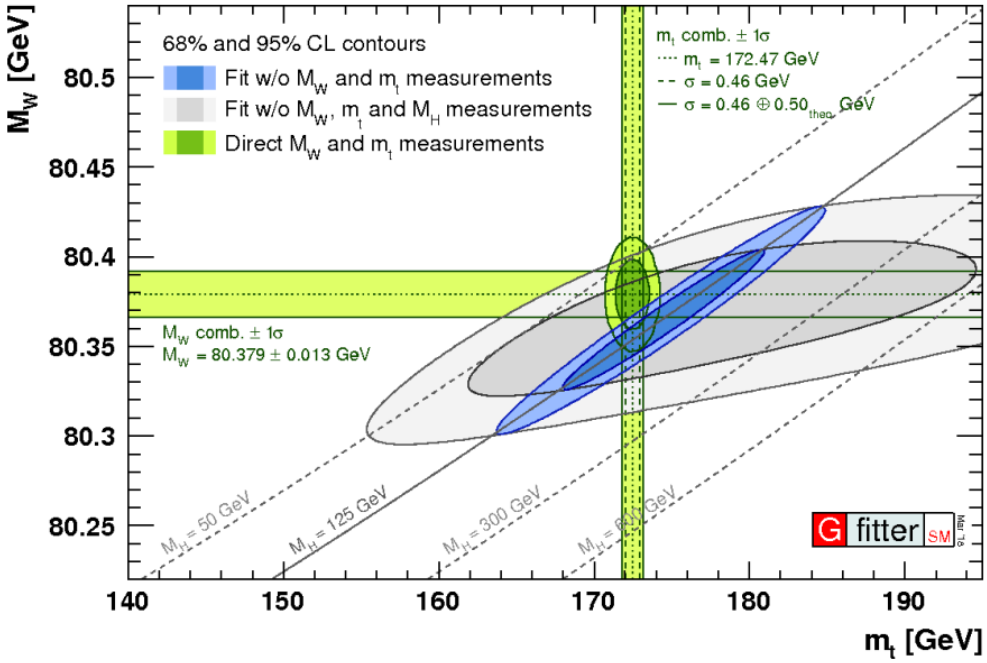

Figure 1.10: 68% and 98% confidence level (CL) contours for the indirect determination of the W mass and top quark mass. The blue (grey) areas correspond to the fit results obtained when the direct Higgs-boson mass measurements are included (excluded). The contours are compared to the direct measurements of the masses, shown by the horizontal and vertical green bands [11].

Lastly, an accurate knowledge of m_t (in combination with m_H, mass of the Higgs boson), provides a test of the *stability of the vacuum state* of the SM, which is related to the ultimate fate of the universe. As it can be seen from figure 1.11, current measurements show that we are in a region of *metastability*: the possibility of disappearance of the universe is not excluded, but constrained to a time much larger than the universe age [12].
Measurements of the m_t are performed either directly or indirectly. In the first case, one proceeds via *kinematic reconstruction*, for example by comparing the m_t distribution as reconstructed from data to a set of available MC simulated distributions- the so-called *template method*- for different values of the top mass parameter in the simulation. Alternatively one can consider different proce-

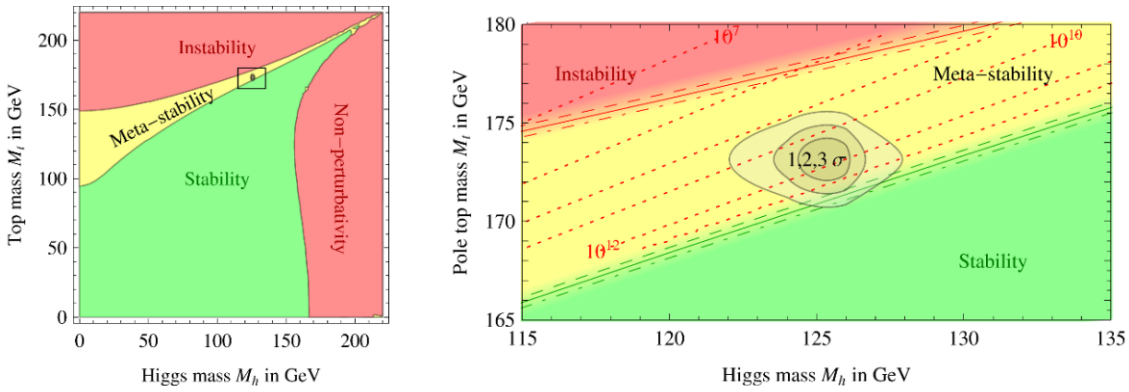

Figure 1.11: Regions of Instability, Stability and Meta-stability of the SM vacuum. On the right end side, a zoom to the region corresponding to the preferred experimental range for the Higgs and top top masses is shown. The grey areas correspond to the allowed regions at 1, 2 and 3σ [12].

dures, such as the *Matrix Element Method* (MEM), in which a probability for each event is calculated as a function of the top mass, using a LO matrix element for the production and decay of top-antitop pairs. In an indirect approach instead one obtain an estimate from the measurement of the cross section. A summary of top quark mass measurements performed at LHC and Tevatron is shown in table 1.2. In any case, the definition of the top quark mass is not univocal. In particular, one possible choice is to consider the *pole mass* ("on-shell") m_t^{pole} [13], defined as the real part of the renormalized top quark propagator pole, which is located at

$$\sqrt{p^2} = m_t^{pole} - \frac{i}{2}\Gamma \tag{1.40}$$

where Γ is the top width and p its four momentum.

2. *Top quark Spin Correlations*: The top quark decays before its spin gets flipped by strong interaction. This allows a direct observation of the top quark polarization via the study of the angular distribution of its decay products, making thus possible to define and measure observables sensitive to the top quark spin [14]. Top quark pair production ($t\bar{t}$) is not expected, according to the SM, to give rise to polarized top. However, the spins of the top and the anti-top are predicted to be correlated and such correlation has been observed at LHC by both the ATLAS and CMS collaborations [15]. Moreover, the direction of the top quark spin is 100% correlated to the angular distribution of the down type fermions present after the decay. In particular, charged leptons arising from the leptonic W decay

Table 1.2: Top quark measurements from Tevatron and LHC, with statistical uncertainties listed first, followed by the systematics. In the last two lines, the integrated luminosities refer to the highest values recorded in the runs employed in the corresponding combined measurements, for each of the listed experiments [4].

m_t (GeV/c^2)	Experiment	$\int \mathcal{L}dt$ fb^{-1}	Channel
$172.08 \pm 0.25 \pm 0.41$	ATLAS	20.2	l+jets+ll+All jets
$172.44 \pm 0.13 \pm 0.47$	CMS	19.7	l+jets+ll+All jets
$172.35 \pm 0.16 \pm 0.48$	CMS	19.7	l+jets
$172.34 \pm 0.20 \pm 0.70$	CMS	35.9	ll
$173.72 \pm 0.55 \pm 1.01$	ATLAS	20.2	All jets
$172.08 \pm 0.25 \pm 0.41$	ATLAS	20.2	l+jets+ll+All jets
$172.25 \pm 0.08 \pm 0.62$	CMS	35.9	l+jets
$172.6 \pm 0.4 \pm 2.4$	CMS	35.9	Boosted jets
$172.13 \pm 0.32^{+0.60}_{-0.70}$	CMS	35.9	Single top
$174.30 \pm 0.35 \pm 0.54$	CDF,DØ (I+II)	≤ 9.7	publ. or prelim
$173.34 \pm 0.27 \pm 0.71$	Tevatron+LHC	$\leq 8.7 + \leq 4.9$	publ. or prelim

carry almost the full spin information of the top quark, making the the angular distribution of charged leptons the preferred one for the study of top spin correlation.

3. *Yukawa Coupling*: Fermion masses arise from a Yukawa interaction with coupling $g_f = \frac{\sqrt{2}m_f}{v}$, where v is the VEV (vacuum expectation value, $v \simeq 246$ GeV). The top quark is particularly remarkable in this regard, as it is characterized not only by the highest coupling among the elementary particles, due to its particularly large mass, but also due to the fact the the resulting coupling is very close to unity. The measurement of the top quark Yukawa coupling is performed at LHC by considering the $t\bar{t}H$ processes.

4. *W boson helicity*: The SM prescribes the same V-A CC weak interaction for the top quark as for any other fermion, i.e. $-i\frac{g}{\sqrt{2}}V_{tb}\gamma^{\mu}\frac{1}{2}(1-\gamma_5)$. The model also dictates that the fraction of top quarks decaying into longitudinally polarized W bosons is proportional to the *Yukawa coupling* of the top quark, resulting in an enhancement with respect to the weak coupling. Introducing the notation $\mathcal{F}_0, \mathcal{F}_+, \mathcal{F}_-$ to label the fractions of longitudinally, LH and RH W bosons respectively, their values are expected to be $\mathcal{F}_0 \sim 70\%$, $\mathcal{F}_+ \sim 30\%$ and,$\mathcal{F}_- \sim 0\%$. These fracions could significantly change in presence of some anomalous couplings, which could be inferred experimentally by studying the angular distribution between lepton from the W decay and b-jets from the same top decay [4, 7].

5. *Forward-Backward and Charge Asymmetries*: The study of potentially large $t\bar{t}$ production asymmetries is motivated by the fact that their observation would be a sign of BSM physics. Perturbative QCD predicts, at LO,the $t\bar{t}$ production to be symmetric under an $t \longleftrightarrow \bar{t}$ exchange. However, while the $gg \to t\bar{t}$ remains symmetric at NLO, the $q\bar{q} \to t\bar{t}$ process present a small asymmetry, caused by the interference of tree-level and one-loop contributions for the $t\bar{t}$ production. In order to study this asymmetry, one has to account for the different initial states, i.e. pp or $p\bar{p}$ and the different fractions of gluon fusion and $q\bar{q}$ processes occurring. Depending on them, different asymmetry observables were defined for Tevatron and LHC.

   At Tevatron, the production asymmetry manifested as a *forward-backward* asymmetry, with related observable defined as [4]:

$$A_{FB}^{t\bar{t}} = \frac{N(\Delta y > 0) - N(\Delta y < 0)}{N(\Delta y > 0) + N(\Delta y < 0)} \tag{1.41}$$

   With $\Delta y = y_t - y_{\bar{t}}$ *rapidity* difference between the top and the anti-top. At LHC, where the dominant mechanism for $t\bar{t}$ pair production is gluon fusion, the mea-

surement is more difficult. Instead, one introduces a different observable, the so-called *charge asymmetry* A_C, which is defined according to:

$$A_C^{t\bar{t}} = \frac{N(\Delta|y| > 0) - N(\Delta|y| < 0)}{N(\Delta|y| > 0) + N(\Delta|y| < 0)} \tag{1.42}$$

Despite the early claim from the CDF and DØ of an excess in the asymmetry measured with respect to SM predictions, the later measurements, including those performed at LHC, are consistent with the SM expectations [4].

1.3 $WbWb$ production

The goal of the present thesis is to provide the measurement of the differential cross section for the production of the $WbWb$ state, in the process

$$pp \to W^+bW^-\bar{b} + X \tag{1.43}$$

In the present section, an overview of the $WbWb$ production mechanism is presented, together with a discussion of the state-of-art for the measurement of the $WbWb$ production cross section. To this purpose, the processes contributing to this final state and the problem of interference between said contributions are introduced.

1.3.1 $WbWb$ production cross section and $t\bar{t} - tWb$ interference

As it was mentioned in section (1.2.3), eqs. (1.34) to (1.36), the production of the $WbWb$ state can take place following the decay of a $t\bar{t}$ pair, at LO. This process represents actually just *one* of the several possible that can lead to the very same final state. Its contribution corresponds to *doubly resonant* diagrams presenting, as the name suggests, two top quark resonances. The bulk of the inclusive $WbWb$ cross section, is efficiently reproduced in the so-called *Narrow-Width Approximation* (NWA), which incorporates doubly resonant effects, in the limit of vanishing top quark width, i.e. for $\Gamma_t \to 0$ [16]. In this limit, the denominator of the top quark propagator can be written as

$$\lim_{\Gamma_t \to 0} \frac{1}{(p_t^2 - m_t^2) + m_t^2\Gamma_t^2} = \frac{\pi}{m_t\Gamma_t}\delta(p_t^2 - m_t^2) + O\left(\frac{\Gamma_t}{m_t}\right) \tag{1.44}$$

This approach introduces a $1/\Gamma_t$ factor for each top quark resonance, strongly suppressing the singly and non resonant contributions. The full process is then factorized into top quark pair production and decay. Thus, the NWA provides a description restricted to $t\bar{t}$ on-shell states, with a limited accuracy in the description of the full process [17]. Therefore, to achieve a complete description of the $WbWb$ production, *all* the possible contributions should be considered: the inclusion of all the off-shell

effects from doubly, *singly* and *non resonant* diagrams, containing only one or no resonant top quarks, allows to account for all contributions that are suppressed by factors corresponding to powers of Γ_t/m_t. An example of diagrams involved is shown in

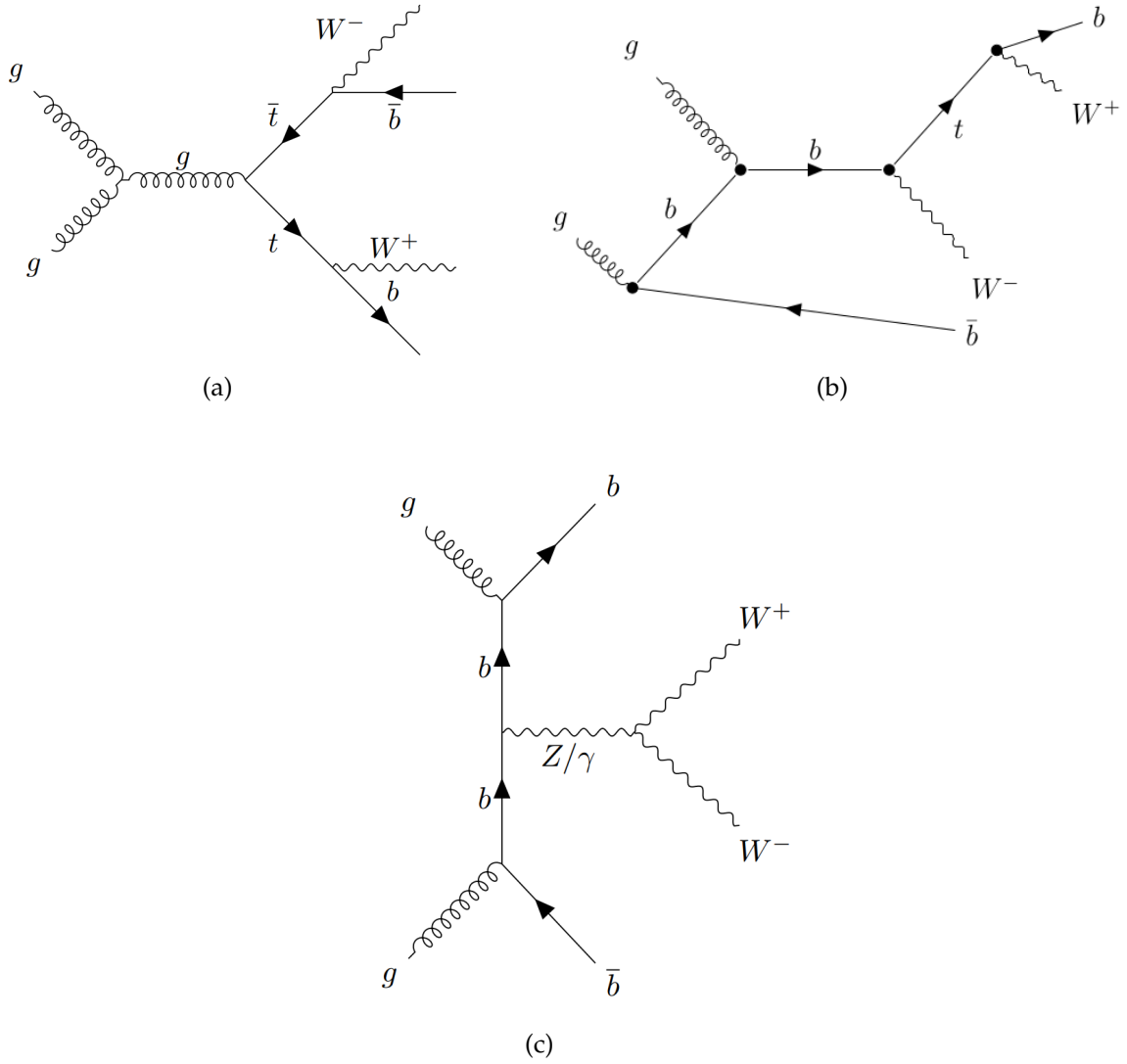

Figure 1.12: Examples of doubly-resonant (a), singly-resonant (b) and non resonant (c) diagrams.

Calculations of the full process are available, also at higher order, in a fixed flavour scheme (both for the 4FS and the 5FS one) [18–20]. They are based on the adoption of the *complex mass scheme*, which allows to take into account the top quark decay width in a gauge invariant way. Such complex mass scheme is based on the introduction of

the complex quantity:

$$\mu_t^2 = m_t^2 - i m_t \Gamma_t \tag{1.45}$$

and analogously for the other resonances. These quantities are then replaced to the particles masses, inside the calculations, whenever the corresponding contribution appears. By applying the prescriptions discussed so far, one can achieve a description of the whole process, which encompasses both single-top and top-pair contributions, non resonant terms, is gauge invariant and includes interference and other finite-Γ_t effects. In this way, it is possible to evaluate the squared amplitude for the $WbWb$ production [20]:

$$\begin{aligned} |\mathcal{A}_{WbWb}|^2 &= |\mathcal{A}_{2t} + \mathcal{A}_{1t} + \mathcal{A}_{1\bar{t}} + \mathcal{A}_{0t}|^2 \\ &= |\mathcal{A}_{2t}|^2 + |\mathcal{A}_{1\bar{t}}|^2 + 2\mathrm{Re}(\mathcal{A}_{2t}\mathcal{A}_{1t}^*) \\ &\quad + |\mathcal{A}_{1t}|^2 + 2\mathrm{Re}(\mathcal{A}_{2t}\mathcal{A}_{1\bar{t}}^*) \\ &\quad + 2\mathrm{Re}(\mathcal{A}_{1t}A_{1\bar{t}}^*) + |\mathcal{A}_{0t}|^2 + 2\mathrm{Re}((\mathcal{A}_{2t} + \mathcal{A}_{1t} + \mathcal{A}_{1\bar{t}}) \cdot \mathcal{A}_{0t}^*) \end{aligned} \tag{1.46}$$

The cross section will then be proportional to the calculated amplitude. In the previous formula, the subscripts *2t* , *1t* and *0t* refer to the doubly resonant, single resonant e non resonant terms respectively. Additionally, the interference terms between individual contributions are considered, described by the real part of the complex quantities in parenthesis. The last line is expected to be negligible with respect to the remaining terms, which encompass the top-pair $t\bar{t}$ and tWb productions [20]. As a consequence, the following discussion will consider only the contributions coming from the $t\bar{t}$ and *tWb*, i.e. the tW contribution at NLO. This corresponds also the approach adopted in the analysis, in which only the doubly- and singly- resonant contributions are considered explicitly, together with the interference among them.

It is then relevant to discuss the issues related to the definition of the tW channel and its higher order corrections and how it can be isolated from $t\bar{t}$. The problem presents many theoretical subtleties, and was treated extensively in [10] and [21]. The squared matrix element for the tWb production can be written as:

$$|\mathcal{A}_{tWb}|^2 = |\mathcal{A}_{1t} + \mathcal{A}_{2t}|^2 = |\mathcal{A}_{1t}|^2 + 2 \cdot \mathrm{Re}(\mathcal{A}_{1t}\mathcal{A}_{2t}^*) + |\mathcal{A}_{2t}|^2 \tag{1.47}$$

Two main strategies have been developed in order to subtract the top pair contribution, known as *Diagram Removal* (DR) and *Diagram Subtractions* (DS) [20]:

1. *Diagram Removal*: two versions of DR have been proposed:

   - DR1 (*without interference*): The idea is to set the doubly resonant contributions to zero, $\mathcal{A}_{2t} = 0$, removing both the corresponding amplitude squared term and the interference one. Thus, one obtains:

$$|\mathcal{A}_{tWb}|^2_{DR1} = |\mathcal{A}_{1t}|^2$$

- DR2 (*with interference*): In this case, one only removes the contribution from $|\mathcal{A}_{2t}|^2$, keeping the interference term:

$$|\mathcal{A}_{tWb}|^2_{DR2} = |\mathcal{A}_{1t}|^2 + 2 \cdot \mathrm{Re}(\mathcal{A}_{1t}\mathcal{A}^*_{2t})$$

DR schemes involve the removal of some contribution over *the whole* phase space, and thus are not gauge invariant. Despite this, the related effect was found to be negligible [20].

2. *Diagram Subtraction* [20]: DS methods have been developed in order to avoid the problem of gauge dependence. In DS methods, the matrix element is written as:

$$|\mathcal{A}_{tWb}|^2_{DS} = |\mathcal{A}_{1t} + \mathcal{A}_{2t}|^2 - \mathcal{C}_{2t}$$

$\mathcal{C}_{2t}$ represents a *local* subtraction term, which is required to satisfy three conditions: first, the term should cancel exactly the doubly resonant matrix element squared, when the kinematics is exactly on top of the resonant pole. Secondly, the term should be gauge invariant and lastly, it has to decrease quickly once one moves away from the resonant region.

The subtraction term can be expressed, according to the previous conditions, in the form:

$$\mathcal{C}_{2t} = f(p^2_{Wb})|\mathcal{A}_{2t}|^2$$

with $p_{Wb} = (p_W + p_b)$. The pre-factor f can be chosen freely, and the usual choice is represented by a Breit-Wigner profile. In particular, two examples for the distribution proposed in the literature are:

- DS1:

$$f_1(s) = \frac{(m_t\Gamma_t)^2}{(s - m_t^2)^2 + (m_t\Gamma_t)^2}$$

- DS2:

$$f_2(s) = \frac{(\sqrt{s}\Gamma_t)^2}{(s - m_t^2)^2 + (\sqrt{s}\Gamma_t)^2}$$

The DS (and the DR2) methods present the introduction of a non-zero top width, which has to be regularized by modifying the denominator according the aforementioned complex mass scheme.

1.3.2 State of the art: measurement of the cross section as a function of interference-sensitive variables

Currently, the only available measurements of the $WbWb$ differential-cross section performed by the ATLAS collaboration are in the fiducial phase-space region where

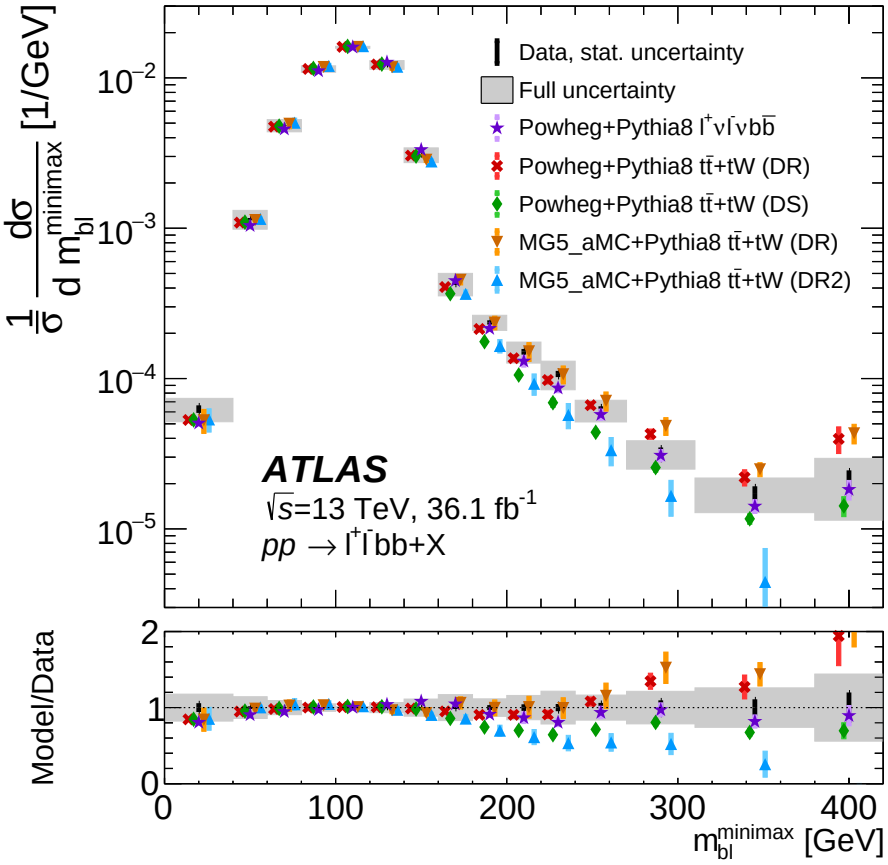

Figure 1.13: Normalized differential cross section, measured as a function of m_{bl}^{minimax}. A comparison with several theoretical predictions for the $t\bar{t} + tWb$ signal are shown on the top right part of the plot [22] .

the interference effects described in the present section are significant. In particular, the 2018 measurement [22] was performed in the dileptonic channel with exactly two b-tagged jets, and considered a variable specifically selected to its sensitivity to the interference effect: m_{bl}^{minimax}. The m_{bl}^{minimax} variable corresponds to the invariant mass of the system composed by a b-jet and a lepton, and it is defined as:

$$m_{bl}^{\text{minimax}} \equiv \min(\max(m_{b_1 l_1}, m_{b_2 l_2}), \max(m_{b_1 l_2}, m_{b_2 l_1})) \tag{1.48}$$

with b_i, l_i corresponding to the two $b-$jets and leptons, respectively. For the doubly resonant case, the condition $m_{bl}^{\text{minimax}} < \sqrt{m_t^2 - m_W^2}$ is satisfied. Due to the suppression of the doubly resonant contribution for higher values of the $m_{bl}^{minimax}$ variable, the differential cross section becomes more sensitive to interference effects above this kinematic endpoint. In particular, this is true for values above 200 GeV. The results of

this first measurement is show in figure 1.13

As of today, additional measurements in the interference-sensistive region are currently ongoing [23]. With respect to the current available measurement, the present thesis provides a measurement of the $WbWb$ differential cross section, in the dilepton channel and in a fiducial phase space with at least two final-state $b-$jets. The measurement is provided as a function of some basic kinematic observables, namely the transverse lepton momentum, transverse jet momentum, lepton invariant mass and the number of extra jets observed in the final state.

Chapter 2

LHC and The ATLAS experiment

2.1 LHC structure

The Large Hadron Collider (LHC) project was approved by the CERN Council in 1994 and started its operations in 2008. As of today, it still represents the largest and most powerful particle accelerator in the world. LHC is located on the Franco-Swiss border near Geneva, placed approximately 100 meters underground, in correspondence of the pre-existing 26.7 km of circumference tunnel that was once occupied by the Large Electron-Positron (LEP) collider [24]. LHC allows to study both proton-proton (*pp*) and heavy ion - heavy ion collisions, as well as heavy ion - proton collisions, with a design value of the center of mass energy for *pp* collisions of $\sqrt{s} = 14$ TeV and a present value of the center of mass energy for the run 3 of 13.6 TeV [14].

Several steps are required in order to achieve such energies, each one of them increasing the energy of the beam and injecting it in the next acceleration stage, with LHC being the last element of such chain. Starting from 2020, the linear accelerator 4 (Linac 4) became the source of proton beams for the CERN accelerator complex [25], accelerating H^- ions up to 160 MeV, before sending them to the Proton Synchrotron Booster (PSB). In this process of injection, the two electrons are stripped from the each negative ion, allowing to obtain the protons. These protons are then accelerated up to 2 GeV in order to prepare them for the injection in the next stage, the Proton Synchrotron (PS), where the beam reaches an energy of 26 GeV. At this point, the beam reaches the Super Proton Synchrotron (SPS), where it gets accelerated up to 450 GeV, in preparation for the final transfer to the two LHC beam pipes. The acceleration procedure for heavy ions, more precisely fully ionized lead atoms ($^{208}Pb^{82+}$) , is characterized by some differences in the initial steps. Once the ions are produced from the source, they are accelerated in the Linac 3 at an energy of 4.5 MeV/nucleon. Following this first acceleration stage, they are injected into the Low Energy Ion Ring (LEIR), where they reach an energy of 72 MeV/nucleon. At this point, they are sent to the PS and the rest of the process is mostly the same. LHC allows to accelerate these ions up to an energy of 1.38 TeV per nucleon [26]. The full acceleration complex is shown in figure 2.1.
LHC is a two-ring superconducting-hadron accelerator and collider, in which the two proton beams travel in separate *beam pipes* throughout most of the time and are brought together in the so-called interaction points. Such pipes must be maintained at *ultra high vacuum* (10^{-13} atm for the arch sections) in order to avoid potential collision with gas molecules inside the accelerator. This ultra high vacuum serves the additional purpose to reduce the amount of heat that seeps from the surroundings to the cryogenics parts, which are kept at a temperature of 1.9 K [27, 28].

The charged particles acceleration is performed by means of 16 *Radio Frequency* (RF) cavities, which are also required to compensate for *synchrotron radiation* losses as they pose a serious threat to the whole acceleration process. Indeed, the choice to move from LEP to LHC was also motivated by the need to overcome the limit on the maximum center of mass energy achievable accelerating electrons, as we can see from the fact that the energy loss due to synchrotron emission in a circular collider is related to the mass *m* of the emitting particle by

$$\frac{dE}{dt} \propto \frac{E^4}{m^4 R^2} \tag{2.1}$$

where E is the energy of the particle and R is the orbit radius. The circular motion of the charged particles is ensured by the presence of 1232 dipole magnets, kept at a temperature of 1.9 K and providing an intense 8.4 T magnetic field. The beam focusing

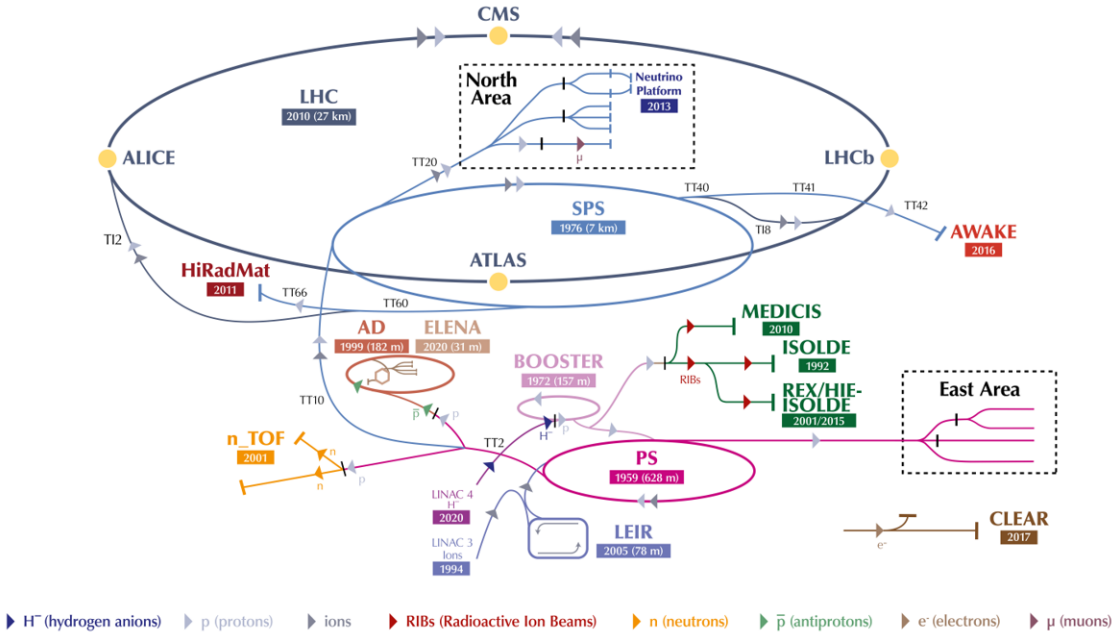

Figure 2.1: The complete accelerator complex at CERN, showing how the preliminary acceleration stages discussed for LHC are actually involved in several other experimental programs. A timeline and relevant dimensions are reported. Adapted from [25].

is instead ensured by 392 quadrupoles, kept at the same temperature and characterized by a maximum magnetic field of 6.9 T. In both cases, such intense magnetic field require the use of superconductors, namely cables composed of Niobium-titanium (NbTi) filaments, hence the need for the low temperatures provided by the cooling system, consisting in liquid helium.

2.2 LHC luminosity

In order to assess the performances of particle accelerators and colliders, it is customary to introduce some parameters. One of the most important is the *luminosity*. The luminosity is related to the number of events that can take place, according to

$$N_{events} = \sigma_{events} L = \sigma_{events} \int \mathcal{L}(t) dt \tag{2.2}$$

with σ_{events} being the cross section for the event under study, $\mathcal{L}$ the *instantaneous luminosity* and L the *integrated* luminosity [4].

The instantaneous luminosity in a collider is related to the number of bunches N_b circulating, the revolution frequency f, n_i number of particles contained in two colliding bunches and the transverse rms size of the beam in the horizontal σ_x and vertical σ_y directions at the interaction point by [14]

$$\mathcal{L} = \frac{N_b n_1 n_2 f}{4\pi\sigma_x\sigma_y} \times \mathcal{F} \tag{2.3}$$

where $\mathcal{F}$ is a factor of order 1 taking into account geometric (finite bunch length, crossing angle) as well as dynamical (mutual focusing of the two beams during the collision) effects [14]. The luminosity can be recasted in terms of the *emittances* (area of the ellipse in phase space containing the particles in the beam) ϵ and *amplitude functions* β^* at interaction point as

$$\mathcal{L} = \frac{n_1 n_2 N_b f}{4\sqrt{\epsilon_x\beta_x^*\epsilon_y\beta_y^*}} \tag{2.4}$$

From which we see that under the assumption of a $\mathcal{F}$ factor close to one, an high luminosity can be achieved for high bunches population collision, of low emittance (i.e. similar momenta) and high frequency, in a region where the amplitude function value is as low as possible [14]. Since 2017, LHC peak luminosity reached a value above 2 $\times 10^{34}$ cm^{-2} s^{-1}, more than twice its design value [14]. The High-Luminosity LHC was declared a top priority of the European Strategy for particle Physics in 2013 and should be operational starting from 2029. Its luminosity should reach a value over 10 times higher than the nominal design one, reaching a total integrated luminosity of the order of 3000-4500 fb^{-1} [29].

2.3 LHC experiments

As we have already mentioned, the two anti-rotating beams at LHC meet at some *interaction points*. LHC has eight arc and eight straight sections, where the latter are approximately 528 m long and can serve as experimental or utility intersection. Of the 8 sections, four are employed for the experiments ATLAS, ALICE, CMS and LHCb.

ATLAS (A Toroidal LHC ApparatuS) [3] is a general purpose detector that will be discussed in greater detail in the following.

ALICE (A Large Ion Collider Experiment) [30] is a general-purpose, heavy ion detector at LHC focusing on QCD. Beside working with Pb ions, it also studies light ions collisions, lower energy running and dedicated proton-nucleus runs. With dimensions of $16 \times 16 \times 26$ m^3 and a total weight of 10 000 t, the experiment consists of

18 detector systems, surrounding the interaction point, optimized for high momentum resolution and particle identification over a broad range of momenta.

The CMS (Compact Muon Solenoid) [31] experiment is conceived to study *pp* and lead-lead collisions. At the core of the CMS detector there is a high magnetic field and large bore superconducting solenoid. It surrounds the tracking system consisting in a silicon pixel and strip tracker together with the calorimeters, a lead tungstate scintillating crystal ECAL and a brass scintillator sampling HCAL. The overall dimensions of the CMS detecor are 21.6 m of length and 14.6 m of diameter, for a total weight of 12 500 t.

The LHCb (LHC beauty) [32] experiment is devoted to precision measurements of CP violation and rare B hadron decays. LHCb uses a series of subdetectors to detect *forward particles*, thrown forwards by the collisions in one direction. As usual, the first subdetector is mounted close to the collision point, and the other are progressively placed one after the other, over a length of 20 metres. The detector itself consists in a spectrometer magnet, a vertex locator system, a tracking system made of a Trigger Tracker (TT) silicon microstrip detector placed in front of the spectrometer magnet, three tracking stations behind the magnet made of silicon microstrips in the inner parts and Kapton/Al straw for the outher parts, two Ring Imaging Cherenkov counters (RICH), using Aerogel as radiators and an ECAL and an HCAL. Lastly, a muon detector system. LHCb dimensions are 21 m of length, 10 m of height and 13 m of width, for a total weight of 5 600 t.

2.4 LHC roadmap

Since the starting of its operations, LHC underwent a series of upgrades aiming to close the gap with the design parameters. The first LHC run started in 2011 and lasted until 2013. During the first run, LHC increased the maximum center of mass energy achievable going from an initial value of 900 GeV up to 7 TeV, reaching later a value of 8 TeV (cfr with the timeline in figure 2.2) [34]. In November 2012, LHC reached a peak instantaneous luminosity of 7.7 $\times 10^{33}\mathrm{cm}^{-2}\mathrm{s}^{-1}$, but still at half the design energy and twice the beam crossing time. The first LHC Pb-Pb collision took place in 2010, with a center of mass energy of 2.76 TeV, continuing to perform heavy ion collisions at said energies during the consecutive years [34]. The first data taking period corresponds to the so-called LHC *Run 1*, which has successfully ended in February 2013. This first stint culminated in the discovery of the Higgs boson, in 2012. Following Run 1, the first long shutdown (LS1) took place, aiming to perform the necessary upgrade in preparation for the Run 2.

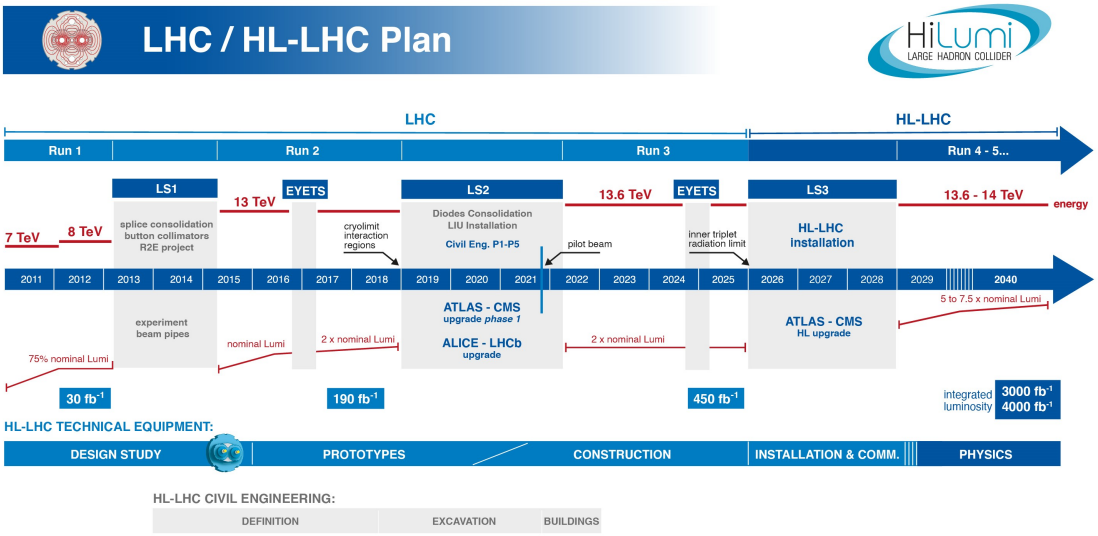

Figure 2.2: The LHC roadmap, as of February 2022. Every *Run*, periods in which data are collected, is alternated by a *Long Shutdown* period, here labelled as LS, in which upgrades are performed [33].

LS1 lasted from 2013 to 2015 and was motivated by the need to consolidate magnet interconnections. *Run 2*, started in 2015 and finished in 2019. Run 2 [35] was characterized by an higher center of mass energy of 13 TeV and a reduced bunch spacing of 25 ns, with overall improvement on the figures of merit. During this period was also reached an important milestone concerning LHC luminosity: in 2017 the nominal value of it was first reached and then surpassed, setting a record peak luminosity over twice the design value of $10^{34}\mathrm{cm}^{-2}\mathrm{s}^{-1}$ [14]. During the following LS2, which took place between 2019 and 2022, LINAC4 became the source of proton beams for the CERN accelerator complex, and several additional major upgrades were implemented, paving the road for *Run 3*.

Run 3 started in early 2022, and it is currently going on (at the time of writing). It was officially announced on July 5th of the same year, with a new record energy of 13.6 TeV. In the Run 3 period from 2022 to 2024, the LHC aims to further increase the integrated luminosity, with a present goal of 450 fb^{-1}, by the end of the run, well above the initial goal of 300 fb^{-1}. Finally, after the LS3 foreseen for the period 2026-2028, LHC is supposed to reach the design value of 14 TeV or further close the gap with it, with a luminosity 5 to 7.5 larger than the nominal value, corresponding to a final goal integrated luminosity of 3000-4500 fb^{-1} [33].

2.5 The ATLAS experiment

ATLAS is a general purpose detector, built for probing *p-p* and Pb-Pb collisions [3]. It is the largest volume particle detector ever constructed [36], with 46 meters of length, 25 of height, 25 of width and 7000 tonne of weight. It sits 100 m underground, in correspondence of the so-called *point 1* of LHC. The ATLAS experiment is conducted as a joint effort of more than 5500 scientists from 245 institutes in 42 countries [36] .

The present section aims to provide an overall description of the ATLAS detector and of the sub-detectors it is composed, according to general design of Run 2.

2.5.1 Detector Overview

The ATLAS detector adopts a specific coordinate system and nomenclature [3]. The nominal interaction point (*IP*) is considered to be the origin of the coordinate system. The detector possesses a forward-backward symmetry with respect to the IP point. The z-axis is defined by the beam direction, leaving the x-y plane as the one orthogonal to it (*transverse plane*). The x-axis is taken to be as the one pointing from the interaction point to the centre of the LHC ring, while the positive y-axis points upwards. Detector's *side-A* is the one in which z is positive, while *side-C* is the one with negative z. The *azimuthal* angle ϕ is measured around the beam axis, while the *polar* angle θ is the angles from the beam axis. Assuming the initial transverse momentum p_T of the beam (in the xy plane) to be negligible, the final p_T has to satisfy:

$$\sum p_T \simeq 0, \qquad p_T = \sqrt{p_x^2 + p_y^2}$$

In order to deal with quantities which are invariant under Lorentz boost along the beam axis[1], it is customary to introduce the *rapidity*

$$y = \frac{1}{2} \ln \left(\frac{E + p_z}{E - p_z} \right) \tag{2.5}$$

and the one of *pseudorapidity*

$$\eta = -\ln \left[\tan \frac{\theta}{2} \right] \tag{2.6}$$

where the latter is more convenient to deal with experimentally, and represents the relativistic (m $\ll p_T$) limit of the rapidity. Using these variables, we can consider a (η,ϕ,z) space, where the distances in the transverse $\eta - \phi$ are defined according to

[1] under a boost along the z axis, rapidity transforms in a convenient form: the transformed quantity is obtained by the starting one via addition of a fixed term, thus rapidity *differences* are invariant

$$\Delta R = \sqrt{(\Delta\eta)^2 + (\Delta\phi)^2} \tag{2.7}$$

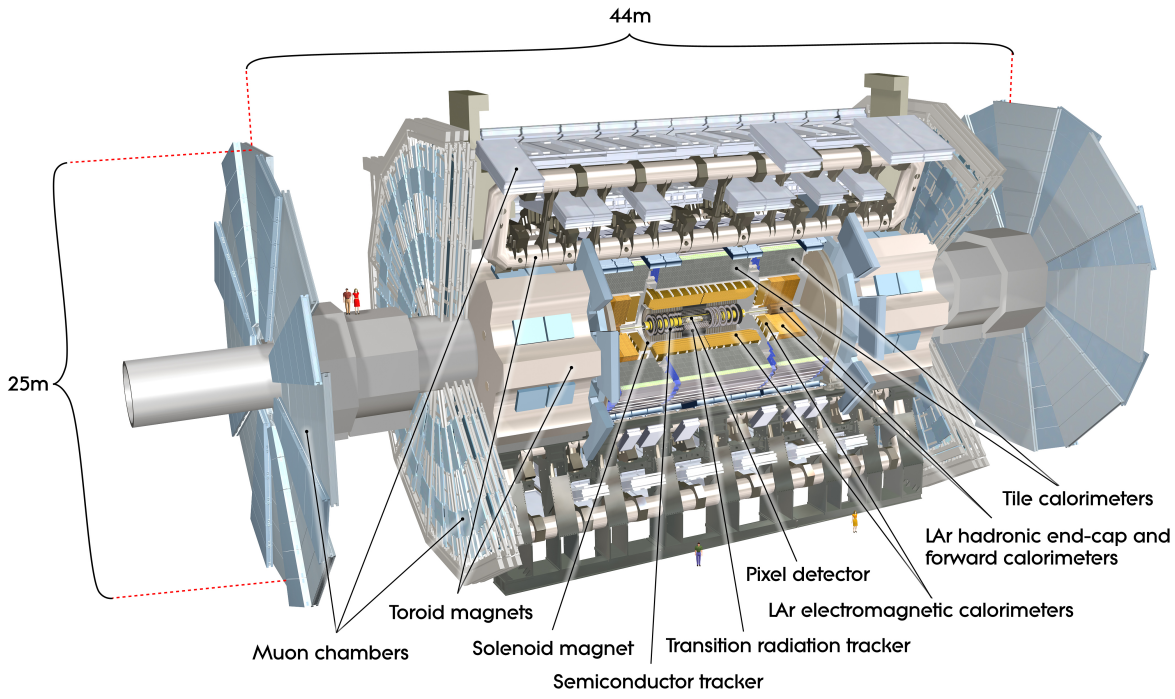

Figure 2.3: ATLAS detector cut-away view [37] .

The LHC detectors have to satisfy some common general requirements, dictated by experimental conditions and ultimate goals of the research carried on, in order to allow the identification and reconstruction of the physical phenomena under investigation. Most notably, detectors are required to have:

1. *Electronics and sensor elements*: the detectors require fast, radiation hard electronics and sensor elements. Moreover, in order to handle the particle fluxes and reduce the influence of overlapping events, high detector granularity is necessary.

2. *Geometrical acceptance*: the detector needs large acceptance in pseudorapidity with almost full azimuthal angle coverage.

3. *Momentum resolution and reconstruction efficiency*: It is essential that the detector possesses good charged particle momentum resolution and reconstruction efficiency.

4. *Calorimetry*: Very good EM calorimetry for e^- and photon identification and full-coverage hadronic calorimetry for jet and missing transverse energy measurements.

5. *Triggering*: Triggering on low transverse momentum objects must be highly efficient and with a sufficient background rejection capability.

6. *Muon detection*: good muon indentification and momentum resolution. It is crucial to be able to identify without ambiguity high transverse momentum muons.

A summary of the ATLAS detector main performance goals is shown in table 2.1, while figure 2.3 provides a cut-away view of the complete detector .

Table 2.1: Summary of general performance goals of the ATLAS detector. The muon spectrometer performance is independent of the inner detector system for high p_T muons. E and p_T are expressed in GeV [3].

Detector Component	Resolution	η coverage	
		Measurement	Trigger
Tracking	$\sigma_{p_T}/p_T = 0.05\%\ p_T \oplus 1\%$	± 2.5	
EM calorimeter	$\sigma_E/\mathrm{E} = 10\%/\sqrt{E} \oplus 0.7\%$	± 3.2	± 2.5
Hadronic Calorimetry			
barrel and end-cap	$\sigma_E/\mathrm{E} = 50\%/\sqrt{E} \oplus 3\%$	± 3.2	± 3.2
forward	$\sigma_E/\mathrm{E} = 100\%/\sqrt{E} \oplus 10\%$	$3.1 < \lvert\eta\rvert < 4.9$	$3.1 < \lvert\eta\rvert < 4.9$
Muon Spectrometer	$\sigma_{p_T} = 10\%$ at $p_T = 1$ TeV	± 2.7	± 2.4

Several *sub-detectors* have been designed in order to satisfy the criteria discussed. They are arranged around the beam axis according to a cylindrical geometry, covering each a given pseudorapidity range.

Considering for reference fig 2.4, the closest to the beam axis is the *inner detector*, immersed in a 2 T solenoidal magnetic field. The inner detector is devoted to momentum

and vertex measurement as well as to pattern recognition and electron identification. It makes use of high resolution semiconductor pixel and strip detectors in the innermost part of the tracking volume and of straw tube tracking detectors in the outer part.
The *electromagnetic calorimeter* (ECAL) is an high granularity liquid argon (LAr) sampling calorimeter, characterized by excellent energy and position resolution. The *hadronic calorimeter* (HCAL) consists in a scintillator-tile calorimeter, divided into a large central barrel and two smaller and extended ones, on either side of the first one. The muon spectrometer surrounds the calorimeter, and represents the very last subdetector system of ATLAS.

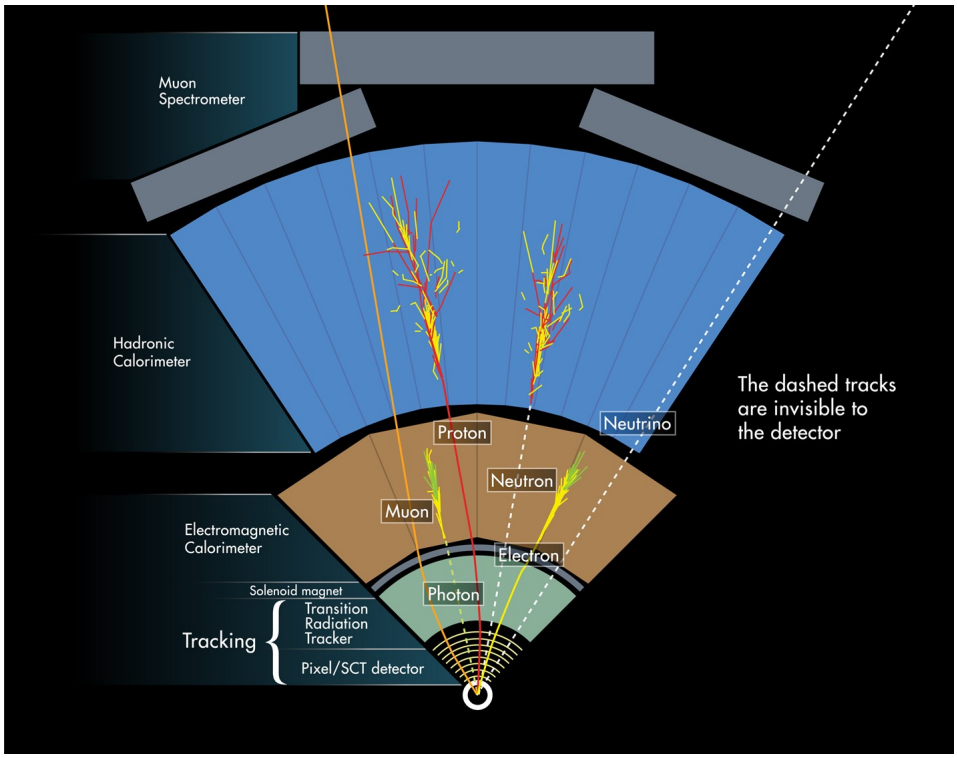

Figure 2.4: Section of the ATLAS detector, with corresponding sub-detector's relative expected signature for selected particles. (©CERN).

2.5.2 Tracking

The Inner Detector (ID) extends over a length of 6.2 m and has a diameter of 2.5 m. It consists of three independent sub-detectors, the *pixel* and *silicon microstrip trackers* (SCT) together with straw tubes of the *Transition Radiation Tracker* (TRT), immersed in the 2 T magnetic field produced by the central solenoid. Exploiting the information

provided by the bending particles trajectories, the ID allows to obtain measurements of particles tracks and electric changes. A cut-away view of the ID is shown in figure 2.5, while figure 2.6 shows the layout of the ID.

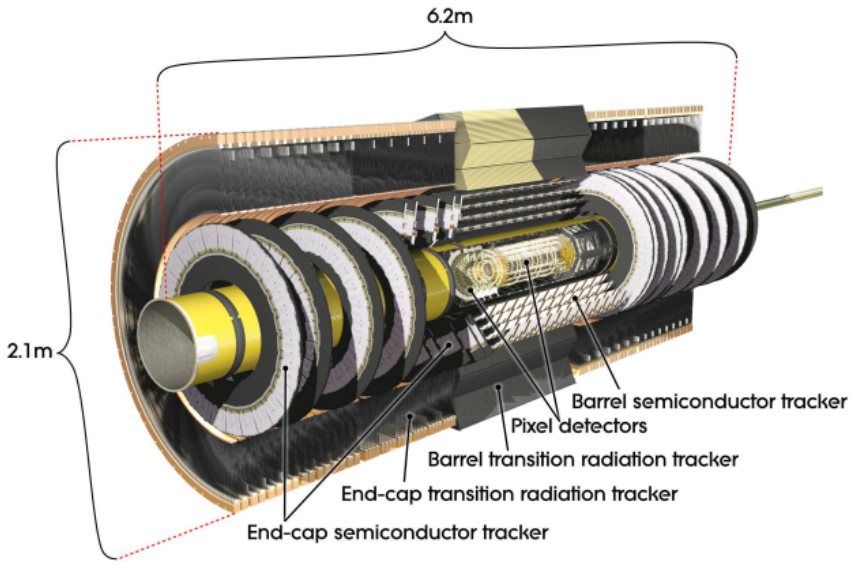

Figure 2.5: Cut-away view of the ID. [3]

Pixel and SCT are the precision tracking detectors and cover a region corresponding to $|\eta| < 2.5$. They are present both in the barrel region, where they are mounted in a concentric cylinders arrangement around the beam axis, and in the end cap regions, placed on disks perpendicular to the beam pipe.

In particular, the pixel detector is the closest to the beam pipe, at a distance of just 3.3 cm, representing the first point of detection. It is composed by 4 layers, called *B-Layer*, *Layer-1*, *Layer-2* and the *Insertable B-Layer* (or IBL), segmented in the R-ϕ and z plane. The individual pixel size is of the order of 50 $\times 400$ $\mu\mathrm{m}^2$ in said plane for all but the IBL, having size 50 $\times$ 250 $\mu\mathrm{m}^2$. The intrinsic accuracies are of 10 μm (R-ϕ) and 115 μm (z) in the barrel and 10 $\mu\mathrm{m}$ (R-ϕ) and 115 μm (R) in the disks.
The semiconductor tracker or SCT consists in 4088 silicon strip sensor modules, divided into four layers in the barrel and nine disks for each endcaps. In the barrel region, this detector exploits small angle stereo strips (40 mrad) to measure both coordinates and one set of strips in each layer along the beam direction in order to provide an R-ϕ measurement. For the end cap region instead, the detectors have strips disposed radially and a set of stereo strips at a 40 mrad angle. The intrinsic accuracies per module are of 17 $\mu\mathrm{m}$ (R-ϕ) and 580 $\mu\mathrm{m}$ (z) and 17 μm (R-ϕ) and 580 $\mu\mathrm{m}$ (R) in the barrel and end caps respectively. For both, the mean strip pitch is 80 $\mu\mathrm{m}$.

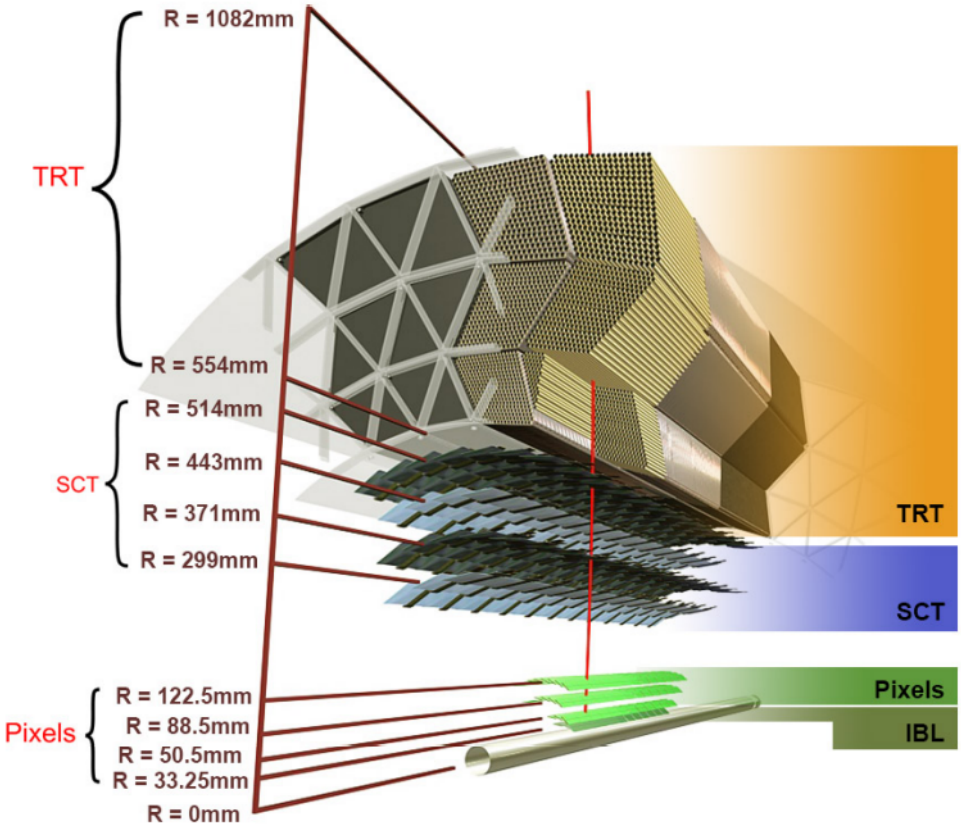

Figure 2.6: Section of the ATLAS ID. [3]

The Transition Radiation Tracker is the outermost sub-detector composing the ID. It consists of polyimide drift tubes (*straws*) with a 4 mm diameter, filled with a gas mixture of 70% Xe 27% CO_2 3% O_2, located as for the previous sub-detector both in the barrel and end caps. In the barrel region, these straws are parallel to the beam axis and 1.44 m long, whereas in the end cap part they are arranged radially in wheels, and 37 cm long. The TRT only provides R-ϕ information, with an accuracy per straw of 130 μm.

2.5.3 Magnet system

The ATLAS magnet system allows to achieve an accurate track reconstruction and momentum measurement. More specifically, the relation between the radius of curvature ρ of the trajectory a particle with electric charge q and momentum $\mathbf{p}$, traversing a magnetic field of intensity B, can be determined from the Lorentz force:

$$\rho = \frac{|\mathbf{p}|}{qB}$$

The ATLAS magnet system consists of one solenoid and three toroids, with the latter located one in the barrel and two in end-caps, all consisting in superconducting magnets. The total diameter of the magnet system is 22 m and its total length amounts to 26 m. Figure 2.7 shows the layout of the magnet system.

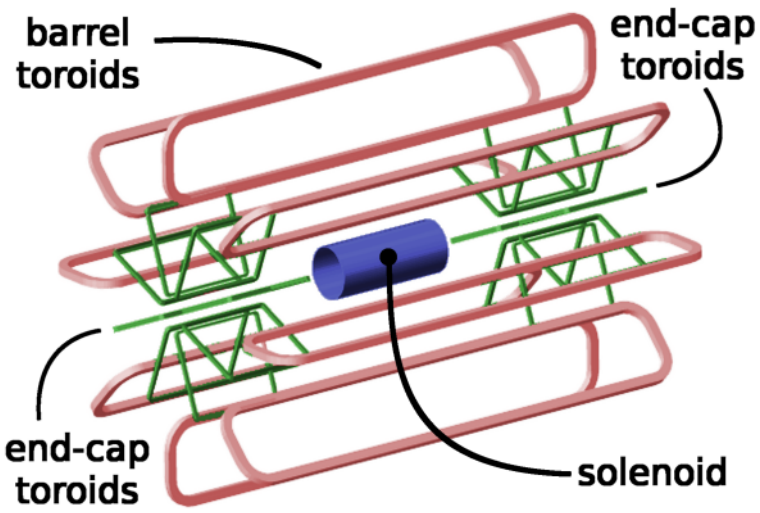

Figure 2.7: Geometry of the magnet system. The eight barrel toroid coils, with the end-cap coils interleaved are visible. The solenoid lies insied the calorimeter volume. [3]

The solenoid is aligned to the beam axis, providing the 2 T field for the ID, as discussed previously. The inner and outer diameters are 2.46 m and 2.56 m respectively, for an axial length of 5.8 m. The coil mass is 5.4 tonnes, and it is kept at a temperature of 4.5 K. On the other hand, the toroids provide a 0.5 T and a 1 T magnetic field for the muon spectrometer respectively in the central and end-cap regions. The barrel toroid consists of eight coils encased in individual racetrack-shaped vacuum vessels. It has a length of 25.3 m with outer and inner diameters respectively of 20.1 m and 9.4 m. The end-cap toroids system is rotated by $22.5°$ with respect to the barrel toroid coil system[2] and they have a 5.0 m axial length for a 10.7 m outer diameter [38] . In total, they generate a magnetic field extending over a volume of approximately 12 000 m^3.

[2]This allows to obtain radial overlap and improve the bending power at the interface between the two coil systems [3]

2.5.4 Calorimeters

The ATLAS calorimeter system has the goal to provide destructive measurement of the particle energies, jet reconstruction and measurements of E_T^{miss}, exploiting the electromagnetic and hadronic calorimeters it is composed by. The ATLAS calorimeters are required to provide good containment for *Electromagnetic* and *Hadronic* showers. It is critical in this sense the depth of the calorimeters. The total thickness for the ECAL is larger than 22 *radiation lengths* X_0 in the barrel and larger than 24 X_0 in the end caps. Correspondingly, we have 9.7 *interaction lenghts* λ of active calorimenter for the barrel and 10 λ in the end caps for the case of jets. An overview of the ATLAS calorimeter system is presented in figure 2.8.

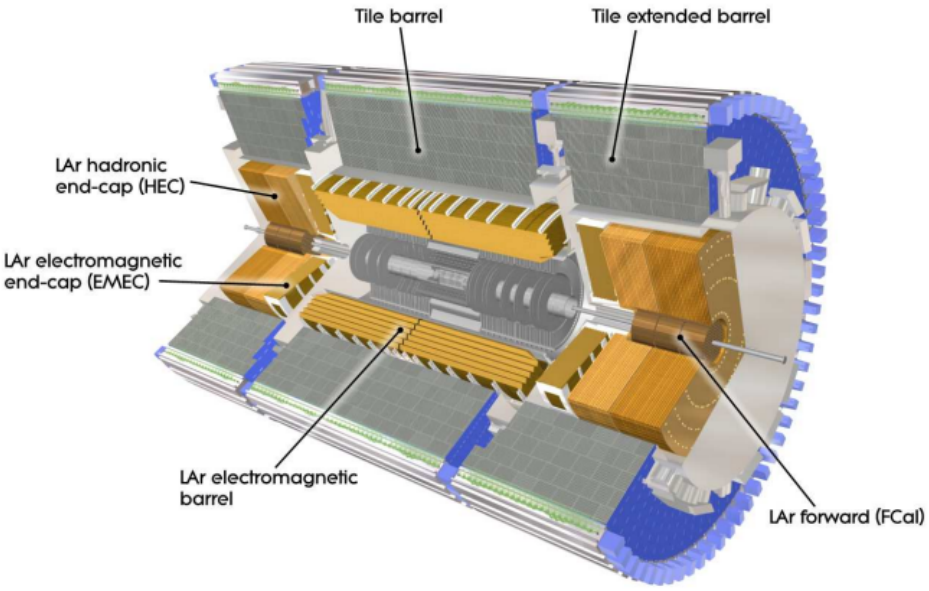

Figure 2.8: The ATLAS calorimeter system. [3]

The calorimeters cover a large η range corresponding to $|\eta| < 4.9$. The finer granularity region overlaps the ID η range, with the goal to provide precision measurements on electrons and photons. For the rest of the calorimeter, the requirement for the granularity is to be sufficient in order to achieve jet reconstruction and E_T^{miss} measurements.

LAr Electromagnetic Calorimeter

The ECAL is a lead-LAr sampling calorimeter with a characteristic accordion geometry, show in figure 2.9 . A cryostat[3] encloses the two parts in which the ECAL is

[3]This is necessary in order to maintain argon in liquid form. The temperature reached is -184°C.

divided: the barrel part, with $|\eta| < 1.475$ and the two end caps, with $1.375 < |\eta| < 3.2$. In turn, the barrel calorimeter is divided into two identical halfs, with a small gap of 4 mm at z$= 0$. The end cap calorimeter too consists of two coaxial wheels, with the outer one covering the interval $1.375 < |\eta| < 2.5$ and the inner one the range $2.5 < |\eta| < 3.2$. A presampler detector consisting in an active 1.1 cm (0.5 cm) layer of LAr is used in the barrel (end caps) region, for $|\eta| < 1.8$, in order to correct for the energy lost by electron and photons in the upstream of the calorimeter.

The energy resolution of the ECAL barrel part was measured to be [3]

$$\frac{\sigma_E}{E} = \frac{10.1\%}{\sqrt{E}} \oplus 0.17\% \tag{2.8}$$

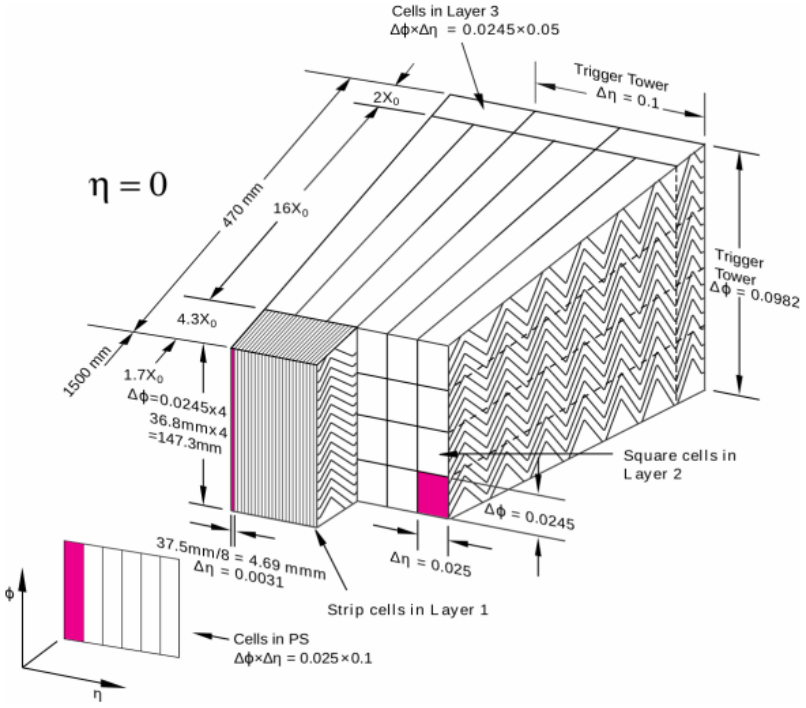

Figure 2.9: Representation of the barrel module of the ECAL, showing the accordion geometry. The granularity in η and ϕ cells, for each of the three layers and of the trigger tower is reported. [3]

where here $\oplus$ represents the sum in quadrature of the stochastic and constant term. Similar results have been obtain for the end cap calorimeter (EMEC).
The full barrel ECAL region is structured into three layers, corresponding to:

1. *Inner Layer*: 4.3 X_0 long, strip composed region of $\Delta\eta = 0.0031$, which is used for charged and neutral pion discrimination;
2. *Middle Layer*: 16 X_0 long, composed by squared towers of $\Delta\eta \times \Delta\phi = 0.025 \times 0.025$ dimension;
3. *Outer Layer*: composed by $\Delta\eta \times \Delta\phi = 0.050 \times 0.025$ towrs, was designed for EM showers of energy larger than 50 GeV;

Hadronic Calorimeter

The HCAL is composed by a *Tile calorimeter*, an *Hadronic End-cap Calorimeter* (HEC) and a *Forward Calorimeter* (FCal).

The tile calorimeter is placed immediately outside the ECAL envelope. It is composed by a tile barrel and two extended barrels (figure 2.8). Its barrel covers the region $|\eta| < 1.0$ and the two extended ones the interval $0.8 < |\eta| < 1.7$. It is a sampling calorimeter with scintillating tiles as active material and steel as absorber. Radially, it extends between 2.28 and 4.25, respectively the inner and outer radius.

The HEC is a sampling calorimeter consists of two independent wheels per end cap, directly behind the end-cap ECAL, sharing the same cryostat. It extends to $|\eta| = 3.2$, overlapping with the forward calorimeter and (slightly) with the tile calorimeter, by extending to $|\eta| = 1.5$.
25 mm parallel copper plates are used to build the wheels closest to the interaction point. Those further away use 50 mm copper plates. These copper plater are alternated with 8.5 mm LAr gaps, serving as active medium. The outer radius of the copper plates is 2.03 m, the inner one is 0.475 m, with an exception in the overlap region where the radius is 0.372 m.

The FCal is approximately 10λ lengths deep and consists in three modules in each end cap. It is located very close to the beam pipe, covering the region $3.1 < |\eta| < 4.9$. The first module is made of copper and optimised for electromagnetic measurements. The other two are made of tungsten and are devoted predominantly for energy measurements of showers developing after hadronic interactions. Once again this is a sampling calorimeter using LAr as active medium.

2.5.5 Muon System

A dedicated subsytem for muons is required since they manage to traverse the innermost layers of the detector discussed so far. The *muon spectrometer* is designed to

detect and measure the momenta of muons exiting from the end-caps and barrel in the pseudorapidity range < 2.7 . Moreover, the muon spectrometer provides the *trigger* on these particles for $|\eta| < 2.4$. Figure 2.10 shows an overview of the muon system. The spectrometer itself is divided into four subsections : the *Cathode Strip Chambers* (CSC) , the *Monitored Drift Tubes* (MDT) , the *Thin-Gap chambers* (TGC) and lastly the *Resistive Plate Chambers* (RPC) , with the first two corresponding to the *precision chambers* and the last two to the *trigger chambers*.

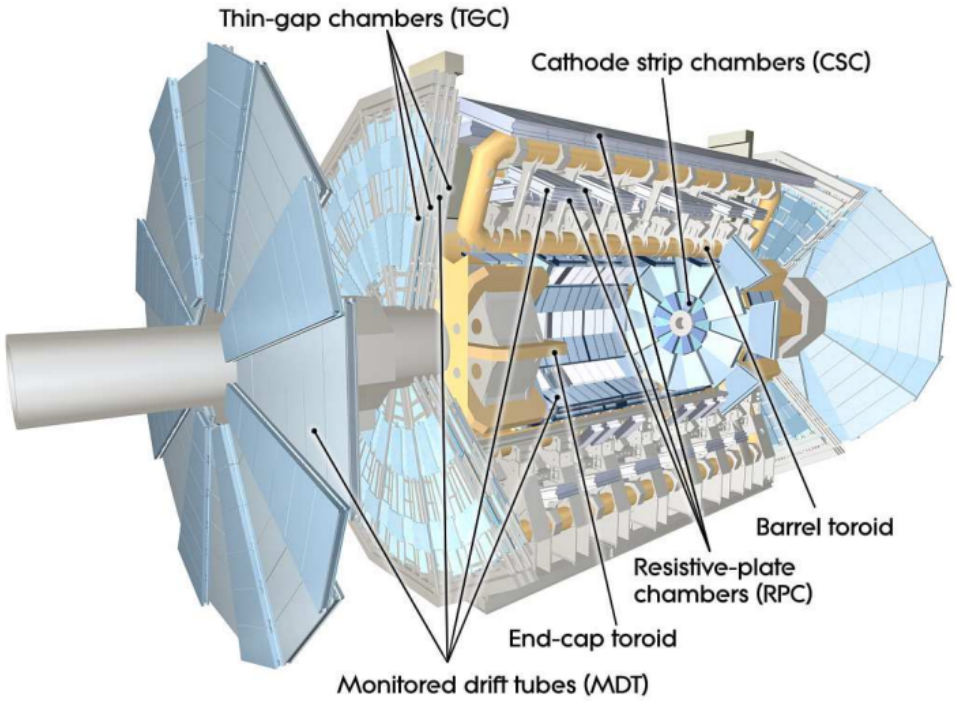

Figure 2.10: ATLAS muon system components. [3]

The MDT [39] are drift chambers consisting in layers of Al drift tubes of 29.97 mm diameter, filled with an Ar-CO_2 mixture, designed to provide precise measurement of the track coordinates. The chambers are operated at a 3 bar pressure. They cover the pseudorapidity range $|\eta| < 2.7$, with the exception of the innermost end cap layer having coverage limited to $|\eta| < 2.0$. The average spatial resolution per tube si of 80 μm or about 35 μm per chamber.
These MDT are complemented by the CSC, which are multi-wire proportional chambers with strip cathodes, aiming to measure muon momenta in the range $2.0 < |\eta| < 2.7$. The spatial resolution of a chamber is 60 μm in the bending plane and 5 mm in

the non bending direction, while the time resolution is about 7 ns.

The TGC are used in the end cap regions, for $1.05 \leq |\eta| \leq 2.7$ (2.4 for triggering). They operate on the same principle of multi-wire proportional chambers, providing good time resolution and high rate capability. They allow the determination of the second (azimuthal) coordinate, complementary to the one measured by the MDT. They are filled with a higly quenching gas mixture of 55% CO_2 and 45% n-pentate C_5H_{12}. Both TGC and RPC provide a spatial resolution between 5-10 mm [40] (2-6 mm in the R coordinate and 3-7 mm in the ϕ one for TGC [3]) . TGC are also characterized by a time resolution of 4 ns.

The RPC are gaseous parallel electrode plate (wireless) detector. Placed on the barrel region, they cover $|\eta| \leq 1.05$. The two resistive plates are held at a distance of 2 mm one from the other by insulating spacers. A 4.9 kV/mm electric field between the plates allows for avalanches formation along the ionizing tracks towards the anode. Their time resolution is 1.5 ns.

2.5.6 Forward detectors

ATLAS forward region is covered by additional smaller sub-detectors, from the closest to farthest to the interaction point: LUCID (LUminosity Cherenkov Integrating Detector), ZDC (Zero-Degree Calorimeter), AFP (ATLAS Forward Proton) and ALFA (Absolute Luminosity For ATLAS). as shown in figure 2.11.

LUCID allows to perform luminosity monitoring. It consists of aluminium tubes placed symmetrically around the beam pipe, and located at a distance of approximately 17 m from the interaction point. The original design of the LUCID-1 tubes was characterized by the fact that they were filled with C_4F_{10} at a pressure of 1.2-1.4 bar .The Cherenkov radiation emitted by a particle traversing the tube was thus detected by 16 photomultiplier tubes (PMTs). Following the upgrade to LUCID-2, the thin quartz windows of the PMTs have been adopted directly as the Cherenkov medium. Moreover, the addiction of small amounts of radioactive ^{207}Bi sources deposited on the windows allows to monitor PMTs performances [42].

ZDC aims to detect forward neutrons produced in heavy ion collisions, in a region $|\eta| > 8.3$. There are four ZDC modules installed per side, with the first one corresponding to the electromagnetic module consisting in tungsten plates with faces perpendicular with respect to the beam pipe and quartz rods, penetrating the plates, parallel to the beam. The rods are viewed by phototubes capturing the Cherenkov light from shower products. Above the tungsten plates are placed, in order, quartz

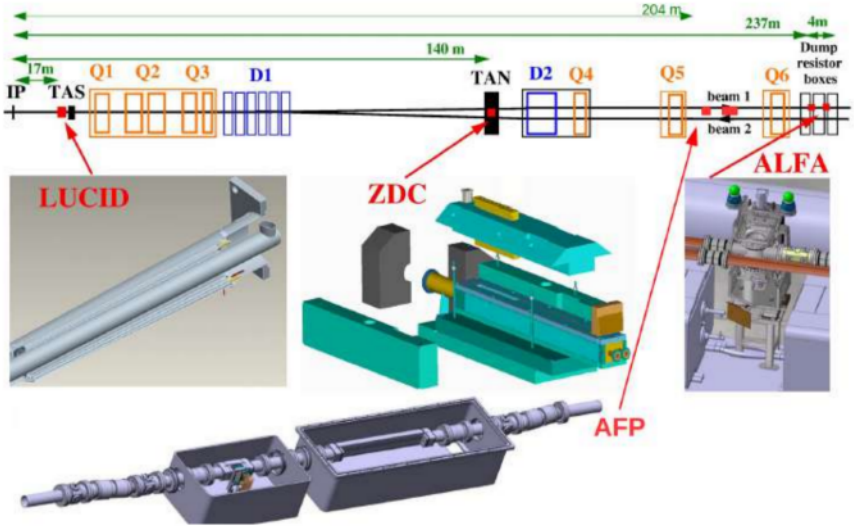

Figure 2.11: ATLAS forward detectors system. [41]

strips and steel plates, with the former viewed from above by photomultiplier tubes. The EM module is approximately 29 X_0 deep. The hadronic modules are similar, with a depth of approximately 1.14 λ.

AFP [43] detector pursues the goal to perform measurements on protons emitted from a central interaction in the very forward directions. It is composed by a silicon tracker and a TOF subsystems, placed once again symmetrically with respect to the interaction point, to perform measurements of energy and momentum of the proton.

ALFA [44] is located at approximately 240 m from the interaction point, making it the most remote detector. It based on staggered layers of square shaped scintillating fibers read by *multi-anode photomultiplier tubes* (MAPMTs), inside so-called *Roman pots*, consisting in thin-walled vessels separated from the vacuum of the accelerator by a window and such that they can be moved closer to the beam itself, up to a millimetre distance from it. The fibers are then "read out" by PMTs.

2.5.7 Trigger and Data Acquisition

The *Trigger and Data Acquisition* [3, 46] system is devoted to the selection (trigger) of events occurring in the detector and the collection of data relative to such events, conversion in an appropriate format and their storage (data acquisition). The Trigger and Data Acquisition systems are collectively referred to as TDAQ. The ATLAS TDAQ system is responsible for the online processing, selection and storage of events

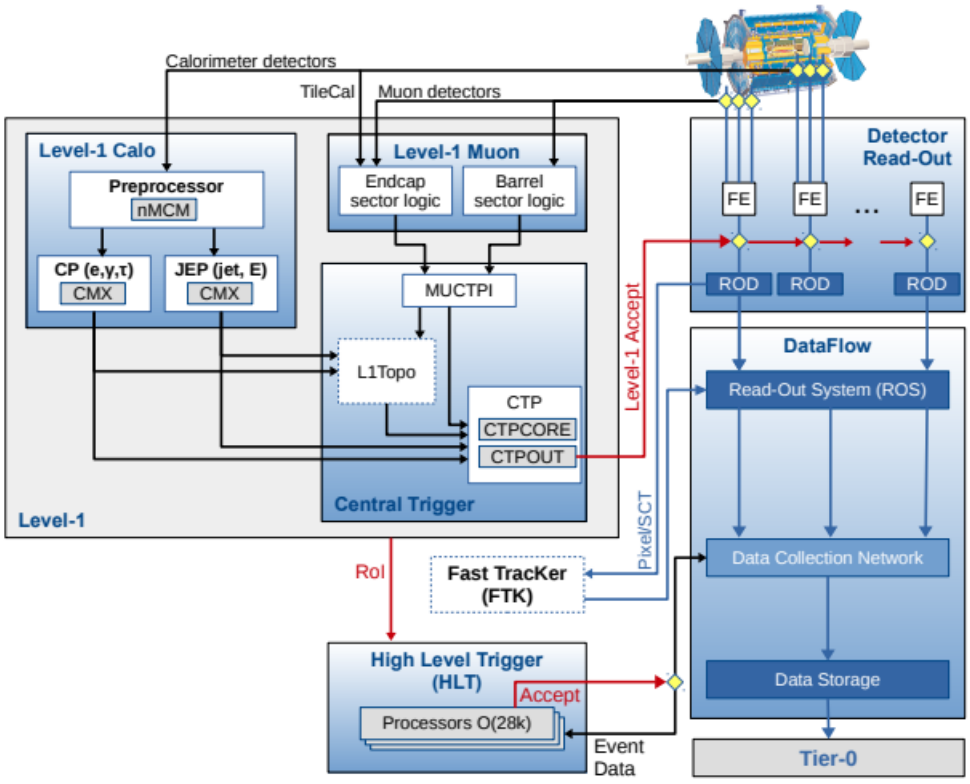

Figure 2.12: The ATLAS TDAQ system in Run 2 from [45]

of interest of the offline analysis, and it is shown in figure 2.12 [47].
The ATLAS trigger system is composed by two distinct levels, the *Level 1* (L1) and the *High Level Trigger* (HLT). Each level refines the decision made at the previous one and, whenever necessary, applies additional selection criteria. The L1 trigger is a hardware based system, making use of custom electronics to trigger on information from the calorimeter and muon detector. To this purpose, a L1 calorimeter (L1Calo) and L1 muon (L1Muon) system are introduced.

The L1Calo takes signals from the calorimeter as input. The analogue detector signals are then digitalised and calibrated in the preprocessor. Thus they are sent in parallel to the Jet/Energy-sum Processor (JEP) and the Cluster Processor (CP). The JEP identifies jet candidates, and evaluates global sums of total and missing transverse energy. The CP system instead is devoted to the identification of electron, photon, and τ can-

didates above a programmable threshold. The L1Muon trigger instead makes use of hits from the RPCs and TGCs, respectively in the barrel and endcaps, in order to evaluate the deviation from the hit pattern from the one of muons with infinite momentum. The L1Muon system applies coincidence requirements between the outer and inner TGC stations, and between the TGCs and tile calorimets, in order to reduce the rate in the endcap regions of particles not originating from the IP.

The L1 trigger decision is then formed in the *Central Trigger Processor* (CTP), receiving inputs from the L1Calo and L1muon, via the *L1Muon Central Trigger processor Interface* (MUCTPI) and the L1 topological trigger (L1Topo), as well as from other detector subsystems (LUCID, ZDC, MBTS,etc). The CTP has also the role of applying the *dead time*, which limits the number of L1 accepts to be within constraints on detector read-out latency. The L1 trigger event selection can be based either on event-level quantities, like the total energy deposited in the calorimeter, the multiplicity of objects above thresholds, like the transverse momentum o a muon, or particular topological requirements, like invariant masses or angular distances. The L1 trigger accepts events at a rate up to the maximum detector read-out rate of 100 kHz, within a latency of 2.5μs, reduced from the starting 40 MHz.

Following each L1-accepted, the corresponding event data are read out by the Front-End electronics, from all detectors. The data are sent to the *ReadOut Drivers* (RODs), which make the initial processing and formatting. Following the RODs, the data are sent to buffer to the *ReadOut System* (ROS). Moreover, the L1 identifies the *Regions of Interest* (RoIs), in η and ϕ, witihin the detector, to be investigated in the next trigger stage,the HLT, where data are sent by the ROS

The HLT is software-based, and applies typical reconstruction sequences considering first fast, dedicated trigger algorithms for early rejection, followed by more precise, CPU-intensive ones, similar to those of the offline reconstruction, to make the final selection. The execution of these algorithm takes place on a dedicated computing farm, of approximately 40 000 selection applications, called Processing Units (PUs), which are designed to make decisions within few hundreds milliseconds. The physics output rate of the HLT is of 1.2 kHz on average, with a corresponding average throughput of 1.2 GB/S to the permanent storage. When an event is finally accepted by the HLT, the Sub-Farm Output (SFO) send the data to the permanent storage for the offline reconstruction and for being exported to the Tier-0 facility at CERN computing center.

Chapter 3

Object Reconstruction

The reconstruction and identification of objects produced in pp collisions represents the first, necessary, level of any ATLAS physics analysis. Following this procedure, information on the physical objects of interest, such as electrons, photons, muons and jets is obtained, by exploiting the technologies described in the previous chapter. The goal of the present chapter is to provide an overview on how object reconstruction is performed by the ATLAS collaboration, considering explicitly the case of electrons, muons and jets, which are of interest for the Chapter 4.

3.1 Track Reconstruction

Track reconstruction [48] has its basic building block in the *hits* in one of the ID tracking layers. Observed hits are then assembled into *clusters*. Clusters formed as a consequence of one charged particle deposit are called *single particle clusters*. However, in a dense environment with high pile-up such as the ATLAS case, multiple particles can be responsible for the formation of the same cluster. In this case we talk about *merged clusters*. Figure 3.1 shows an example of the two classes.

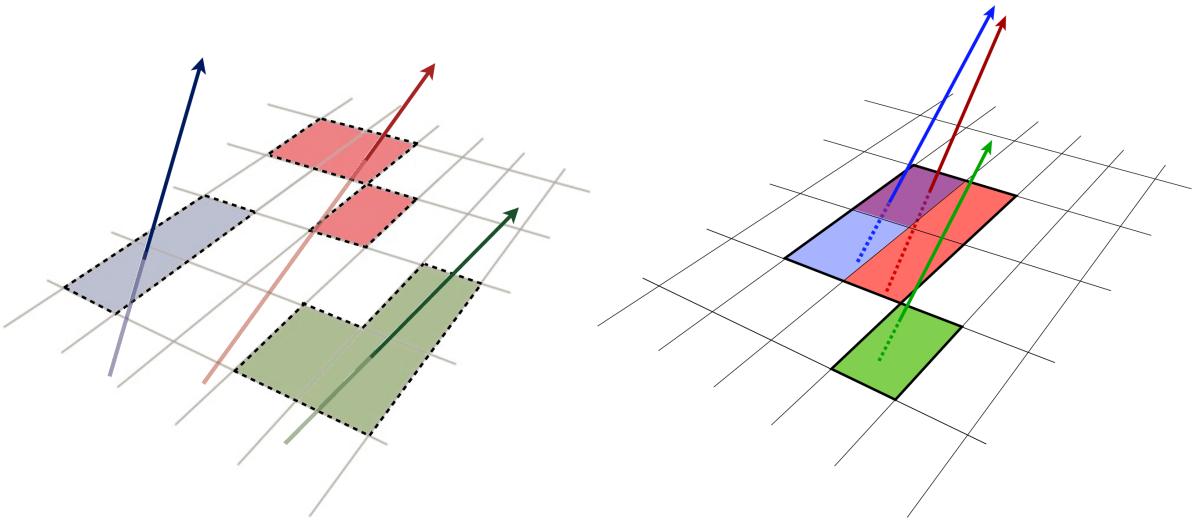

(a) (b)

Figure 3.1: Examples of a single particle cluster (a) and merged cluster from very collimated particles (b). Different colours represent energy deposits from different charged particles traversing the sensor and the particles trajectories are shown as arrows [48].

On turn, combining clusters a three dimensional measurement is obtained - the so-called *space-points*. For the pixel detector, to each space-point correspond a single cluster, while in the SCT, clusters from both side of a strip layer must be combined.
To form a *track seed*, sets of three space-points are used. The candidate track is build via a Kalman filter [49], adding further space-points from the remaining layers of the pixel and SCT detector, compatible with the preliminary trajectory. To each seed are associated multiple track candidates, for each compatible space point extension on the same layer.

Next, in the *ambiguity solver*, tracks are assigned a *track score*, which provides a measure of the track quality. The criteria according to which the scores are assigned are the

number of holes, the number of clusters associated to the track and the χ^2 of the track fit. The score defines the order in which the tracks are processed, favoring those with higher scores. Following the score assignment, the ambiguity solver deals with clusters assigned to multiple track candidates. Shared clusters are counted by comparing track candidates with those tracks previously accepted by the ambiguity solver. Clusters are required to be not shared between more than two tracks. Moreover, if a track contains more than two shared clusters is rejected.

The last step consists in the *TRT track extension* [50], in which track segments are extended from the silicon detector to the outer TRT. The process takes place in two step: first the candidates are searched, then the extensions are processed and evaluated. The procedure for the TRT extension is performed according to an *inside-out* scheme, i.e. from silicon detectors (SCT and pixel) to the TRT. In the circumstances in which no track candidate could be found in this scheme, for instance if ambiguous hits cause the track seed in silicon detector to have an insufficient score, such that they do not to survive the ambiguity solver step, an *outside-in* sequence is considered, starting from the TRT and moving inward, to the silicon detector.

3.2 Vertex reconstruction

Primary vertex reconstruction [51] is performed via grouping all the tracks that passed the reconstruction procedure. Vertex candidate reconstruction is a two stage process: the *vertex finding* and the *vertex fitting*. First, a set of tracks passing the selection criteria is identified. Then, the seed position for the vertex is selected as the one closest to the beam spot. Using an iterative χ^2 minimization, where in each iteration the less compatible tracks are down-weighted and the vertex position is recomputed, the best vertex position is determined. Tracks which are incompatible with the vertex at 7 σ are rejected, and then considered as input for new vertex finding iterations. The procedure is then repeated for every remaining tracks in the event. The vertex corresponding to the highest sum of squares of transverse momenta ($\sum p_T^2$) is assumed to be the primary one, while the others are considered pile-up vertices.

3.3 Electrons

3.3.1 Reconstruction

Electron candidate reconstruction in the precision region of the ATLAS detector, corresponding to $|\eta| < 2.47$, is based on three signatures: localised energy clusters deposit in the ECAL region, charged particle tracks in the ID region and close matching of the

two in the $\eta \times \phi$ space [52].

Concerning the *Seed-cluster reconstruction*, the $\eta \times \phi$ region occupied by the ECAL is divided into a $\times$ 256 grid of elements, called *towers*, of size $\Delta\eta \times \Delta\phi = 0.025 \times 0.025$. The energy of each tower is obtained by summing the contributions collected in the first, second and third layer of the calorimeter, as well as in the pre-sampler, located at the $|\eta| < 1.8$. Energy cluster candidates are then seeded from combined towers showing a summed transverse energy larger than 2.5 GeV. Ambiguity between overlapping seed-cluster candidates is solved by retaining the candidate of higher transverse energy if E_T is at least 10% higher than the other one, or keeping the candidate containing the highest E_T central tower, if their transverse energy values are within 10%. Finally, the matching is performed, considering as criterion the (η,ϕ) distance of the cluster and track. An example of the electron reconstruction efficiency as a function of the electrons' transverse energy is shown in figure 3.2.

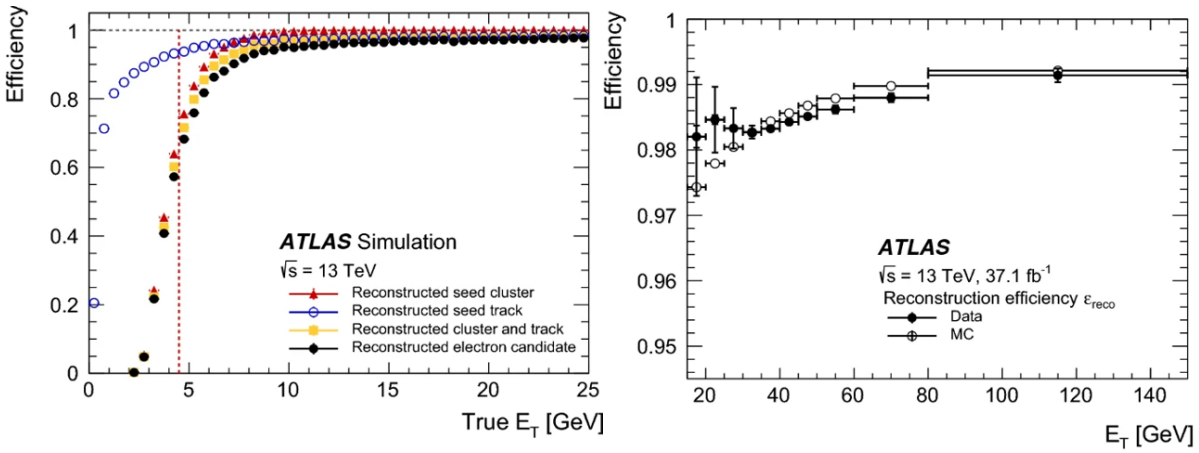

(a) (b)

Figure 3.2: Left: Total reconstruction efficiency for simulated electrons in a single-electron sample, as a function of the true (generator) transverse energy, for each step of the candidate formation. The total reconstruction efficiency is less than total 60% below 4.5 GeV (dashed line). Right: reconstruction efficiency relative to reconstructed clusters, as a function of the electron transverse energy, for $Z \to ee$. Closed circles represent data, open circles simulation [52].

3.3.2 Identification

The selection of prompt electrons in the central region of the detector, for $|\eta| < 2.47$, relies on a likelihood based identification. The signal corresponds to the prompt electrons while the background consists in a combination of jets mimicking the prompt electrons, electrons produced from photon conversion and non prompt electrons from heavy flavour containing hadrons. The corresponding likelihoods are defined as

$$L_{S(B)}(\mathbf{x}) = \prod_{i=1}^{n} P_{S(B),i}(x_i) \tag{3.1}$$

with **x** n-component input vector, $P_{S,i}(x_i)$ is the signal pdf for the i-th quantity at value x_i and $P_{B,i}(x_i)$ is the corresponding value for the background pdf. From them, a *discriminant* d_L is formed

$$d_L = \frac{L_S}{L_S + L_B} \tag{3.2}$$

for each electrons candidate. The identification is based on this discriminant, which presents a sharp peak at unity (zero) for the signal (background). In order to obtain the pdfs, Monte Carlo (MC) simulations of the $Z \to ee$ and $J/\Psi \to ee$ processes are considered, producing finely binned histograms of the individual identification quantities.

Four *operating points* are defined using the discriminant: *VeryLoose*, *Loose*, *Medium* and *Tight*. They correspond to distinct efficiencies for prompt electron identification, as it can be seen from figure 3.4 as a function of the electron transverse energy E_t and η for the three working points Loose, Medium and Tight. The *Tight* requirement was applied in the analysis, in order to select a high purity electron sample. Moreover, electrons are required to be in $|\eta|$ <1.37 or 1.52< $|\eta|$ <2.47, with a p_{T} >15 GeV.

3.3.3 Isolation

The implementation of isolation criteria is dependent on the particular analysis needs, and represents a compromise between highly efficient prompt electrons identification and good rejection capacity of non prompt ones as well as misidentified light hadrons. It is convenient to introduce specific variables in order to quantify the amount of activity in the proximity of the candidate. The usual approach in ATLAS for the activity determination consist in summing the transverse energies of clusters in the calorimeter, or the transverse momenta of tracks inside a cone of radius $\Delta R = \sqrt{(\Delta\eta)^2 + (\Delta\phi)^2}$, without the candidate contribution. The former corresponds to the *calorimeter-based isolation*. The variable E_T^{cone}, used for the calorimeter base isolation, was initially defined from the sum of the transverse energies of the calorimeter cells within a given

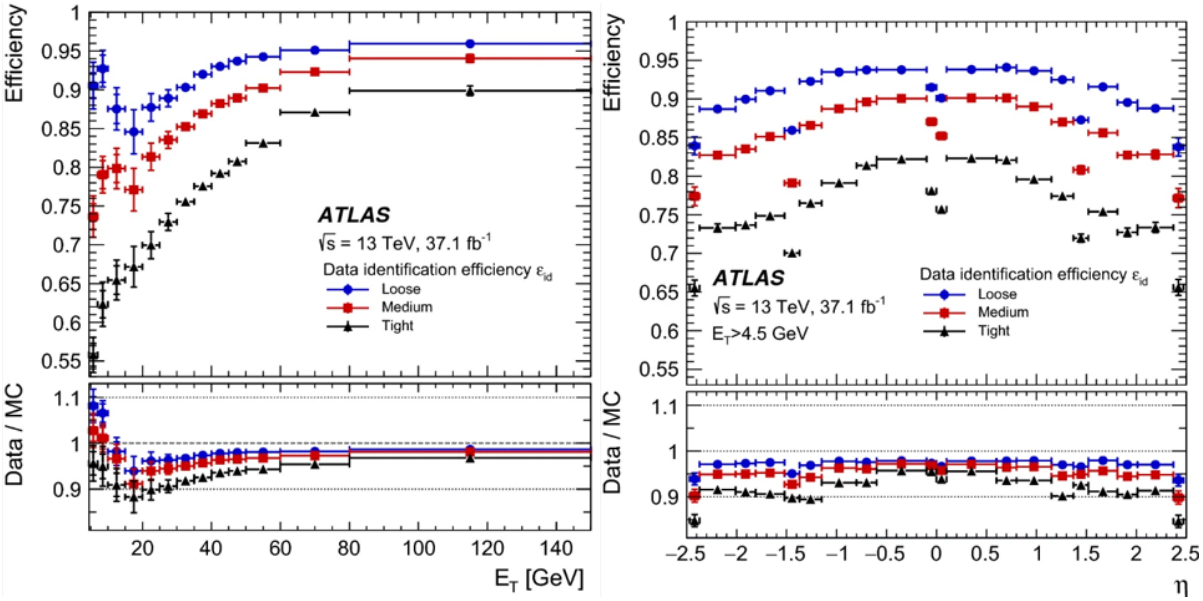

(a) (b)

Figure 3.3: Left: Electron identification efficiency in $Z \rightarrow ee$ events, as a function of E_t. Right: efficiency for the same events, as a function of η. In both cases, the Loose, Medium and Tight working points are considered. In the bottom panels, the ratio of the efficiencies measured using data and MC is shown. The total uncertainties accounts for both the statistical and systematic ones [52].

cone aligned to the electron direction. More recently, the definition is based on the transverse energies of topological clusters. Thanks to this change, an improved pile-up resistance and the data-simulation agreement have been achieved.

Track-based isolation instead considers the introduction of a variable $p_T^{varcone}$, defined as the sum of transverse momenta of all tracks contained within a cone of radius $\Delta R = \min(0.2, 10\,\text{GeV}/E_T)$, around the electron candidate track (excluding the candidate itself). The measured isolation efficiency for electron, as recorded with data available up to 2017, is presented in figure 3.4.

Electron isolation WPs definition depends on either the specific cuts applied on the isolation variables or the particular target fixed efficiency value.
The isolation procedure adopted in the analysis is instead based on the *Prompt Lepton Veto tagging* (PLVeto) [54], with p_{T} dependant requirements aiming to obtain a high purity (the so-called "Tight" WP). The PLVeto general idea is in the adoption of a Boosted Decision Tree (BDT) in order to separate prompt and Non-prompt leptons,

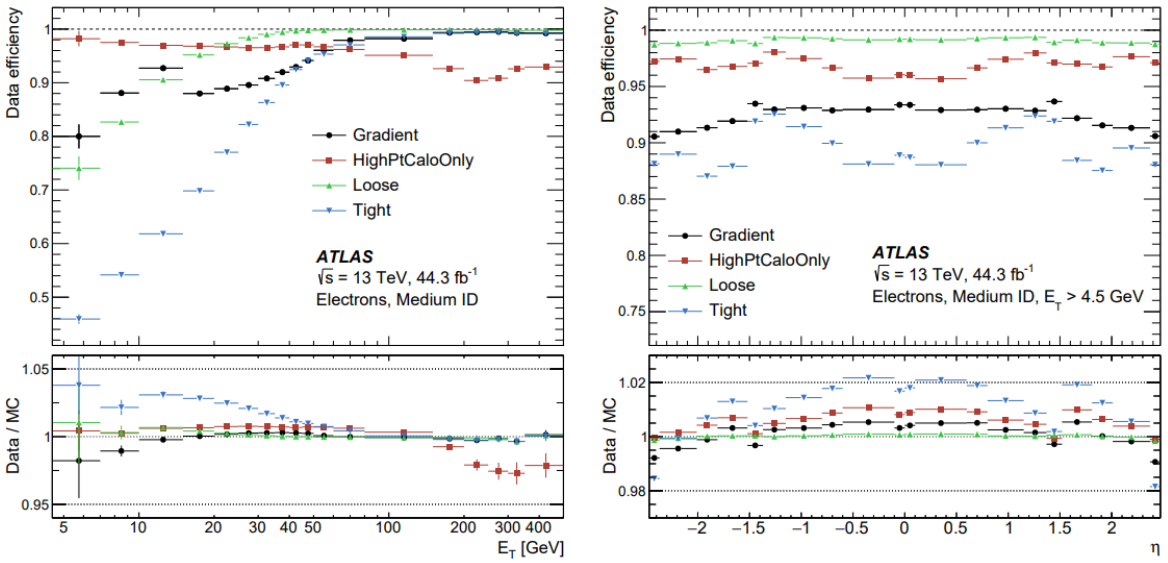

(a) (b)

Figure 3.4: Electron isolation efficiency in $Z \to ee$ events, as a function of E_t (a) and η (b), for the listed working points. In the lower panels, the ration between the measured efficiency (data) and the MC simulations is provided [53].

using as input the energy deposits and charged-particle tracks (including the lepton track) in a cone around the lepton direction, on the basis of an assigned score cut. For the values of the p_{T} of interest for the present analysis, the score cut is parameterized as :

$$p_{\mathrm{T}} < \max\left(-0.88, A + Be^{-\frac{p_{\mathrm{T}}}{c}}\right)$$

3.4 Muons

3.4.1 Reconstruction

Muon reconstruction [55, 56] is performed by making use (mostly) of the information obtained from the ID and MS. ID contribution and steps to the reconstruction are analogous to those discussed for electrons, as they are the same for every charged particle. Muon reconstruction in the MS instead starts by searching for short, straight-line segments, reconstructed from hits in an individual MS station, using a Hough transform. Segments from the different stations are then combined into preliminary track candidates, imposing as constraints the position of the IP and the assumption of a

parabolic trajectory, corresponding to a first-order approximation to the muon bending in the magnetic field. The hits in the RPC or TGC are used in order to measure the coordinate orthogonal to the bending plane. CSC segments reconstruction occurs instead via a combinatorial search in the ϕ and η detector planes. By combining these information, the three-dimensional track candidates are formed, using seeds from the middle layers, where a larger number of tracks is present, and then extending then inward and outward. The final step for muon reconstruction is a global χ^2 fit of the muon trajectory, which takes into account the effect of the particle interaction with the detector as well as misalignment effects between the detector chambers.

Four muon classes are defined in the combined reconstruction, depending on which sub-detector is considered:

1. *Combined muon* (CB): the track reconstruction is performed individually by the two subdetectors and a combined track is produced via a global refit made using the hits from the ID and MS. In this procedure, MS hits may be added or removed in order to improve the fit quality. Most of the muons are reconstructed using an outside-in pattern recognition, in which first the muons from the MS are reconstructed, and the the ID track is extrapolated inward.

2. *Segmented-tagged muons* (ST): tracks in the ID are classified as muon tracks if, once they are extrapolated to the MS, they are associated with at least one local track segment in the MDT or CSC. ST muons are used for muons crossing only one layer of the MS chamber due to either low p_T or because they are in regions of the MS with reduced acceptance.

3. *Calorimeter-tagged muons* (CT): if a track in the ID can be matched to an energy deposit in the calorimeter compatible to a minimum ionizing particle (MIP), then said track is identified as a muon. This class is characterized by the lowest purity among all the muon types, but it recovers acceptance in the parts of the ATLAS muon spectrometer which are only partially instrumented. Thus, the identification criteria for this kind of muons is optimized for $|\eta| < 0.1$ and $p_T >$5 GeV, in order to suppress the large background contamination.

4. *Extrapolated muons* (ME): This reconstruction is applied when the MS track cannot be matched to an ID track and its parameters are extrapolated from the beamline. The muon is required to traverse at least two layers of MS chambers, or three layers in the forward region. This kind of muons is mostly used in order to extend the acceptance for muon reconstruction in 2.5$< |\eta| <$2.7, which is not covered by the ID.

A summary of the muon classes introduced so far is shown in figure 3.5. When muons share the same ID track, a hierarchy preferring CB muons over the ST, which in turn

are preferred over the CT, is applied. Overlaps with ME muons are solved by analyzing the track hit content and selecting the track with largest number of hits and better fit quality.

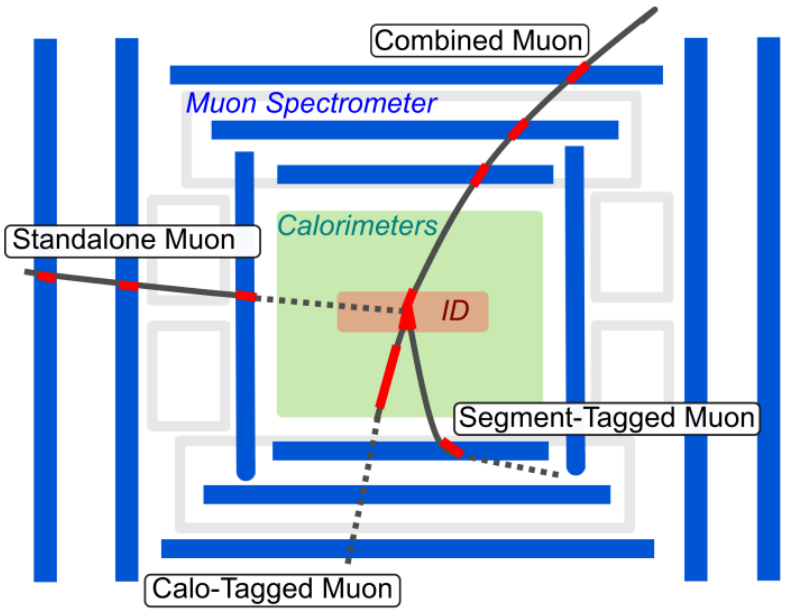

Figure 3.5: Visual summary of the muon classes introduced [57].

3.4.2 Identification

Following muon reconstruction, as for the electrons, an identification procedure is applied in order to improve the muon quality, by imposing additional requirements on the number of hits in the ID and different MS chambers. Five different muon identification selections are considered, in order to reduce the background due to non prompt muons, which are mostly originated from pion and kaon decays. Once again, we have in increasing order of purity, the *Loose*, *Medium* and *Tight* selections. Moreover, two additional WPs are introduced for the extreme phase space regions, the *High* and *Low* p_T. More in detail, we have that [56]:

> *Medium Muons* : the medium identification criteria represents the default selection for muons in the ATLAS experiment. The selection aims to minimise the systematic uncertainties associated with muon reconstruction and calibration, and involves only CB and ME tracks.
> For the ME tracks, a minimum of three hits in at least two MDT layers are required, with the exception of the $|\eta| < 0.1$ region, where at least one track in

one MDT layer is required, but with no more than one MDT hole layer. For the CB tracks instead, at least three MDT/CSC layers are required and the region considered is the $2.5 < |\eta| < 2.7$ one, which extends the acceptance outside the ID geometrical coverage.

Loose Muons: this selection is designed to maximise the reconstruction efficiency while providing good-quality muon tracks. All muon types are used and all CB and ME muons satisfying the Medium requirement are included in this selection. CT and ST muons are restricted to the $|\eta| < 0.1$ region, while in the $|\eta| < 2.5$ region, approximately 97.5% of muons are combined ones, with the remaining consisting in CT and ST muons.

Tight Muons: Tight muons are selected with the goal of maximising the purity, at the cost of some efficiency. This selection criteria involves only CB muons with hits in at least two MS stations which also satisfy the Medium selection criteria.

High p_T muons: The High p_T selection maximises the momentum resolution for tracks having transverse momentum larger than 100 GeV. CB muons which have passed the Medium selection and presenting at least three hits in three MS stations are selected. This requirement, despite reducing the reconstruction efficiency, allows for an improved p_T resolution above 1.5 TeV.

Low p_T muons: The Low p_T WP targets the lowest-p_T muons, which are not fully reconstructed in the MS and are identified via MS segments. Only CB and IO muons with at least one hit in precision MS station are considered (with the exception of the $|\eta|$ >1.3 region, where muons with $p_T > 3$ GeV reach the second station, in which case at least two hits are required). This WP provides the optimal separation between prompt and non prompt muons from hadronic decays.

Muons in the analysis are required to pass the $Medium$ reconstruction requirement, and to have $|\eta|$ <2.5 with a $p_{\mathrm{T}} > 15$ GeV.

3.4.3 Isolation

Muon isolation consists in the measurement of the detector activity around a muon candidate: muons produced following the decay of heavy particles, such as W,Z or Higgs bosons are often isolated, i.e. they show reduced to no activity around them, unlike those coming from semileptonic decays.

Usually, two schemes are considered for muon isolation: a track based isolation and a calorimeter based one.
The track based isolation method is based on the definition of an isolation variable

$p_T^{varcone30}$, which is defined as the scalar sum of the transverse momenta of tracks with p_T >1 GeV, in a cone of size $\Delta R = \min(10\text{GeV}/p_T^{\mu}, 0.3)$ around the muon of transverse momentum p_T^{μ}, excluding the muon track itself. A different isolation variable can also be adopted, by considering instead $\Delta R = 0.2$, defining a quantity labelled as p_T^{cone20}
The calorimeter based method, instead introduces a variable labelled as $E_T^{topocone20}$,which is defined as the sum of the transverse energy of topological clusters in a cone of size $\Delta R = 0.2$ around the muon, provided that the contribution from the energy deposit coming from the muon itself has been subtracted and a correction due to pile-up effects has been introduced.

Additionally, a combination of the two can also be applied, in the *particle-flow based* isolation. Particle-flow based isolation considers the the sum of track-based isolation using $p_T^{varcone30}$ for $p_T < 50$ GeV and p_T^{cone20} for $p_T > 50$ GeV, and the transverse energy of neutral particle-flow objects in a cone of size $\Delta R = 0.2$ around the muon, called $\mathrm{E}_T^{neflow20}$.

As for the electrons, a different approach was used for muons isolation, based on the PLVeto tagging, with a "Tight" requirement.

3.5 Jets

The *colour confinement* hypothesis is at the basis of the impossibility to observe free quarks. Coloured objects are always confined into a colour singlet state, so that no objects of non-zero colour charge can freely propagate. The idea is based on the gluon-gluon self interaction: qualitatively, as the two free quarks are pulled apart, the colour field gets "squeezed" into a tube between the two, so that, for constant energy density per unit length in the tube, the potential will increase with the separation, in a linear fashion, according to $V(r) \sim kr$. Eventually, the separation will lead to a potential energy sufficiently large to create a second quark-antiquark pair, breaking the original "tube" into a pair of smaller ones. The production of $q\bar{q}$ pairs will continue until the kinetic energy has converted into clusters of quarks and gluons, each of net zero color - a process known as *hadronization*.
Therefore, following an high energy collision involving final state free quarks, what is observed experimentally are collimated streams of hadrons, known as *jets*, which deposit energy inside the calorimeter. Jets are a representation of the underlying physical process and their reconstruction, as performed by the ATLAS collaboration, is based on an anti-k_t [58] algorithm.

First, the distances d_{ij} and d_{iB} are defined, respectively as the distance between objects

i and j and the distance between the object i and the beam, according to the formulas

$$d_{ij} = min(k_{ti}^{2p}, k_{tj}^{2p})\frac{\Delta_{ij}^2}{R^2} \tag{3.3}$$

$$d_{iB} = k_{ti}^{2p} \tag{3.4}$$

where $\Delta_{ij}^2 = (y_i - y_j)^2 + (\phi_i - \phi_j)^2$, ϕ_i, y_i and k_{ti} are the azimuthal angle, the rapidity and the transverse momentum of particle i, R is the radius parameter and p is a parameter related to the relative power of the energy versus the geometrical scale represented by Δ_{ij}. For $p = -1$, we have an anti-k$_t$ algorithm, which identifies the smallest distance between particles/towers and merge the pair into a proto-jet. This is an iterative procedure that proceeds until $d_{ij} > d_{Bi}$. Two possible values of the parameter R can be considered: for small-R jets, typically representing quarks and gluons, $R = 0.4$, while for jets representing hadronically decaying massive particles, large jets of $R = 1.0$ are considered. The larger radius is now useful in order to capture all the decay products as being part of a single jet. In the analysis, it was choosen $R = 0.4$

Jet reconstruction uses primarily topo-clusters, topologically grouped clusters of calorimeter cells, as inputs. They are formed from seed cell, containing more than 4σ of energy, where σ represents the average amount of noise expected in said cell, defined as the sum of the expected electronic and pile-up noise. In the analysis, jet reconstruction has been performed using a particle flow (PFlow) [59] algorithm, combining measurements from the tracker and the calorimeter in order to form the input signals for the jet reconstruction.

The presence of secondary particles produced due to pile-up needs to be accounted, as they can overlap with objects of interest. To this purpose, additional calibration corrections are generally introduced, via the subtraction of the average energy due to pile-up , guaranteeing precise jet energy measurements. In particular, the average offset correction considered, $\mathcal{O}^{jet}$, is obtained from *in-situ* studies or MC simulations. The corrected momentum is then given by [60]:

$$p_T^{corr} = p_T^{jet} - \langle \mathcal{O}^{jet}(\langle \mu \rangle, N_{PV}, \eta) \rangle \tag{3.5}$$

where the correction depends on the average pile-up, as well as from the jet pseudo-rapidity and the number of reconstructed primary vertices (N$_{PV}$). In order to identify jets coming from pile-up, the ATLAS experiment has developed a dedicated algorithm, applied in Run 2, known as the *Jet Vertex Tagger* (JVT) algorithm [61]. The JVT algorithm consists in the the definition of a discriminant based on a two-dimensional likelihood, combining the information from several track-based variables. The criterion is only applied to jets with p_{T} <60 GeV and $|\eta| < 2.4$.

Jet energy scale and resolution

The Jet Energy Scale (JES) calibration aim to restore the jet energy to the particle level value [62]. In the first stage of the JES calibration chain, the pile-up subtraction discussed previously is applied. Then, a correction factor depending on p_T and $|\eta|$, obtained via MC simulations, is applied in order to improve the calibration. As a final step, an *in-situ* measurement is used in order to close the gap between Data and MC. Togheter with the JES, a precise knowledge of the Jet Energy Resolution (JER) is important for analysis involving SM jet production. Moreover, the JER also affects the missing transverse energy, which will be introduced in the following. The dependence of the JER on the transverse momentum can be parameterized using the functional form adopted for calorimeter-based resolutions, according to :

$$\frac{\sigma(p_T)}{p_T} = \frac{N}{p_T} \oplus \frac{S}{\sqrt{p_T}} \oplus C \tag{3.6}$$

N represents the noise term, S the stochastic and C the constant one. The sum is once again considered to be in quadrature. The noise term is due to electronic noise from the front-end electronics and due to pile-up. The contribution from this term is expected to be significant in the low p_T region (<30 GeV). The stochastic term takes into account statistical fluctuations in the energy deposition, and represents the limiting term in the resolution up to hundreds of GeV in jet p_T. Lastly, the constant term accounts for fluctuations in the starting points of the hadron showers, non uniform response of the calorimeter and energy deposition in the passive material of the calorimeter. This term becomes dominant in the high p_T region, i.e. above 400 GeV.

3.5.1 *b*-tagging

The identification of jets containing b-hadrons, (the so-called b-jets) is of great importance for many physics programs of the ATLAS experiment. The algorithms which allow the b-jets identification go under the name of *b-tagging algorithms* [63]. This algorithms exploit the long lifetime, high mass and high decay multiplicity of the b-hadrons, as well as the properties of the b-quark fragmentation. In particular, given the aforementioned lifetime of b-hadrons, this particles are characterized by a relatively large mean flight length, leading to at least one vertex displacement from the hard scatter collision point.

Different algorithms are used for b-jet identification. They are divided into two categories. First there are low level algorithms, reconstructing the characteristic features of the b-jets using the individual properties of the charged particle tracks associated to a hadronic jet or combining the tracks to explicitly reconstructing the displaced vertices. Secondly, the result provided by low level algorithms get combined by high

level ones, in order to maximise the performances.

The specific algorithm applied in the analysis is known as DL1r [64], based on a Deep Neural Network (DNN). The DL1r output is multidimensional, corresponding to the probabilities for a jet to be a b-, c- or light-flavoured jet. The algorithm considers all flavours as equally likely in the training phase, allowing, in principle, to be applied also for c- tagging. The $b-$ tagging discriminant expression is given by:

$$D_{DL1r} = ln\left(\frac{p_b}{f_c \cdot p_c + (1 - f_c) \cdot p_{light}}\right)$$

where p_b, p_c, p_{light} and f_c are respectively the $b-$jets, $c-$jets and light flavour jet probabilities and the effective $c-$jet fraction, in the background hypothesis [65]. $b-$tagging working points (WPs) are defined on the basis of the $b-$tagging efficiency. In particular, a 70% WP was considered in the analysis.

3.6 Overlap Removal

Overlap removal is a procedure applied in order to avoid the reconstruction of the same detector signal as multiple analysis objects. The procedure itself is composed by several steps: first of all, calorimeter-tagged muons which share a track with an electron are removed. Consequently, any remaining electron sharing a track with other muons is removed.
As a second step, the closest jet to each electron, within a $y - \phi$ cone of opening $\Delta R < 0.2$, is removed. This aims to reduce the number of electrons misreconstructed as jets. Moreover,in order to reduce the background contribution from non-prompt, non-isolated electrons from heavy flavour hadron decay, electrons within a $\Delta R < 0.4$ cone are removed.
The following step consists in the removal of jets with less than three tracks, located within a distance $\Delta R < 0.2$ from a muon. This enables a reduction of jet fakes, connected to calorimeter deposits associated to muons.
Lastly, in order to reduce the contamination of non prompt muons from heavy flavour hadron decays, muons within a distance of $\Delta R < 0.4$ to any surviving jets are removed.

Chapter 4

Data, Monte Carlo samples and Selections

The present chapter provides an overview on several preliminary aspects considered in the analysis. First, the Data and Monte Carlo samples used are introduced. For the latter, a description of how the signal and background contributions have been simulated is provided, in section 4.1. Next, the Event Selection criteria and Particle Level definition of the objects of interest are discussed, in sections 4.2 and 4.3. Lastly, the obtained Control Plots are presented, for a comparison between data and simulated events, in 4.3.1.

4.1 Data and Monte Carlo samples

4.1.1 Data Sample

The analysis made use of the full ATLAS dataset collected during Run-2 operations (2015-2018). The dataset consists in events corresponding to proton-proton collision at

a centre-of-mass energy of 13 TeV, with a total integrated luminosity of 139 fb^{-1}. Moreover, the dataset includes only data obtained during stable beam LHC operations and with the ATLAS detector fully functioning. For each year of operation considered, the partial integrated luminosities are shown in table 4.1. The quoted luminosities correspond to events included in the so-called *Good Run List*, i.e. runs which are considered well suited for physics analysis.

Table 4.1: Integrated luminosities per each year of operation considered

Year	Int. Lumi. (pb^{-1})
2015	3219.56
2016	32 988.1
2017	44 307.4
2018	58 450.1

4.1.2 Monte Carlo simulated samples

Theoretical predictions used in the analysis are based on the available Monte Carlo (MC) simulations of the processes of interest. Event generation in High Energy Physics encompasses several different steps, starting from the *matrix element* (ME) calculation of the hard process, at a fixed perturbative order.
To simulate the additional final state radiation beyond the one predicted at the fixed order, *Parton Shower* (PS) algorithms are employed. These algorithms allow to account for soft and collinear radiation which would otherwise provide a divergent contribution. The simultaneous use of ME and PS poses in principle a problem of double counting of some corrections, introduced by both methods, which need to be subctracted. This is performed when the ME and PS generator are interfaced, in the so-called *matching* step. Moreover, in order to account for the effect of confinement, phenomenological hadronization models are later applied in order to simulate final state stable particles. Usually, the three steps (ME, PS and hadronization) are not simulated using a single generator, but instead require to interface several generators. Lastly, it is necessary to simulate the detector response to the generated event, which is done using the software Geant 4 [66].

Monte Carlo (MC) samples from the mc16 simulation campaign were used. This campaign is further divided into three different sub-campaigns, labelled with a letter (a,d,e), corresponding to different data-taking periods. In particular, the mc16a simulates the experimental conditions of the 2015 and 2016 periods, the mc16d the conditions of the 2017 period and lastly the mc16e the conditions of 2018. Simulation

samples are re-weighted, depending on the period under consideration, in order to match the data pile-up profile. As signal, the sum of the $t\bar{t}$ and tW samples is considered, from the same combination of generators and parton showers.

In the following, the used samples for signal and background are introduced.

Nominal signal sample

$t\bar{t}$ **production** : Nominal $t\bar{t}$ events production is modelled using the PowhegBox v2 [67–70] generator, which provides matrix elements at next-to-leading order (NLO) in the strong coupling constant α_s, using the NNPDF3.0NLO [71] parton distribution function and the h_{damp} parameter. This parameter defines the separation between the radiative phase space in the region described by the parton shower and the hard region, described by the matrix element. Therefore, it controls the PS/ME matching in Powheg. It is set to 1.5 m_{top}.

The functional form of the renormalisation and factorisation scale is set to the default scale $\sqrt{p_T^2 + m_{top}^2}$. The events are interfaced with Pythia 8.230 for the parton shower and hadronization, using the A14 set of tuned parameters [72] and the NNPDF2.3lo set of PDFs [73]. Bottom and Charm hadrons decays are simulated using the EvtGen v1.6.0 program [74].

This sample is normalised to the cross-section prediction at next-to-next-to-leading order (NNLO) in QCD, with resummation at next-to-next-to-leading logarithmic (NNLL) soft-gluon term. The calculations are performed using the `Top++2.0` [75] program, and the corresponding uncertanties on the PDF and α_s are evaluated according to the PDF4LHC prescription [76].

tW production: The nominal associated tW production is modelled using the PowhegBox v2 [77] generator, providing matrix elements at NLO in α_s, in the *five flavours scheme* 5FS, with the parton distribution function NNPDF3.0NLO set. The functional form of the factorisation and renormalisation scale is set to the default one, which is equal to $H_T/2$, where H_T is the scalar sum of final outgoing partons. The *diagram removal* (DR) scheme (cfr section 1.3) is used in order to account for the interference with the $t\bar{t}$ prodution. Events are interfaced with Pythia8.230, using the A14 tune and the NNPDF23LO PDF set. Bottom and Charm hadrons decays are simulated using the EvtGen v1.6.0 program.

The cross section is corrected to the theory prediction calculated at NLO in QCD and with NNLL soft gluon corrections [78].

Alternative signal samples

Additional signal samples are considered for comparison:

tW **PWG+PY8 (DS)**: similar to the nominal PWG+PY8 sample, but considers the DS scheme;

tW **PWG+PY8 with fixed scales**: the nominal samples is produced by employing dynamical scales (dyn, in the following) [79]. Alternative samples have been considered for both schemes (DS and DR), using instead fixed scales set to a default value equal to the top quark mass, m_t =172.5 GeV;

$t\bar{t}$ **and** tW **PWG+PY8 (DR,** $h_{damp} = 3m_t$**)**: same setting as the nominal PWG+PY8 sample, but the h_{damp} parameter is set to $3m_t$;

$t\bar{t}$ **and** tW **(DR) PWG+H7**: event generation is done using the same PowhegBox v2 set-up, interface with Herwig 7.7.1.3 [80, 81]. The sample was generated using a different MC tuning with respect to the nominal ones, the H7.1-Default tune [82] and a different PDF set, the MMHT2014LO set [83];

$t\bar{t}$ **PWG+PY8+Madspin**: similar to the nominal sample for $t\bar{t}$, but using MadSpin [84] for top quark decay;

$t\bar{t}$ **and** tW **(DR) PWG+PPY8 (pthard1)** : similar to the nominal sample, but using a pthard parameter set to 1 instead of pthard $= 0$. The pthard parameter is a Powheg internal parameter regulating the matching between Powheg and Pythia, by defining the vetoed phase space regions of the showering, where Powheg and Pythia would overlap. The specific value of this parameter defines the strategy applied by the simulator for the definition of the vetoed regions ;

One last sample has been considered as an alternative to the nominal ones and does not provide the signal as the sum of $t\bar{t}$ and tW: the *bb4l* [85] one. The process is modelled using a generator which is a generalization of Powheg, producing final states $l^+l^-\nu_l\overline{\nu}_l b\bar{b}$ by taking into account not only the singly- and doubly- resonant contributions and their quantum interference, but also the off-shell and non resonant effects [85]. For this sample, the events available are simulated up to the NLO in the strong coupling constant, and the functional form considered for the renormalisation and factorisation scale is set to $[(m_t^2 + p_{T,t}^2)(m_{\bar{t}}^2 + p_{T,\bar{t}}^2)]^{\frac{1}{4}}$. For diagrams containing intermediate Z bosons instead, the scales are set to $\frac{\sqrt{p_Z^2}}{2}$, with $p_Z = p_{l^+} + p_{l^-} + p_\nu + p_{\overline{\nu}}$. The h_{damp} parameter is set top 1.5 m_t. Events are interfaced with Pythia 8.245 using the A14 tune and the NNPDF2.3LO PDF set.

Background samples

$t\bar{t}V$ **production**: It correspond to events in which $t\bar{t}$ pair production occurs in association with a Vector Boson V (W,Z). Its modelling is done using the MadGraph5_aMC@NLO v2.3.3 generator, providing matrix elements at NLO in α_s with the NNPDF3.0nlo PDF. The functional form of the renormalisation and normalisation scales is set to $0.5 \times \sum_i \sqrt{m_i^2 + p_{T,i}^2}$, with the index i running over all the particles generated in the matrix element calculation step. Top quark decay is modelled at LO using MadSpin [84], which allows to preserve spin correlation. The events are interface with Pythia8 8.210 for the parton shower and hadronization, using again the A14 set of tuned parameters and the NNPDF2.3lo PDF. Botton and charm hadrons decays are simulated via EvtGen v.1.2.0. The cross section calculation is perfomed at NLO QCD and EW accuracy, using MadGraph5_aMC@NLO.

Z+jets production: It is simulated using the Sherpa v2.1.1 generator [86]. Matrix elements are matched and merged with the Sherpa PS, using the ME+PS@NLO [87] prescription. The virtual QCD corrections on the matrix element at NLO are obtained using the OpenLoops library [88]. The NNPDF3.0NLO PDF set is used in order to generate the samples.

Diboson production: Diboson production was simulated using the Sherpa v2.2.2 and v2.2.1 generator depending on the process. The samples were generated using ME at NLO in QCD for up to one additional parton and at LO for up to three additional parton emissions. Samples for the $gg \to VV$ processes were generated at LO, for up to one additional parton emission. The multiple matrix elements are matched and merged with the Sherpa parton shower. Virtual QCD corrections are introduced via the OpenLoops library and the NNPDF3.0NNLO set was used, together with the dedicated set of tuned paramters available in Sherpa for the parton shower.

Non-prompt production: It consists in events associated with the production of non-prompt leptons. As such, it is estimated via MC simulations using truth level information from $tW, t\bar{t}$, as well as from the background sources. It assumes all fakes come from modelled process.

The total number of expected and observed events is presented in table 4.2

4.2 Particle-Level objects definition

The differential cross section measurement has been performed at *particle level*. The particle level description of physical objects concerns them before their interaction

Sample	$e\mu$, $N_{jets} \geq 2$, $N_{bjets^{70}} \geq 2$
$t\bar{t}$	212000 ± 15000
tW (DR)	6600 ± 500
$t\bar{t}V$	550 ± 70
Diboson	36.0 ± 3.5
Z+jets	50^{+20}_{-19}
Fakes	1400 ± 700
Expected	220000^{+15000}_{-16000}
Observed	219230

Table 4.2: Observed and expected number of events in the channel after the full event selection. The uncertainties include the Monte Carlo statistic uncertainties and all systematic uncertainties except for the signal modelling ones. All the systematic uncertainties are discussed in section 5.4.

with the detector. The particle level encompasses all stable particles from the event generator, which are those satisfying the condition $c\tau > 10$ mm, for τ particle's average lifetime.

In the analysis, particle level electrons and muons from the signal samples were required to not have been originated from hadrons, nor directly or indirectly following an intermediate τ lepton decay. p_T and η requirements for their particle level definition is the same as for the detector level, introduced when discussed object reconstruction. Baseline leptons definition is done by imposing a looser p_{T} requirement of 4 GeV and 5 GeV respectively for muons and electrons.

Particle-level jets are reconstructed by clustering thruth particles, with the anti-k_{T} algorithm introduced in the previous chapter, with an radius $R = 0.4$. Baseline jets are required to have $p_{\mathrm{T}} > 20$ GeV and $|\eta| < 2.8$. Signal jets must satisfy the conditions $p_{\mathrm{T}} > 25$ GeV and $|\eta| < 2.5$.
B-hadrons are matched to jets using a ghost association-procedure [89]. This is performed by clustering truth level jets according to the usual methods, but setting all B-hadrons energies at negligible value. In this way, all jets containing a B-hadron are b-tagged.

The overlap removal of particle-level objects takes place according to different requirements with respect to the detector level case. In particular, muons and electrons are excluded if within $\Delta R < 0.4$. No μ-e overlap removal is applied at particle level.

Leptons resulting from a W decay chain involving only other leptons are accepted

at particle level: a direct lepton-W match is not required. This means that leptons resulting from the decay of an intermediate τ, if coming directly from a W, are accepted.

4.2.1 Particle-level selection

The fiducial region defined, using particle level objects, in order to replicate the detector-level selections discussed in the following, is:

- one electron and one muon with $p_{\mathrm{T}} > 28$ GeV;
- at least two jets, with $p_{\mathrm{T}} > 25$ GeV;
- at least two $b - jets$;

4.3 Event selection

The measurement of the $WbWb$ production differential cross section, in the dilepton channel, following the process

$$pp \rightarrow WbWb \rightarrow l^{+}l^{-}\nu_{l}\overline{\nu_{l}}b\bar{b} + X$$

has been performed as a function of some basic kinematic variables, corresponding to the leptons transverse momentum, the final state jets transverse momentum, the leptons invariant mass and the number of extra-jets. In particular, a separation between leading and sub-leading transverse momenta (respectively the highest and second highest p_T) was considered for the objects under study. Thus, for the variables considered in the following, the notation $p_{\mathrm{T}}^{\mathrm{lep},1}$, $p_{\mathrm{T}}^{\mathrm{lep},2}$, $p_{\mathrm{T}}^{\mathrm{jet},1}$, $p_{\mathrm{T}}^{\mathrm{jet},2}$, $m_{\mathrm{l_1 l_2}}$, $N_{\mathrm{extrajets}}$ is introduced, with the apexes 1 and 2 referring respectively to the leading and subleading object.

The requirements imposed in order to define the $WbWb$ signal process were:

- The presence of opposite sign (OS) charge final state leptons, corresponding to an electron and one muon, with $\mathrm{p_T} > 28$ GeV;
- At least two jets, with $\mathrm{p_T} > 25$ GeV;
- At least two $b-$jets at 70% WP;
- The invariant mass $m_{ll} > 15$ GeV;

The choice of OS final state leptons allows to strongly suppress the $Z \rightarrow ll$ background.

4.3.1 Control Plots

Control Plots provide a way to verify how data are distributed with respect to the processes considered in MC simulations. More precisely, they consist of a comparison of the reco-level distribution observed from data and the one predicted on the basis of MC simulations. In the following, the histograms corresponding to each of the variables considered in the analysis are presented, as shown in figures 4.1 and 4.2 . The plots are produced considering events passing the selection criteria provided at the start of the section. For each of the plots shown, the black dots represent the actual data measured, while the total prediction breakdown into the individual processes is shown in the legend on the top right. The individual contributions are stacked on top of each other.

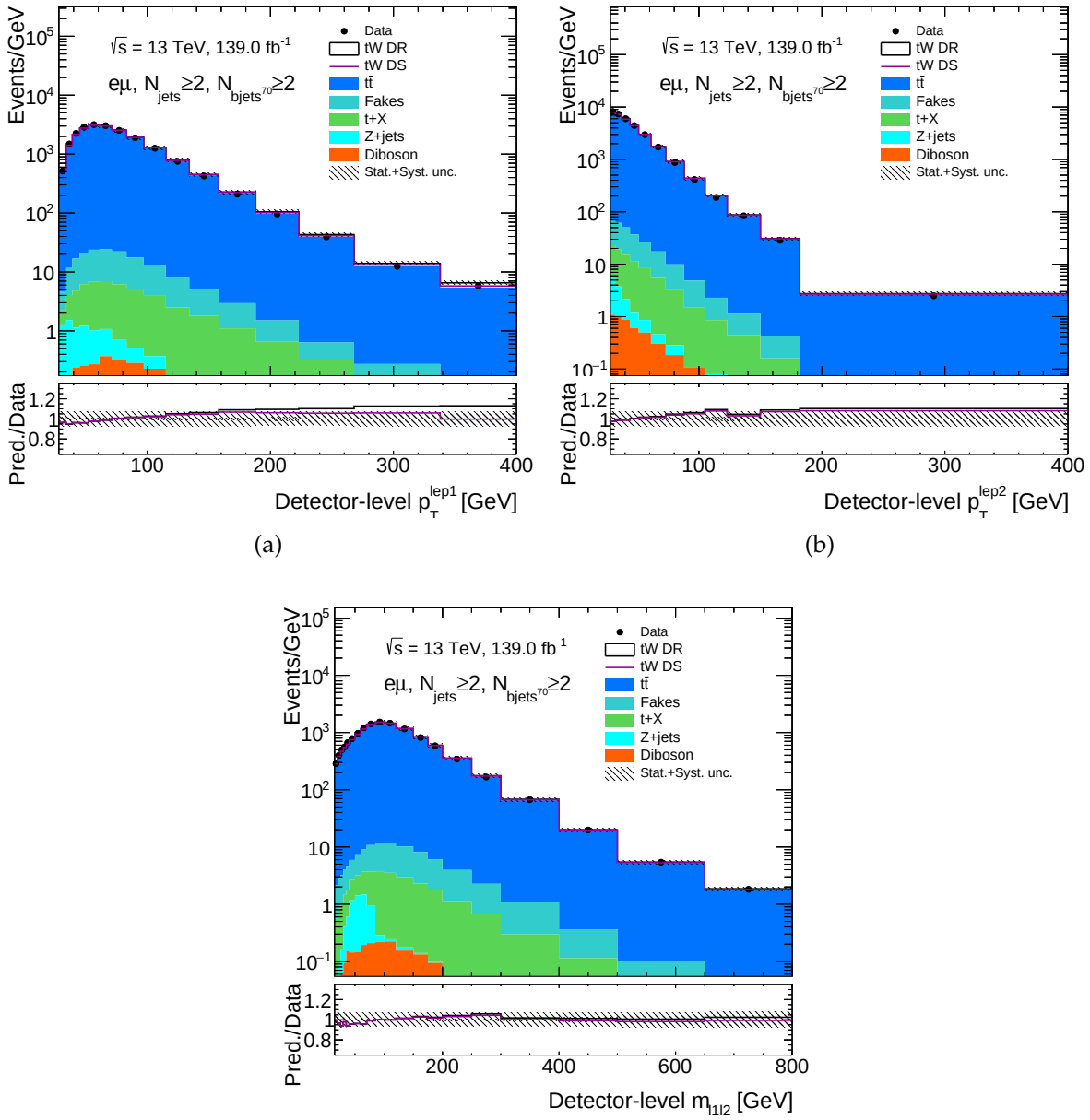

(a) (b)

(c)

Figure 4.1: Comparison between data and MC predictions for the leading (a), subleading (b) lepton transverse momentum and invariant mass (c), respectively. The individual contributions are listed on the top right of each plot. The contribution labelled as Fakes includes both the contribution from fake (misidentified) and non prompt leptons. In the bottom panel, the ratio between Predictions and Data is provided, for the two tW schemes, as a function of the corresponding variable. The hatched area corresponds to the combined statistical and systematic uncertainties.

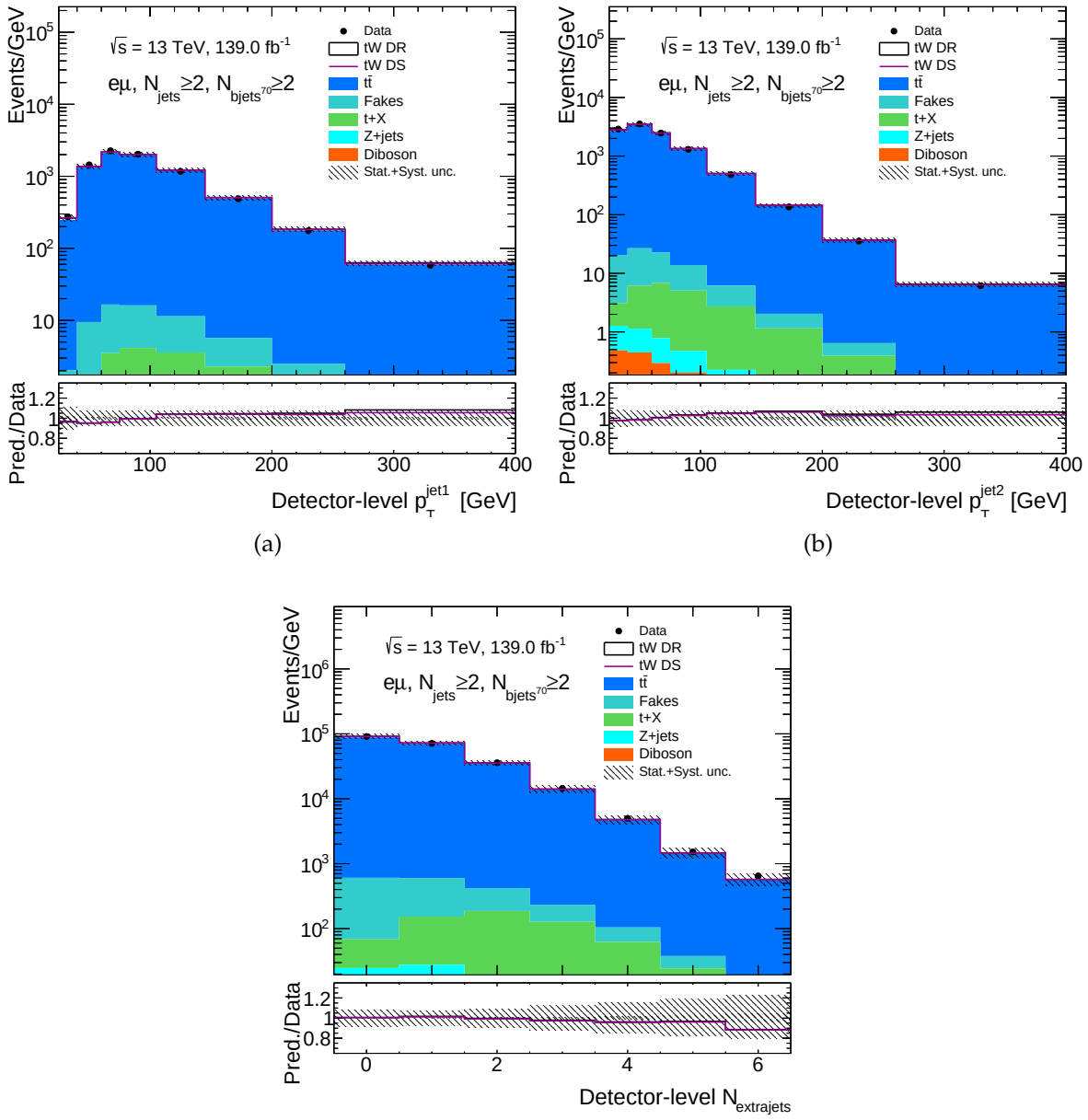

(a) (b)

(c)

Figure 4.2: Comparison between data and MC predictions for the leading (a) and subleading (b) jet transverse momentum, and number of extra jet (c) respectively. The individual contributions are listed on the top right of each plot. The contribution labelled as Fakes includes both the contribution from fake (misidentified) and non prompt leptons. In the bottom panel, the ratio between Predictions and Data is provided, for the two tW schemes, as a function of the corresponding variable. The hatched area corresponds to the combined statistical and systematic uncertainties.

Chapter 5

Analysis Strategy

In this final chapter, the analysis strategy is discussed. First, the unfolding procedure applied for the measurement of the differential cross-section is introduced from a theoretical point of view, in section 5.1. Binning studies and the validation of the unfolding procedure are described in sections 5.2 and 5.3 respectively. For the former, in particular, the results obtained in the validation step are presented. Next, the uncertainties considered in the analysis are introduced, in section 5.4, together with summary plots for each of the variables under consideration. The method applied for the calculation of the χ^2 is thus introduced in section 5.5. Lastly, the complete discussion of the results obtained is provided, in section 5.6.

5.1 Unfolding

The procedure of estimating a probability distribution when no parametric form is available, and data are subject to additional random fluctuations due to the limited resolution, limited geometric acceptance of the detector and reconstruction efficiency effects is known as *Unfolding*[1] [90, 91]. Unfolding is necessary whenever one desires to compare a measurement with the results of other experiments as well as to theoretical predictions of the *true* distribution, as it allows to correct the distortions related to the particular experimental conditions in which the measurement is performed.

The problem can be formalized as follows: consider the case in which one wants to determine the *probability density function* (pdf) $f(y)$ of a random variable y. Due to the distortions introduced by the detector, in each observation the *true* value of y will be different from *measured* one, x, which will be distributed according to another pdf $g(x)$. The two pdfs are related by a *convolution*

$$g(x) = \int R(x|y) f(y) dy \tag{5.1}$$

where $R(x|y)$ is the so-called *Response function*. Under our assumption of no available parametric form, it is convenient to represent the pdfs of both y and x as histograms. Introducing the vectors $\boldsymbol{\mu} = (\mu_1,...,\mu_M)$ (the *true histogram* or *true spectrum*) and $\boldsymbol{\nu} = (\nu_1,...,\nu_N)$ (the *reconstructed spectrum*), corresponding to the expectation values for the histogram y and the expected number of events in bins of x, respectively, we can write (5.1) as:

$$\nu_i = \sum_{j=1}^{M} R_{ij}\mu_j, \qquad i = 1, ..., N \tag{5.2}$$

R_{ij} is known as the *Response Matrix* and can be interpreted as the conditional probability

$$R_{ij} = P(\text{observed in bin } i \mid \text{true value in bin } j) \tag{5.3}$$

Therefore, the goal of the unfolding is to provide an estimate of the true distribution, which is *folded* via the response function. Summing the response matrix over all possible bins of the observed variable, one can define the *efficiency* over the bin j, ϵ_j :

$$\epsilon_j = P(\text{observed anywhere} \mid \text{true value in bin } j) = \sum_{i=1}^{N} R_{ij} \tag{5.4}$$

[1] the same procedure is also known as *Deconvolution* or *Unsmearing*

Generally speaking, the response matrix is not diagonal. The effect of the off-diagonal elements of the matrix is the *bin migration* of events: an event generated in a bin j can be reconstructed in a bin i≠j. To highlight this bin migration phenomenon, it is possible to define the *Migration Matrix*:

$$M_{ij} = \frac{1}{\epsilon_j} R_{ij} \tag{5.5}$$

The elements in the columns of the migration matrix are normalized to unity. In this way, provided that the effect of acceptance has been accounted for, the probability to reconstruct an event in *any* bin is equal to 1 [92]. Equation (5.2) does not account for the presence of *background* events in bin i. In order to include them, the expected number of background events $\boldsymbol{\beta}$ must be added, obtaining the final expression (using matrix formalism):

$$\boldsymbol{\nu} = R\boldsymbol{\mu} + \boldsymbol{\beta} \tag{5.6}$$

In conclusion, the procedure aims to provide estimators $\hat{\boldsymbol{\mu}}$ for the true histogram (or, equivalently, estimators $\hat{\boldsymbol{p}}$ for the probabilities).

The most straightforward approach consists in the direct inversion of the response matrix R.[2] Assuming for simplicity the case where the number of bins in the true and observed histogram is the same (N=M), we would have:

$$\boldsymbol{\mu} = R^{-1}(\boldsymbol{\nu} - \boldsymbol{\beta}) \tag{5.7}$$

An obvious choice for the estimators of $\boldsymbol{\nu}$ is given by the corresponding data values, i.e. $\hat{\boldsymbol{\nu}} = \boldsymbol{n}$ [91].[3] This way, we could simply consider as estimators for the true spectrum:

$$\hat{\boldsymbol{\mu}} = R^{-1}(\boldsymbol{n} - \boldsymbol{\beta}) \tag{5.8}$$

This procedure, however, may present a critical issue: if the off-diagonal terms of the response matrix are too large, i.e. if the bin size is too small compared to the measurement resolution, the estimators are characterized by extremely large variances and strong negative correlations between neighbouring bins [90]. Despite the large variance drawback, the matrix inversion method provides a zero bias and minimum variance estimator [91]. To deal with this issue, it is necessary to introduce a *small bias* (systematic error) in exchange for a large variance reduction (statistical error).

[2] Generally possible in practice [90]

[3] It can be shown that this is the solution obtained from maximizing the log-likelihood, assuming the distribution to be, for instance, Poissonian or Binomial [91]

Such trade-off is implemented via the *Unfolding Regularization*. The idea is to consider a region of the $\boldsymbol{\mu}-$space around the maximal likelihood solution, where the log-likelihood is within a well defined $\Delta \ln L$ of its maximum, according to

$$\ln L(\boldsymbol{\mu}) \geq \ln L_{max} - \Delta \ln L \tag{5.9}$$

and construct the estimators by selecting the *smoothest* solution in this region, by previously defining an appropriate criterion for its definition. It can be shown that this approach is equivalent to maximizing the quantity

$$\Phi(\boldsymbol{\mu}) = \alpha \ln L(\boldsymbol{\mu}) + S(\boldsymbol{\mu}) \tag{5.10}$$

S($\boldsymbol{\mu}$) is known as the *regularization function*, representing the smoothness of the distribution. On the other hand, α is the *regularization parameter*, which can be chosen in order to obtain a particular $\Delta \ln L$. It determines the relative weight placed on the data, compared to the degree of smoothness of the solution (S). For instance, setting α =0 would provide maximally smooth estimators, which would not depend at all on the data, having thus zero variance and a clear bias. A very large regularization parameter instead recover the situation of ML solutions with zero bias and very large variances [90].

Several different approaches could be used, in principle, to carry out the unfolding procedure described, with the choice being motivated by the particular analysis ongoing. The method applied in this analysis is the *Iterative Bayesian Unfolding* [93], which, as the name suggests, is based on the application of Bayes' theorem, stated in terms of *independent causes* C_i, defined as the n_i events in the truth bin i, and produced effects, E_j, which instead can be considered as the n_j events reconstructed in bin j .

From the mere measurement of an effect, it is impossible to determine the corresponding cause in an unambiguous way. This is taken into account by introducing the probability, for a given effect, to be associated to a specific cause, i.e. $P(E_j|C_i)$, which has to be *estimated*, assuming some information on the migration matrix, and the measurement efficiency and resolution, calculated from a Monte Carlo simulations. Applying Bayes' theorem, we have that the probability of a cause, given an effect, is given by:

$$P(C_i|E_j) = \frac{P(E_j|C_i) \cdot P_0(C_i)}{\sum_{l=1}^{n_C} P(E_j|C_l) \cdot P_0(C_l)} \tag{5.11}$$

having introduced $P_0(C_i)$, the *prior* of the i-th cause. The expected number of events in the i-th bin of the cause, is given instead by:

$$\hat{n}(C_i) = \frac{1}{\epsilon_i} \sum_{j=1}^{n_E} P(C_i|E_j) n(E_j) \tag{5.12}$$

where n(E_j) is the number of effects in the j-th bin, ϵ_i the selection efficiency of the corresponding bin.

Introducing the *unfold matrix* $\mathcal{M}_{ij}^{-1}$, defined as[4]:

$$\mathcal{M}_{ij}^{-1} = \frac{P(E_j|C_i) \cdot P_0(C_i)}{\sum_{l=1}^{n_E} P(E_l|C_i) \sum_{l=1}^{n_c} P(E_j|C_l) \cdot P_0(C_l)} \tag{5.13}$$

We can write the population in the cause bins in the form:

$$\hat{n}(C_i) = \sum_{j=1}^{n_E} \mathcal{M}_{ij}^{-1} n(E_j) \tag{5.14}$$

Lastly, it is possible to provide an estimate of the posterior probability according to:

$$\hat{P}(C_i) \equiv \frac{\hat{n}(C_i)}{\sum_j \hat{n}(C_j)} \tag{5.15}$$

The method, as we have anticipated, is applied in an *iterative* fashion: the starting step consists in choosing P_0 from the best knowledge [5] of the process under study, evaluating from this the expected number of events $n_0(C_i)$. Once this initial step is cleared and the corresponding $\hat{n}(C)$ and $\hat{P}(C)$ for all causes are estimated, it is possible to replace the values of $P_0(C)$ and $n_0(C)$ with said estimate and repeat the process. The iterations will stop when, from the comparison of the χ^2 between the current and previous iteration, the difference will turn out to be "small enough" to make further iterations not convenient.

In this particular method, the problem of solutions' large variances is addressed by interrupting the maximum likelihood procedure before it converges to its true maximum. Thus, the number of iterations acts in a sense as the regularization parameter. Concerning the actual implementation of the unfolding method described so far, the analysis exploited the `RooUnfold` framework [94].

The procedure described so far was applied to the specific case of the measurement of the differential cross section for the $WbWb$ production, as a function of some basic

[4] Notice that this does not correspond to the algebraic inverse of the migration matrix, M_{ij}

[5] The case of "complete ignorance" about the process is represented by the choice of a uniform distribution

kinematic variables. In the most general case, such differential cross section with respect to a given kinematic variable X, can be written as:

$$\frac{\mathrm{d}\sigma^{fid}}{\mathrm{d}X^i} \equiv \frac{1}{L \cdot \Delta X^i} \frac{1}{\epsilon^i} \sum_j \mathcal{M}_{ij}^{-1} f_{acc}^j \cdot (N_{obs}^j - N_{bkg}^j) \tag{5.16}$$

In the previous formula, the index j runs over the bins of the observable at reconstruction level, while the index i is related to the bins at particle level. N_{obs}^j is the number of observed events in the j-th bin (our data), N_{bkg}^j the background contribution in the corresponding bin. Consistently with the notation used so far, ΔX^i represents the bin width, L the *integrated* luminosity, $\mathcal{M}^{-1}$ is the matrix applying the regularized unfolding procedure described so far. The two remaining terms, ϵ^j and f_{acc}^j, are called the efficiency and acceptance factors, respectively. The efficiency factor:

$$\epsilon^k = \frac{N_{reco\ \&\ part}^k}{N_{part}^k} \tag{5.17}$$

is defined as the ratio of generated events, that are also reconstructed, over the total number of generated events. It provides a correction, applied directly on the unfolded spectrum, on the number of events passing the truth level selection, that are not reconstructed at detector level.
The acceptance factor instead:

$$f_{acc}^k = \frac{N_{reco\ \&\ particle}^k}{N_{reco}^k} \tag{5.18}$$

is defined as the fraction of reconstructed signal events in a given bin k, that pass the particle level selection, i.e. the the number of MC events which are reconstructed and come from the fiducial phase space, over the whole reconstructed MC signal. It is thus obtained via simulation, and provides a bin-by-bin correction for the selected reco-level events that were not selected at particle level.
Together with the (fiducial) differential cross section, the integrated fiducial cross section σ^{fid} is evaluated in order to provide the normalized differential cross section defined as:

$$\frac{1}{\sigma^{fid}} \cdot \frac{\mathrm{d}\sigma^{fid}}{\mathrm{d}X^i} \tag{5.19}$$

Figures 5.1 to 5.6 show the calculated values for the corrections and the migration matrix for each of the variables considered in the analysis.

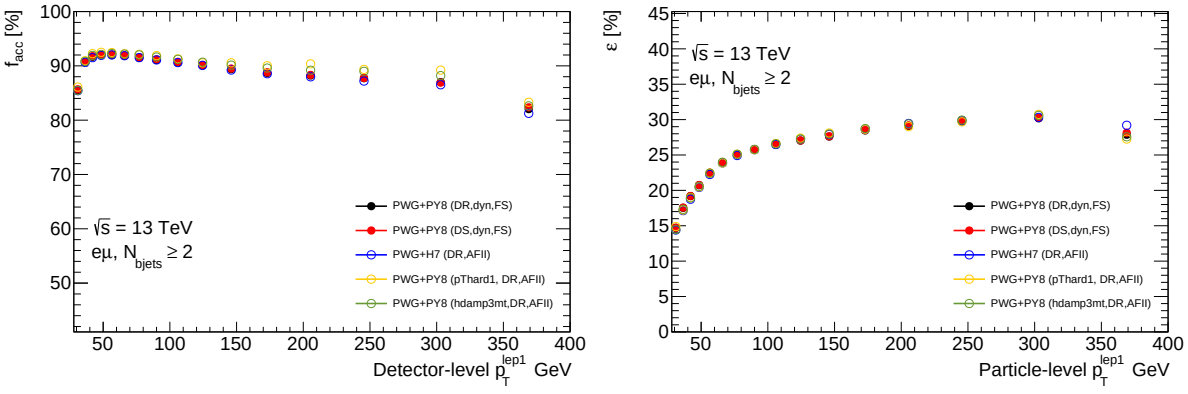

(a) (b)

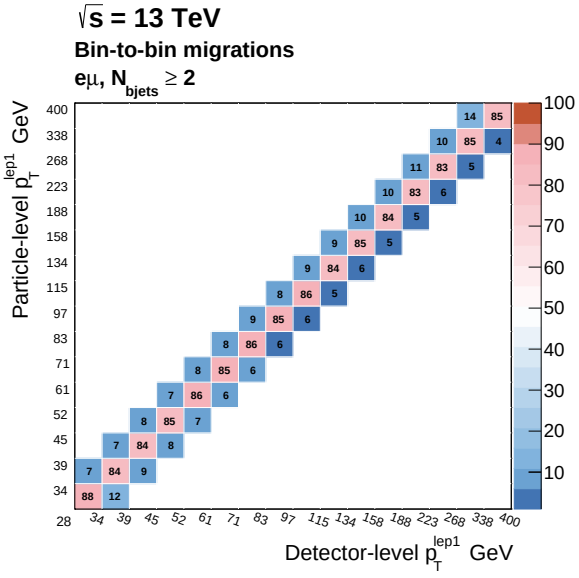

(c)

Figure 5.1: The acceptance (a) (f_{acc}) and efficiency (b) (ϵ) corrections and the migration matrix (c) for the $p_{\mathrm{T}}^{lep,1}$ variable. The nominal acceptance and efficiency corrections are shown in black. A comparison for the two corrections as evaluated from different MC generators for the signal modelling is provided, in different colors. The migration matrix shows only bins where the migration is greater than 1%.

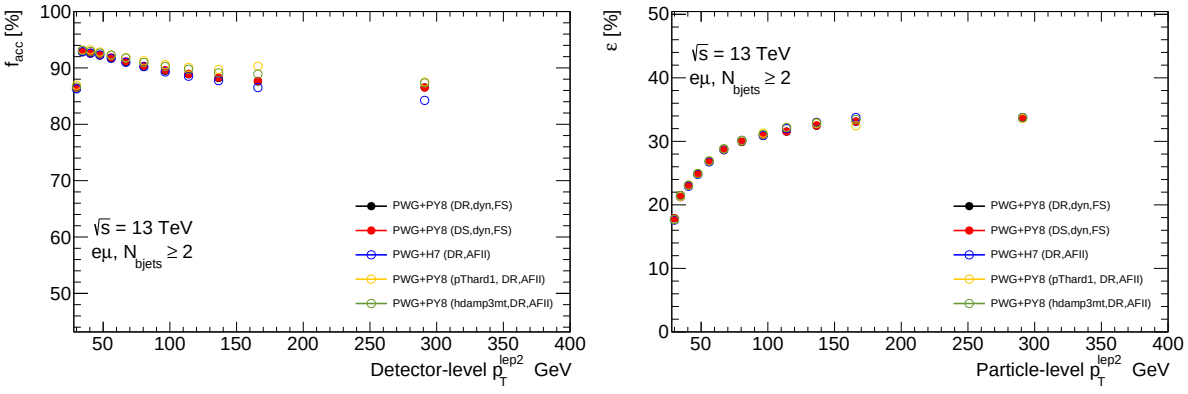

(a) (b)

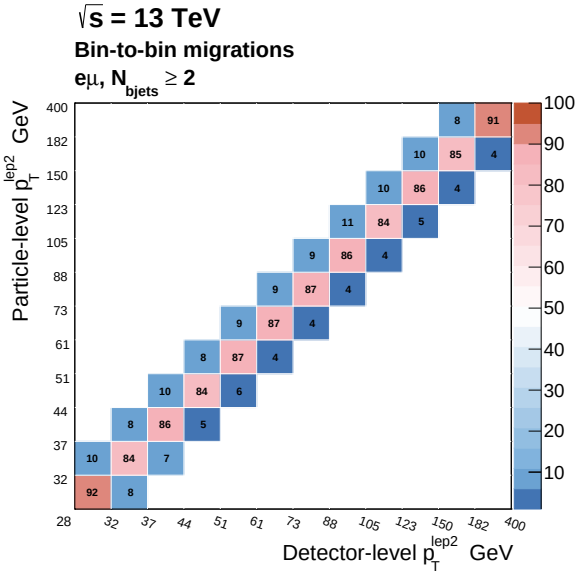

(c)

Figure 5.2: The acceptance (a) (f_{acc}) and efficiency (b) (ϵ) corrections and the migration matrix (c) for the $p_{\mathrm{T}}^{lep,2}$ variable. The nominal acceptance and efficiency corrections are shown in black. A comparison for the two corrections as evaluated from different MC generators for the signal modelling is provided, in different colors. The migration matrix shows only bins where the migration is greater than 1%.

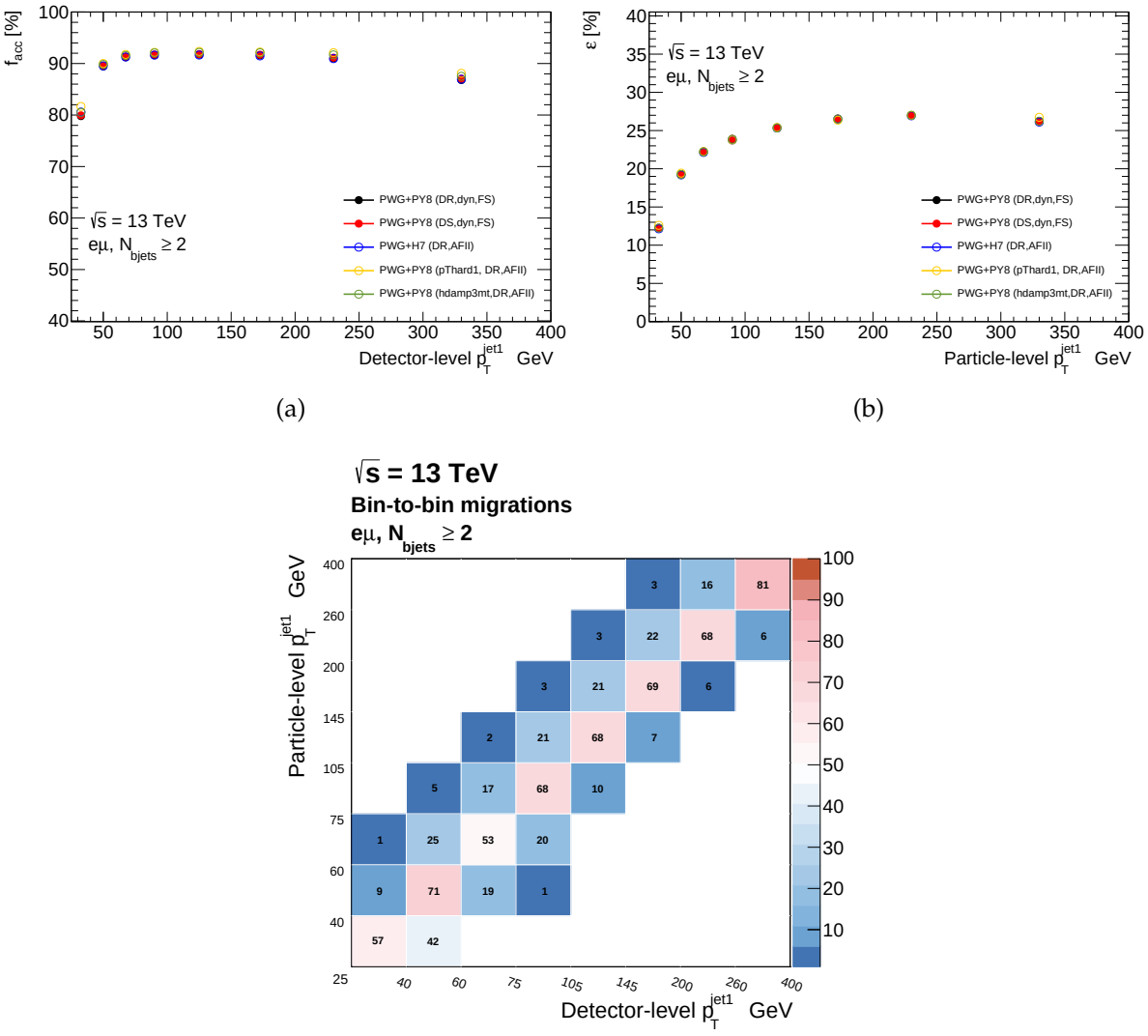

Figure 5.3: The acceptance (a) (f_{acc}) and efficiency (b) (ϵ) corrections and the migration matrix (c) for the $p_{\mathrm{T}}^{jet,1}$ variable. The nominal acceptance and efficiency corrections are shown in black. A comparison for the two corrections as evaluated from different MC generators for the signal modelling is provided, in different colors. The migration matrix shows only bins where the migration is greater than 1%.

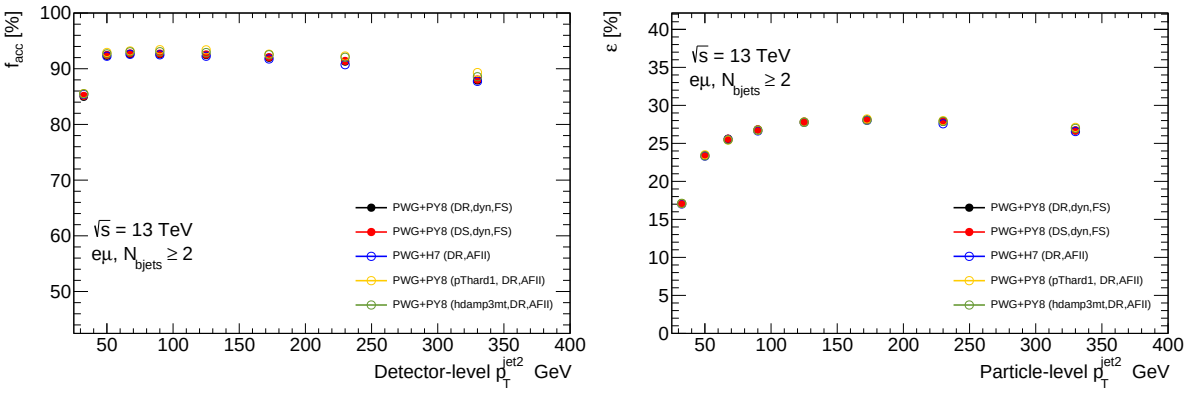

(a) (b)

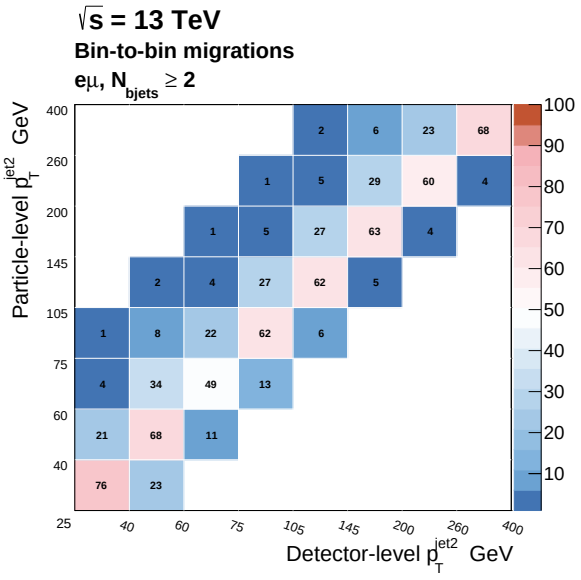

(c)

Figure 5.4: The acceptance (a) (f_{acc}) and efficiency (b) (ϵ) corrections and the migration matrix (c) for the $p_{\mathrm{T}}^{jet,2}$ variable. The nominal acceptance and efficiency corrections are shown in black. A comparison for the two corrections as evaluated from different MC generators for the signal modelling is provided, in different colors. The migration matrix shows only bins where the migration is greater than 1%.

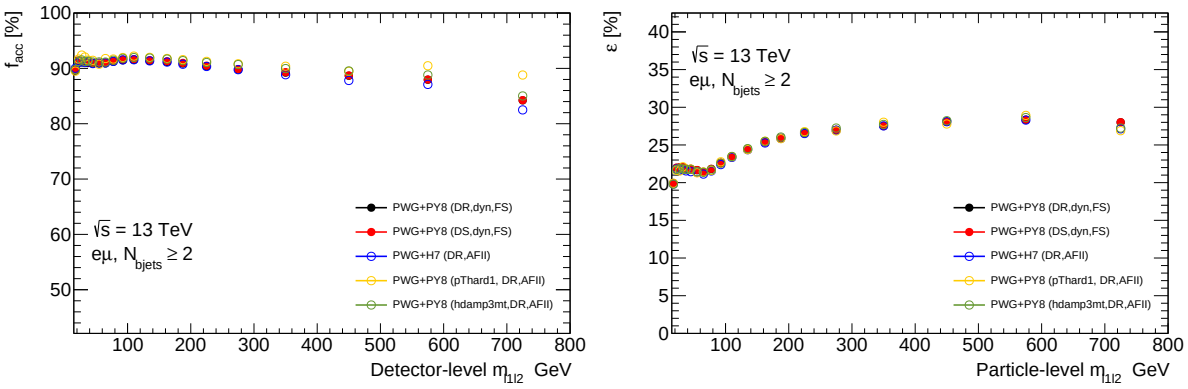

(a) (b)

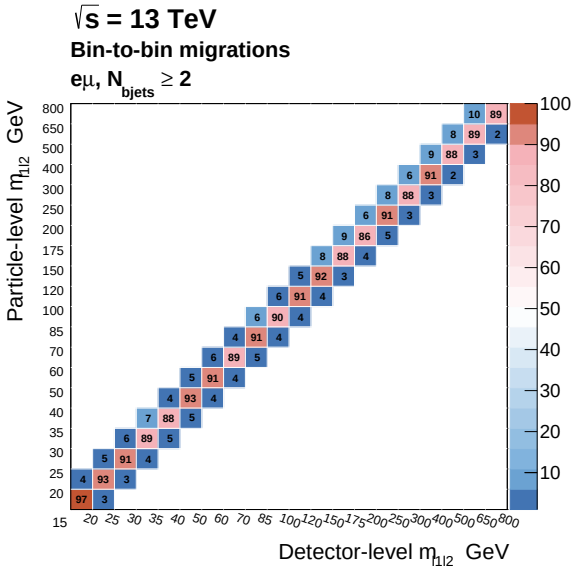

(c)

Figure 5.5: The acceptance (a) (f_{acc}) and efficiency (b) (ϵ) corrections and the migration matrix (c) for the m_{l1l2} variable. The nominal acceptance and efficiency corrections are shown in black. A comparison for the two corrections as evaluated from different MC generators for the signal modelling is provided, in different colors. The migration matrix shows only bins where the migration is greater than 1%.

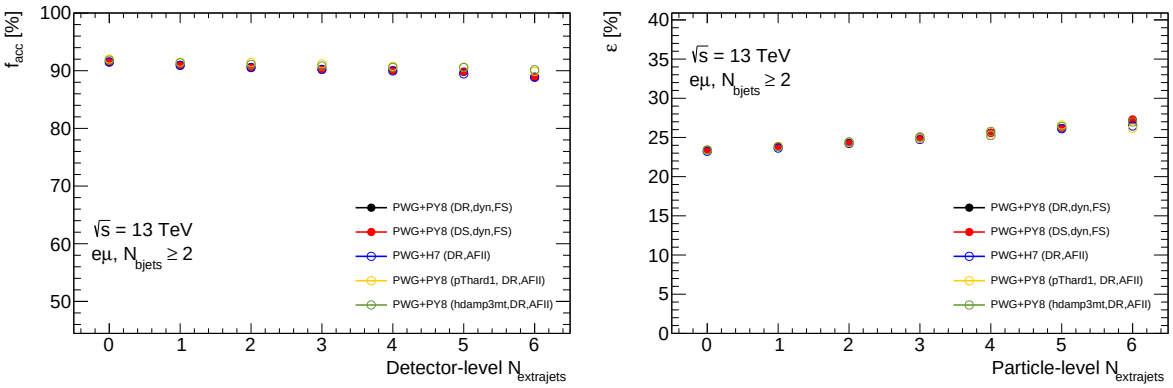

(a) (b)

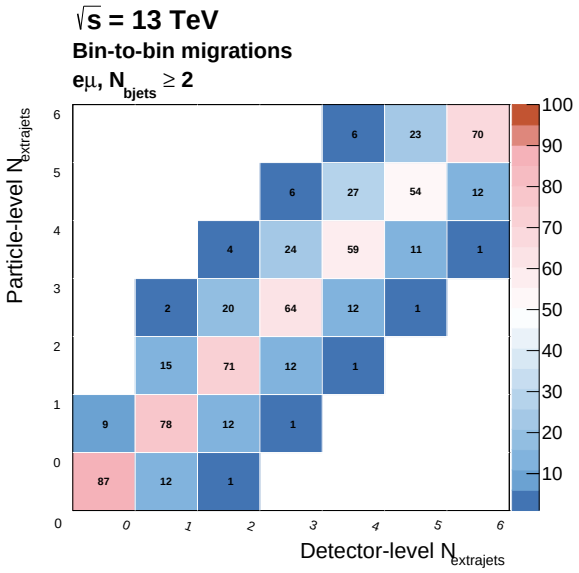

(c)

Figure 5.6: The acceptance (a) (f_{acc}) and efficiency (b) (ϵ) corrections and the migration matrix (c) for the $N_{\text{extrajets}}$ variable. The nominal acceptance and efficiency corrections are shown in black. A comparison for the two corrections as evaluated from different MC generators for the signal modelling is provided, in different colors. The migration matrix shows only bins where the migration is greater than 1%.

5.2 Resolution studies and binning selection

In order to select a binning as fine as possible, consistently with the constraints provided by resolution and statistical uncertainties, *resolution studies* were performed. These tests are based, once again, on an iterative procedure, which starts by considering a *fine* binned $T - R$ vs. T distribution. Here, T represents the true spectrum and R the reconstructed one. Introducing the resolution, which is defined according to:

$$2 \cdot \mathrm{RMS}(T - R) \tag{5.20}$$

(where RMS stands for *Root Mean Square*) in each bin of T, one proceeds by merging bins (starting from the first one defined), until the two conditions:

$$\Delta_i > \delta \cdot 2 \cdot \mathrm{RMS}_i \tag{5.21}$$

$$\sigma_{stat} \approx \frac{\sqrt{N_i}}{N_i} < k\% \tag{5.22}$$

are met. In the previous formulas Δ_i is the bin width as usual, δ a conservative factor introduced in order to account for bin asymmetries, $k\%$ the upper limit considered for the bin statistical uncertainty. Under the assumption of an ideal Gaussian resolution, a bin width equal to $2 \cdot \mathrm{RMS}$ would correspond to $\approx 68\%$ of events reconstructed in the correct bin. In the present analysis, the parameter δ and k were assumed to be equal to 1 and 5 respectively.

The selected binning for each of the variables considered in the analysis is shown in table 5.1

Table 5.1: Variables and binning employed in the analysis.

Variable	Bin Edges
$\mathrm{p}_T^{jet,1}$ [GeV]	25,40,60,75,105,145,200,260,400
$\mathrm{p}_T^{jet,2}$ [GeV]	25,40,60,75,105,145, 200,260,400
$\mathrm{p}_T^{lep,1}$ [GeV]	28,34,39,45,52,61,71,83,97,115,134,158,188,223,268,338,400
$\mathrm{p}_T^{lep,2}$ [GeV]	28,32,37,44,51,61,73,88,105,123,150,182,400
m_{l1l2} [GeV]	15,20,25,30,35,40,50,60,70,85,100,120,150,175,200,250,300,400,500,650,800
$\mathrm{N}_{extrajets}$	0,1,2,3,4,5,6

5.3 Unfolding Validation

The unfolding procedure described previously has been validated by means of two different tests: *Closure Tests* and *Stress Tests*. The description of the two is provided in the following subsections. The results of these tests showed that the binning and regularisation parameter (our number of iterations) selected lead to a stable unfolding procedure, and thus no additional uncertainties related to the specific unfolding method selected must be introduced.

5.3.1 Closure Tests

Closure Tests provide a check of the consistency of the unfolding procedure and of the stability of the selected binning. The goal is to check whether it is possible to correctly recover a statistically independent sample, drawn from the same modelling employed for the calculation of the unfolding corrections. The procedure adopted in order to perform the stress tests, involves the following steps:

1. *Sub-samples formation*: First, the signal MC sample is divided into two statistically independent sub-samples, called respectively *Half 0* and *Half 1*, by assigning randomly each event to one of the two sub-samples;

2. *Role assignment*: One of the two sub-samples assumes the role of *pseudo-data*, while the other is used in order to calculate the unfolding corrections. In the present analysis, the role of pseudo-data was assigned to the half0 sample, while the half1 was employed for the corrections calculation;

3. *Unfolding*: The pseudo-data are unfolded with the corrections calculated using the other sub-sample, using the same Bayesian Iterative procedure described before. The number of iterations considered for this step was equal to 4.

4. *Check of the results*: Once the unfolding is completed, the unfolded pseudo-data distribution gets compared to the corresponding true spectrum. In order to asses the degree of compatibility between the unfolded spectrum and the predictions, as given by the two halves, the χ^2 was evaluated, using a covariance matrix accounting only for the statistical uncertainties. The corresponding p-values were thus obtained.

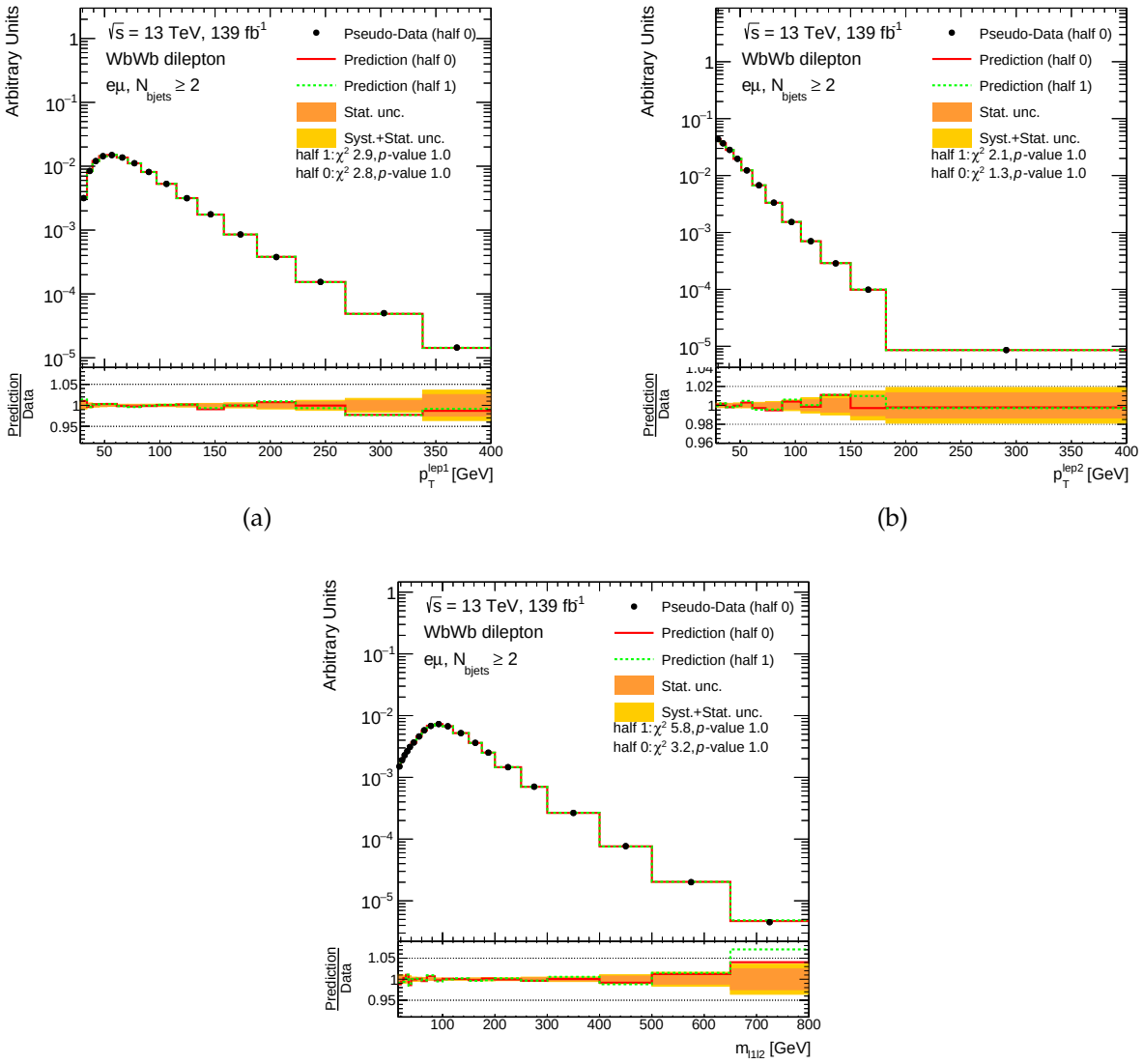

Figure 5.7: Closure tests for the relative differential cross-section measurements with respect to (a) $p_{\mathrm{T}}^{lep,1}$, (b) $p_{\mathrm{T}}^{lep,2}$, (c) m_{l1l2}. The black point correspond to the pseudo-data (half0), the unfolding was performed by evaluating the corrections from half1. The predictions corresponding to the two halves are shown, as well as the agreement between the unfolded distribution and the halves, as indicated by the χ^2 and the corresponding p-value.In the bottom panel, the ratio between predictions and data is shown, together with the bands corresponding to systematic and total uncertainty.

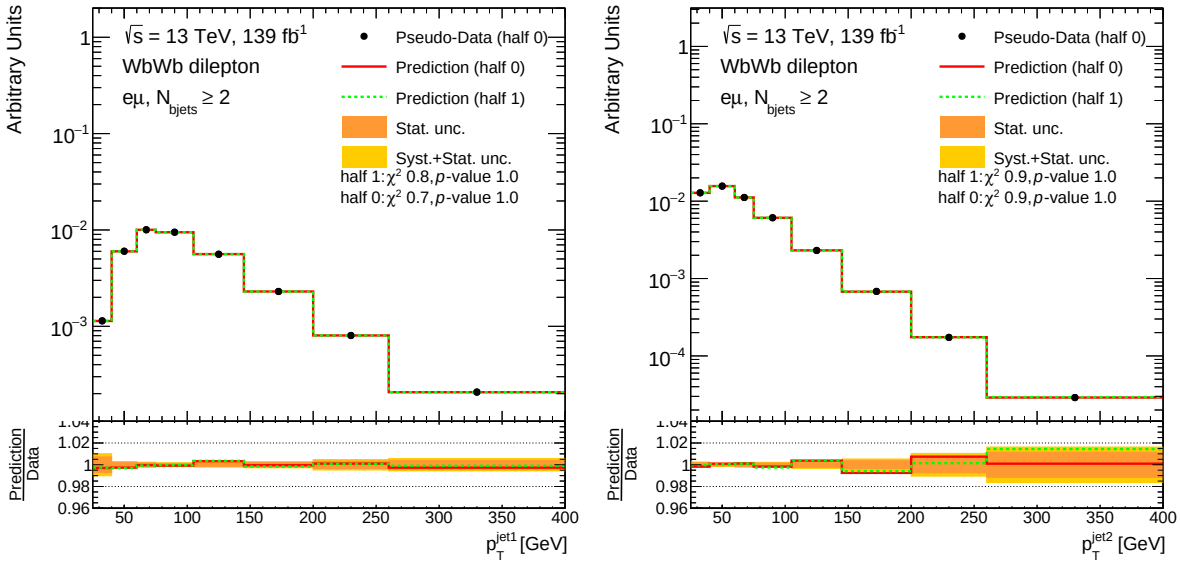

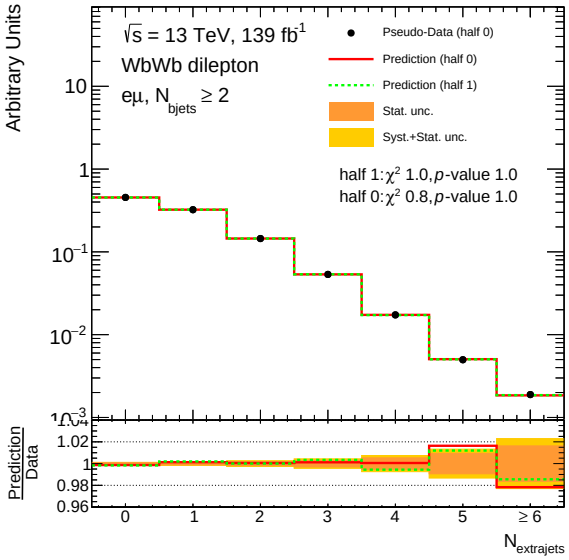

Figure 5.8: Closure tests for the relative differential cross-section measurements with respect to (a) $p_{\mathrm{T}}^{jet,1}$, (b) $p_{\mathrm{T}}^{jet,2}$, (c) $N_{extrajets}$. The black point correspond to the pseudo-data (half0), the unfolding was performed by evaluating the corrections from half1. The predictions corresponding to the two halves are shown, as well as the agreement between the unfolded distribution and the halves, as indicated by the χ^2 and the corresponding p-value. In the bottom panel, the ratio between predictions and data is shown, together with the bands corresponding to systematic and total uncertainty.

5.3.2 Stress Test

Stress tests allow to perform an additional check on the unfolding procedure: since a specific MC sample is chosen for evaluating the unfolding corrections, it is necessary to check whether the choice introduces a bias when performing the unfolding or not. The test consists of reweighting the MC used, in order to change the shape of the distributions. The varied distribution obtained is used as pseudo-data and unfolded with the nominal MC response. The resulting distribution is compared then with the reweighted MC at particle level.
An important difference to highlight between closure and stress tests is in the fact that while closure tests are performed in order to verify that the unfolding procedure is stable from a statistical point of view, i.e. they allow to assess the unfolding performance in presence of statistical fluctuations, stress tests allow to verify if the unfolding works properly when data are drawn from a different distribution with respect to the one from which the unfolding corrections have been calculated.

The reweighting was performed by evaluating the factor used to re-scale the distributions, according to:

$$f(X) = \frac{(D-B)(X)_{observed}}{S(X)_{expected}} = \frac{S(X)_{observed}}{S(X)_{expected}} \tag{5.23}$$

with X variable with respect to which the stress is introduced, D, B and S respectively the data, background and signal distributions. In the case of the present analysis, X= $p_T^{lep,1}, p_T^{jet,1}, m_{l_1 l_2}$.

The tests have been performed for each of the variables under consideration, which have been unfolded with all the reweighting shapes. Stress tests performed using a reweighting function based on the m_{l1l2} variable are shown, for all the kinematic observables in figures 5.9 and 5.10. The plots concerning the stress tests performed using the other reweighting functions are shown in Appendix A.

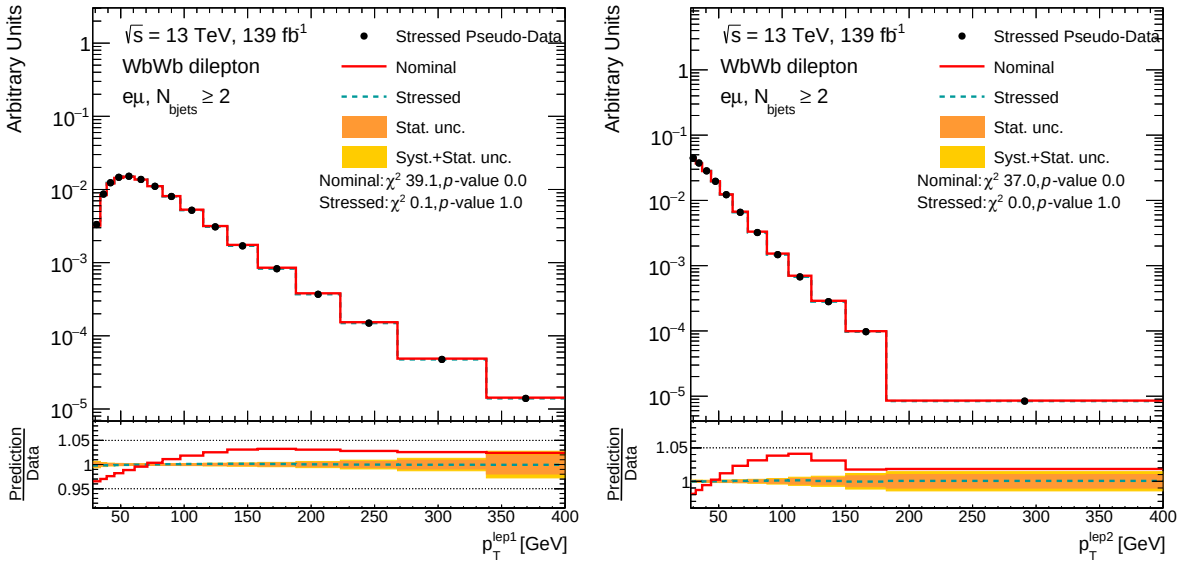

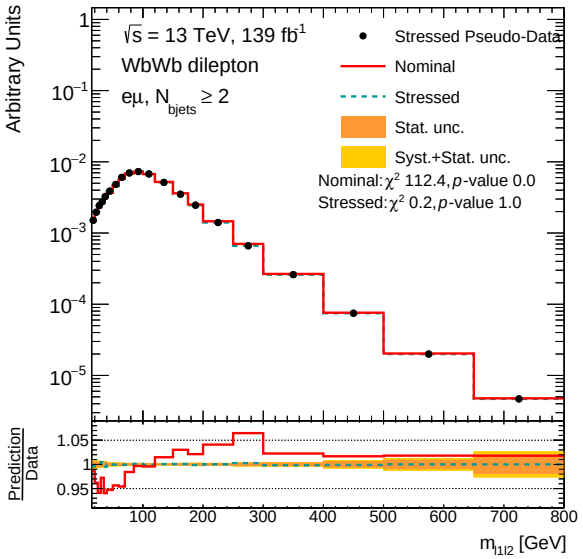

Figure 5.9: Stress tests for the relative differential cross-section, measured as a function of the $p_{\mathrm{T}}^{\mathrm{lep},1}$ (a), $p_{\mathrm{T}}^{\mathrm{lep},2}$ (b) and m_{l1l2} (c) variables, using a reweight function based on the m_{l1l2} variable distribution. A comparison between the stressed and nominal predictions is provided. In the bottom panel, the prediction/data ratio as a function of the variable is shown. The statistical and total uncertainty bands are shown in yellow and orange respectively.

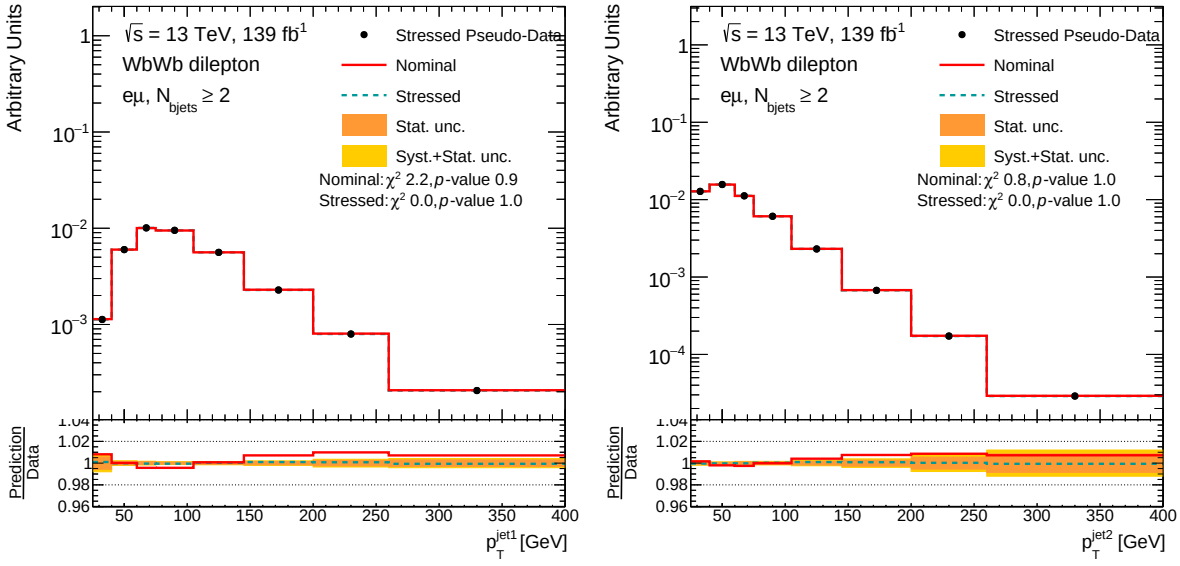

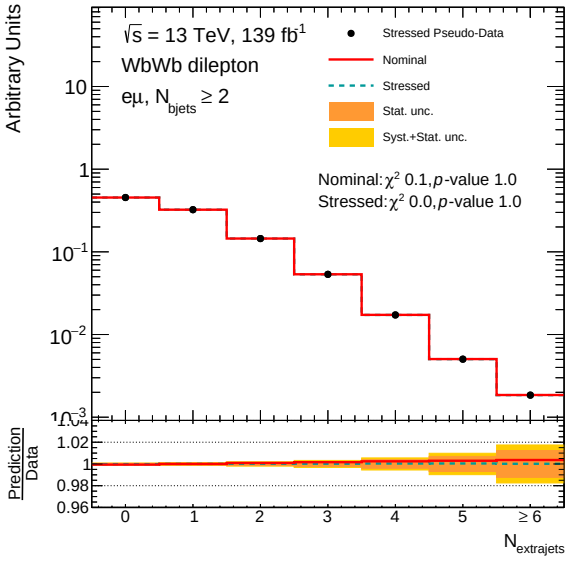

Figure 5.10: $p_{\mathrm{T}}^{\mathrm{jet},1}$ (a), $p_{\mathrm{T}}^{\mathrm{jet},2}$ (b) and N_{extrajet} (c) variables, using a reweight function based on the m_{l1l2} variable distribution. A comparison between the stressed and nominal predictions is provided. In the bottom panel, the prediction/data ratio as a function of the variable is shown. The statistical and total uncertainty bands are shown in yellow and orange respectively.

5.4 Systematic uncertainties

The sources of systematic uncertainty affecting the measurement of the differential cross-section are multiple. In particular, the uncertainties related to detector effects and due to signal and background MC modelling were found to be the most relevant. Systematics evaluation is done by unfolding the varied (i.e. obtained by modifying the values of the corresponding systematic) MC spectrum (detector level) with nominal corrections, and then comparing the results of the unfolding procedure to the particle-level distribution from the generator used for the original detector level spectrum.

5.4.1 Detector systematics

The detector systematics account for the assumptions made in the implementation of detector simulation and the overall quality of the detector simulation used for modelling the apparatus response to the reconstructed objects. In particular, the detector systematics considered in the analysis include:

Leptons uncertainties

The lepton uncertainties are associated to the lepton energy/momentum scale and resolution, both of them affecting the leptons momentum. Moreover, the calibration procedure used to evaluate lepton reconstruction and identification efficiencies is characterized by an associated uncertainty, which propagates in the analysis. Similarly for the trigger efficiencies. The estimation of the efficiencies and the associated uncertainties are described in [95, 96]

Jets uncertainties

Jets uncertainties are related to the jet energy scale (JES) and resolution (JER), together with the one on jet vertex tagging (JVT). The uncertainty on JES and JER was estimated by varying the jet energies according to the uncertainties from simulations and in-situ calibration measurements, following the recommendations for the full Run 2 [62]. The JVT uncertainty is assessed by varying the scale factor associated to the JVT requirement [97].

$b-$tagging

$b-$jets are identified via a DL1r algorithm, as introduced in chapter 3. Scale factors[6] are applied to the simulations, with the purpose to correct the jet flavour tagging effi-

[6] ration between MC and data efficiencies

ciencies and matching the experimentally observed ones in data [63]. The corrections are applied for the tagging efficiency of $b-$jets and mis-tag rates of $c-$ and light jets.

Pileup modelling

The uncertainty on the reweighting procedure applied in order to correct for the pile-up profile in MC is obtained by varying the scale factors by $\pm 1\sigma$.

5.4.2 Signal modelling

Limited understanding of the signal process modelling from the generator is an important source of uncertainty. The impact of it is evaluated by repeating the unfolding procedure with alternative predictions and comparing the resulting particle level distributions. In the following, a breakdown of the signal modelling uncertainties is provided.

Hadronization model

The particular hadronization model of choice is accounted via the introduction of an associated uncertainty. The evaluation is done using the Powheg+Herwig7 sample.

Scales

The choice of the μ_R and μ_F scales in the hard-scatter and in the showering is performed using Powheg+Pythia8. Here, μ_R and μ_F are varied simultaneously by a factor 0.5 and 2.0. The scales of the showering are varied according to the Var3c [98] A14 tune variation. These variations mainly affect the ISR.

FSR

The uncertainty on the FSR simulation is obtained using the Powheg+Pythia8 sample. The renormalization scale in the final-state shower is varied by factors 2 and 0.5 with respect to the nominal value.

$\mathbf{h_{damp}}$

The uncertainty on the h_{damp} parameter is estimated using a dedicated Powheg+Pythia8 sample where h_{damp} is multiplied by a factor 2 with respect to the nominal value.

Matching

The matching uncertainty is evaluated by comparing the nominal sample with an alternative one, obtained by setting the Pythia8 $p_{T,hard}$ parameter to 1.

Lineshape

This uncertainty is associated to the top pair system. Analyses making use of the top-quark decay properties depend on the modelling of its width and the lineshape considered in MC generators. The related uncertainty is evaluated via a comparison of the nominal sample with an alternative one where, in the $t\bar{t}$ component, the top quarks decay is modelled using MadSpin. In this alternative sample, the nominal tW one is used.

Top quark mass

The top quark mass is known with a precision of approximately 0.5 GeV [4]. Since the kinematic of the decay product depends on the quark mass (and so does the probability of passing the selection requirements), this uncertainty has implications on the analysis.
In order to estimate the uncertainty related to a shift of $\pm$ 0.5 GeV on the top mass, it was first verified that the relation between the top mass value and the differential cross-section is linear. Then, the uncertainty induced by a $\pm$ 3.5 GeV variation was evaluated and lastly the result was divided by 7.

PDF uncertainties

The choice of a particular PDF has consequences on the efficiency, acceptance and potentially the response matrix too. To asses this effects, an event-by-event reweighting was applied to the nominal $t\bar{t}$ and tW samples was applied, using the PDF4LHC15 prescription, described in [76].

DR vs DS scheme

It was mentioned how two different schemes can be adopted in principle in order to treat the overlap between $t\bar{t}$ and tW production, diagram removal and diagram subtraction. The nominal signal applies the DR scheme, while DS is used as alternative sample. This uncertainties accounts for the effect of changing scheme, and affects only the tW modelling, since the $t\bar{t}$ sample is the same for both the nominal and alternative case.

5.4.3 Uncertainties on the background modelling

Z+jets

The uncertainty on the Z+jets process is a global uncertainty applied on the MC prediction of the Z+jets background components. It is based on variations of the PDF, α_s, μ_F and μ_R, as calculated in [99].

Diboson and $t\bar{t}V$

It corresponds on the uncertainty on the cross section calculation for the $t\bar{t}Z$ and $t\bar{t}W$ processes, composing the $t\bar{t}V$ sample. They are set to 13.3%.

Fake and non-prompt leptons background

A 50% normalisation uncertainty is applied to the fake and non-prompt leptons background, reflecting the uncertainty in evaluating it from the MC simulations.

5.4.4 Other sources of uncertainty

Finite MC sample statistics

The limited statistics of the MC samples introduces an additional source of uncertainty. In order to evaluate its impact, pseudo-experiments are performed. They consist in smearing the number of events in each bin via a Gaussian, with mean equal to the yield of the bin and standard deviation equal to the uncertainty of the bin. The smeared spectrum is then unfolded and the procedure is replicated 10 thousand times. At the end, the final statistical uncertainty is evaluated from the RMS over all the pseudo experiments. The resulting uncertainty was found to be below 0.5%, up to a value of $1-2\%$ in the tails of some of the distributions.

5.4.5 Integrated Luminosity

The uncertainty of the combined integrated luminosity, over the period 2015-2018, is 2.1% [100]. It was obtained from the LUCID-2 detector, and complemented via the measurements performed by the ID and calorimeters. In order to propagate such uncertainty to the unfolded results, the value of the luminosity is varied by $\pm$ 2.1% in the reconstructed simulated spectra and unfolding them using the nominal corrections.

Data statistics

The uncertainty due to data statistics is propagated in the unfolding by creating Poisson smeared pseudo-experiments, which later undergo the unfolding procedure.

5.4.6 Systematic uncertainties summary plots

Summary plots for the impact of the systematics listed so far were produced. To this purpose, the following arbitrary convention for both grouping and naming of the systematic uncertainties was considered:

- *Parton Shower*: Includes the uncertainties related to the parton shower (PS) modelling;
- *Hard scattering*: are the uncertainties related to the hard scattering modelling. They include the matching and lineshape uncertainties;
- *Generator Parameters*: are uncertainties associated to the particular choice of the generator parameters, such as the renomarlization and factorisation scales, the ISR and FSR parameters, the PDF . This uncertainty group includes also the MC simulations statistics;
- *Jets*: Jet uncertainties include the JES and JER, together with the JVT scale factor;
- $t\bar{t}$ *modelling*: includes the $t\bar{t}$ normalisation, h_{damp} and top mass uncertainties;
- tW *modelling*: are the uncertainties on the modelling of the tW contribution to the signal. In particular, they correspond to the uncertainty on the tW cross section and the one on the DR procedure;
- *Flavour tagging*: are the uncertainties on the $b-$tag scale factors;
- *Background uncertainties*: are related to the background modelling;

Figures 5.11 and 5.12 show the corresponding plots, containing the summary of the uncertainties on the measured differential cross-section, respectively for the lepton and jet related variables. The statistical and total (sum in quadrature of the statistical and systematic one) uncertainties are shown as well, while the least impact-full contributions are not presented.

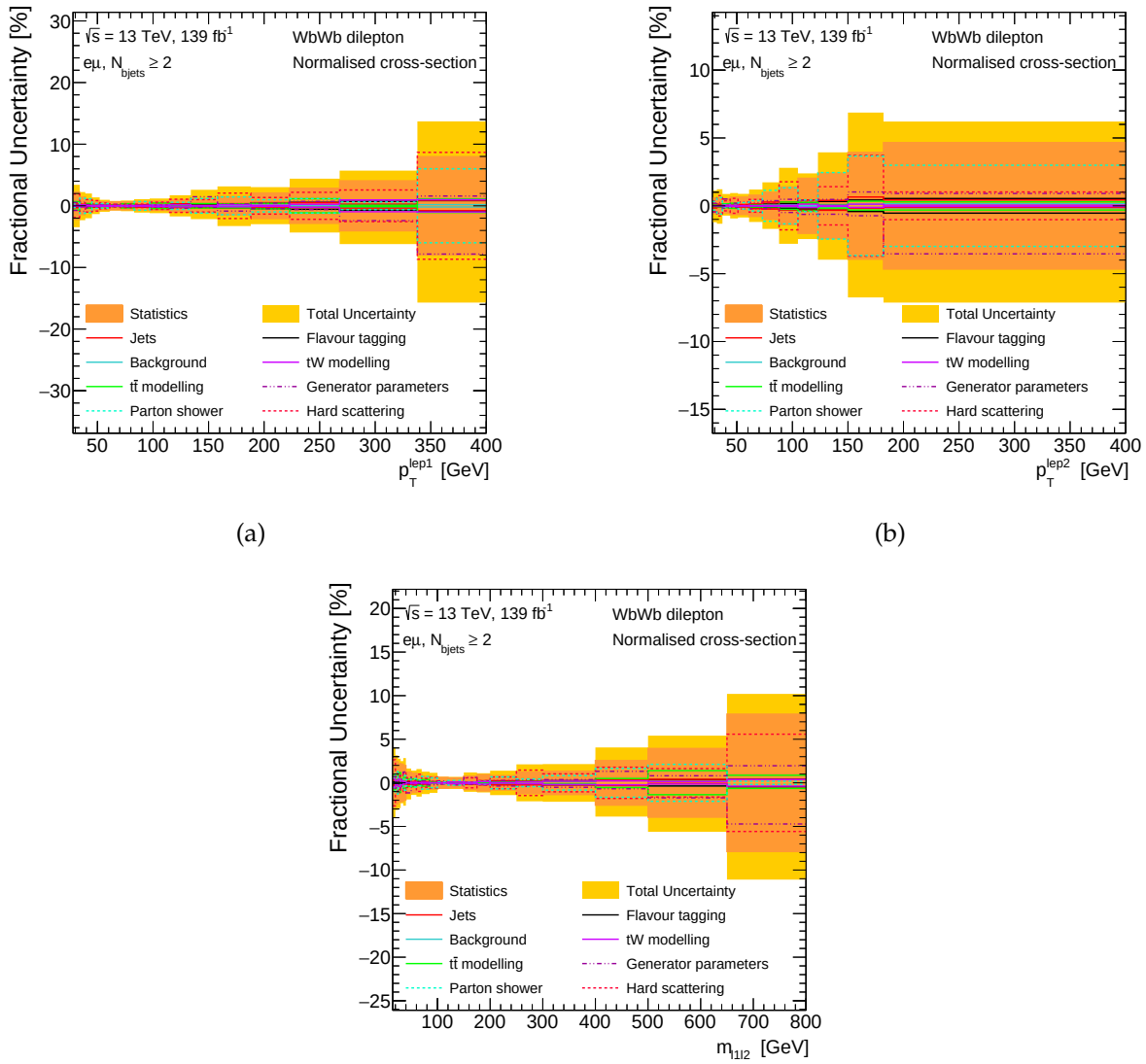

(a)

(b)

(c)

Figure 5.11: Uncertainties breakdown for the relative (normalised) differential cross-sections measurement as a function of (a) $p_{\mathrm{T}}^{\mathrm{lep},1}$, (b) $p_{\mathrm{T}}^{\mathrm{lep},2}$, (c) m_{l1l2}.

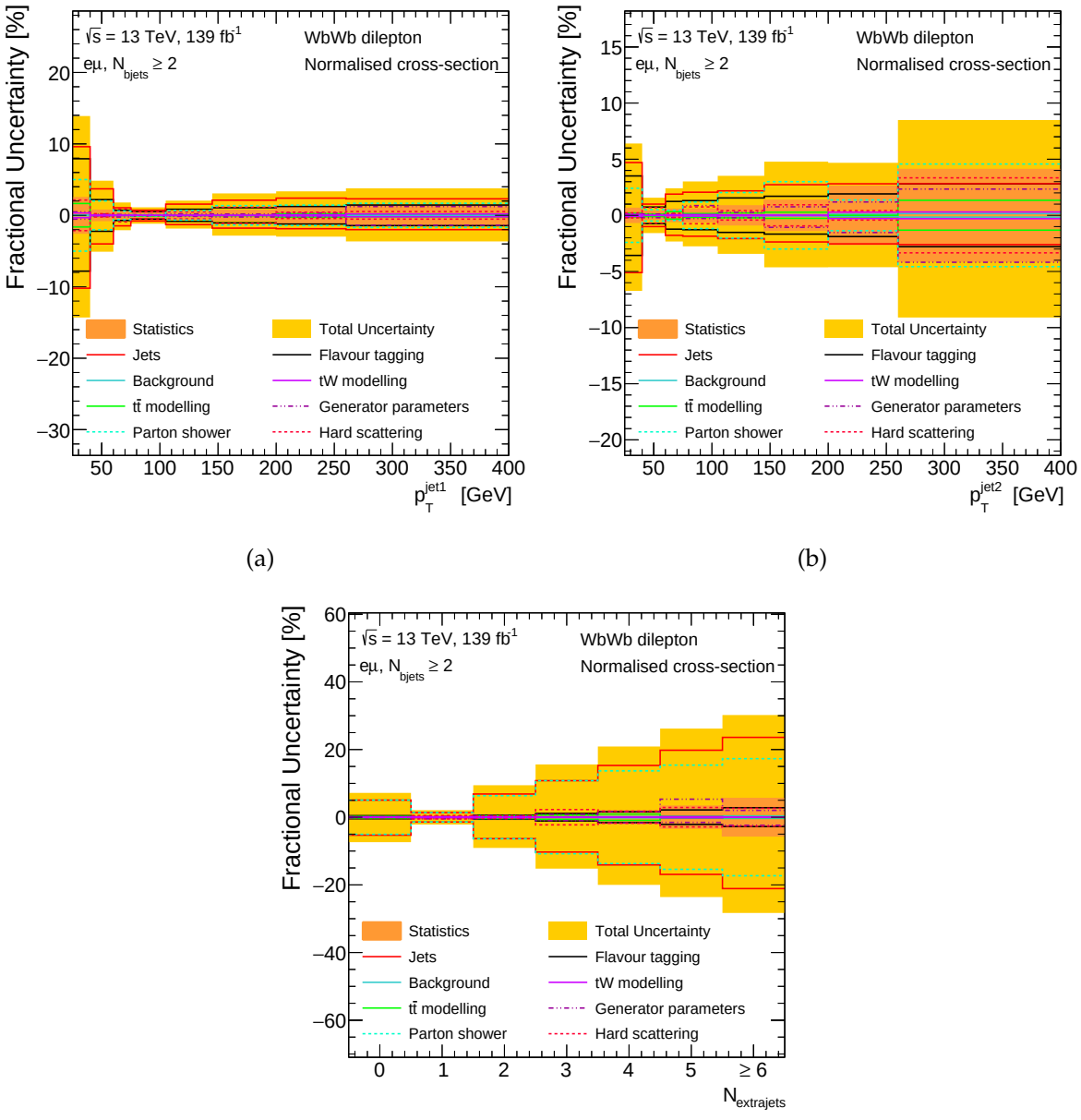

(a)

(b)

(c)

Figure 5.12: Uncertainties breakdown for the relative (normalised) differential cross-sections measurement as a function of (a) $p_{\mathrm{T}}^{\mathrm{jet},1}$, (b) $p_{\mathrm{T}}^{\mathrm{jet},2}$, (c) $N_{\mathrm{extrajets}}$.

5.5 χ^2 evaluation

To estimate the agreement between the available theoretical predictions and the measured differential-cross sections, the χ^2 has been computed. To calculate the χ^2, the relation

$$\chi^2 = V^T \times Cov^{-1} \times V \tag{5.24}$$

was applied, where Cov is the covariance matrix, and V the vectors of residuals, which are defined as the difference between the measured differential cross section and the prediction. A degree of freedom was subtracted, since only the normalised differential cross sections were considered, leading to a reduction of the overall dimensions of V and Cov. The covariance matrix accounts for both the statistical and systematic uncertainties. For each of the considered systematic uncertainties, the corresponding covariance matrix elements c_{ij} were evaluated according to:

$$c_{ij} = \sigma_i \cdot \sigma_j \tag{5.25}$$

where

$$\sigma_i = \frac{|\delta u_i| + |\delta d_i|}{2} \tag{5.26}$$

Where the labels δu_i and δd_i refer respectively to the up and down variations of a given uncertainty in the $i-$th bin. The sign of σ_i was determined according to the convention:

1. sign(σ) = sign(δu), if $\delta u \cdot \delta d < 0$;
2. sign(σ) = sign(δu), if $\delta u \cdot \delta d > 0$ and $|u| > |d|$;
3. sign(σ) = -sign(δu), if $\delta u \cdot \delta d > 0$ and $|u| < |d|$;

The statistical uncertainties components are instead obtained from pseudo-experiments. First, each bin was smeared either with a Poisson or Gaussian distribution (respectively for the data and MC statistical component). In the latter case, the mean was set equal to the bin content, which on turn corresponds to the sum of weights. The sigma of the Gaussian instead is equal to the square root of the sum of said weights. The corresponding c_{ij} values were then obtained as:

$$c_{ij} = \langle (x_i + \langle x_i \rangle)(x_j - \langle x_j \rangle) \rangle \tag{5.27}$$

with x_i and x_j post-unfolding values of the pseudo-experiments in the corresponding bins. The total systematic component is thus obtained as the sum of each covariance matrix, while the total covariance matrix is defined as the sum of the statistical and systematic components.
From the reduced χ^2/NDF, the corresponding $p-$value was extracted.

5.6 Results

The measurements of the relative[7] fiducial differential cross-section as a function of the basic kinematic observables, as introduced in 4.3, is discussed in the present section. For each of the measurements, a comparison is provided with the available theoretical predictions introduced in section 4.1.2. The choice of considering the relative differential cross-section relies on the fact that many of the systematic uncertainties considered have a small effect on the shape of the distribution, and can be cancelled by taking the ratio $\frac{1}{\sigma}\frac{\mathrm{d}\sigma}{\mathrm{d}X}$. The results of the measurement of the relative differential cross-section in the fiducial phase space previously defined are shown in figures 5.14 to 5.19.

To assess the degree of compatibility with each of the predictions considered, the corresponding χ^2 and $p-$values are evaluated, according to the method presented in 5.5. The obtained values are shown in tables 5.2 and 5.3. From them, it can be noticed that the best and worst agreement between the measured differential cross-sections and the considered predictions is obtained in the measurement of the differential cross-section as a function of the $p_{\mathrm{T}}^{\mathrm{jet},2}$ and m_{l1l2}, respectively. The former, in particular, is well described by all available predictions, with the sole exception of h_{damp}, whereas the latter is poorly described by all of them. As a general remark, it can also be noticed how none of the available predictions provides a good description of all the measured cross sections simultaneously, with the worst agreement corresponding to the alternative h_{damp} and pthard predictions. The best agreement between measurements and predictions is obtained, on average, from PWG+H7. The same prediction however do not agrees with the measurement of the cross-section as a function of $N_{extrajets}$. The same thing occurs with $bb4l$. On the other hand, PWG+H7 is the only prediction showing a good agreement with the leading lepton case. It can also be noted how the PWG+PY8+Madspin (DR) prediction provides an overall better agreement with respect to the PWG+PY8 sample with dynamic scales.
An additional measurement of the total fiducial cross section was performed. To this purpose, the same unfolding procedure applied for the differential cross-section has been applied to a single-bin distribution, thus considering a 1×1 unfolding matrix. As a consequence, the procedure in this case reduces to a simple division between the number of reconstructed events in data, after the application of the acceptance correction and the subtraction of the background contribution, and the efficiency.

The value of the total fiducial cross-section obtained is

$$\sigma_{fid} = 5.97 \pm 0.01(\mathrm{stat.})^{+0.30}_{-0.33}(\mathrm{syst.})\mathrm{pb}. \tag{5.28}$$

[7]Normalized by the total cross section

Table 5.2: Summary of the evaluated χ^2 and corresponding $p-$values obtained by comparing the measured fiducial differential cross-sections, as a function of the variables listed in the first column, with the NLO+PS predictions available. The uncertainties on the predictions are not included.

Observable	PWG+PY8 (DYN, DR)		PWG+PY8 (DR)		PWG+H7		BB4L		PWG+PY8 (DS)	
	χ^2/NDF	p-value	χ^2/NDF	p-value	χ^2/NDF	p-value	χ^2/NDF	p-value	χ^2/NDF	p-value
p_T^{lep1}	40/15	< 0.01	42/15	< 0.01	19/15	0.22	23/15	0.08	31/15	< 0.01
p_T^{lep2}	26/11	< 0.01	27/11	< 0.01	15/11	0.20	17/11	0.11	21/11	0.03
p_T^{jet1}	15/7	0.03	15/7	0.03	9/7	0.22	14/7	0.05	15/7	0.03
p_T^{jet2}	5/7	0.64	5/7	0.66	2/7	0.98	6/7	0.53	5/7	0.61
m_{l1l2}	56/19	< 0.01	56/19	< 0.01	67/19	< 0.01	33/19	0.02	51/19	< 0.01
$N_{extrajets}$	7/6	0.29	7/6	0.29	27/6	< 0.01	22/6	< 0.01	6/6	0.38

Table 5.3: Summary of the evaluated χ^2 and corresponding $p-$values obtained by comparing the measured fiducial differential cross-sections, as a function of the variables listed in the first column, with the NLO+PS predictions available. The uncertainties on the predictions are not included.

Observable	PWG+PY8 (DS, DYN)		HDAMP		PTHARD		PWG+PY8+MADSPIN (DR)	
	χ^2/NDF	p-value	χ^2/NDF	p-value	χ^2/NDF	p-value	χ^2/NDF	p-value
p_T^{lep1}	30/15	0.01	56/15	< 0.01	42/15	< 0.01	38/15	< 0.01
p_T^{lep2}	21/11	0.04	30/11	< 0.01	31/11	< 0.01	22/11	0.03
p_T^{jet1}	15/7	0.03	35/7	< 0.01	16/7	0.02	13/7	0.08
p_T^{jet2}	5/7	0.60	17/7	0.02	8/7	0.31	4/7	0.74
m_{l1l2}	50/19	< 0.01	54/19	< 0.01	56/19	< 0.01	37/19	< 0.01
$N_{extrajets}$	7/6	0.37	7/6	0.32	18/6	< 0.01	7/6	0.33

The result is shown in figure 5.13, where it is compared with all the predictions considered in the analysis. The total fiducial cross section measurement has its main sources of uncertainties in the luminosity and flavour tagging efficiency, with other relevant contributions being the lepton isolation, JES and the signal modelling, where the main uncertainties in the latter are on the hadronisation model and FSR.

The noticeable difference between the total cross-section prediction from the $bb4l$ and the other generators is related to the different perturbative order considered for the corrections. For $bb4l$ the calculation is performed at NLO+PS accuracy, whereas for the others at NNLO+NNLL. Since the available k-factor for the $bb4l$ sample is of the order of $\simeq 14\%$, the difference observed can be understood on the basis of the different perturbative order of the calculation.

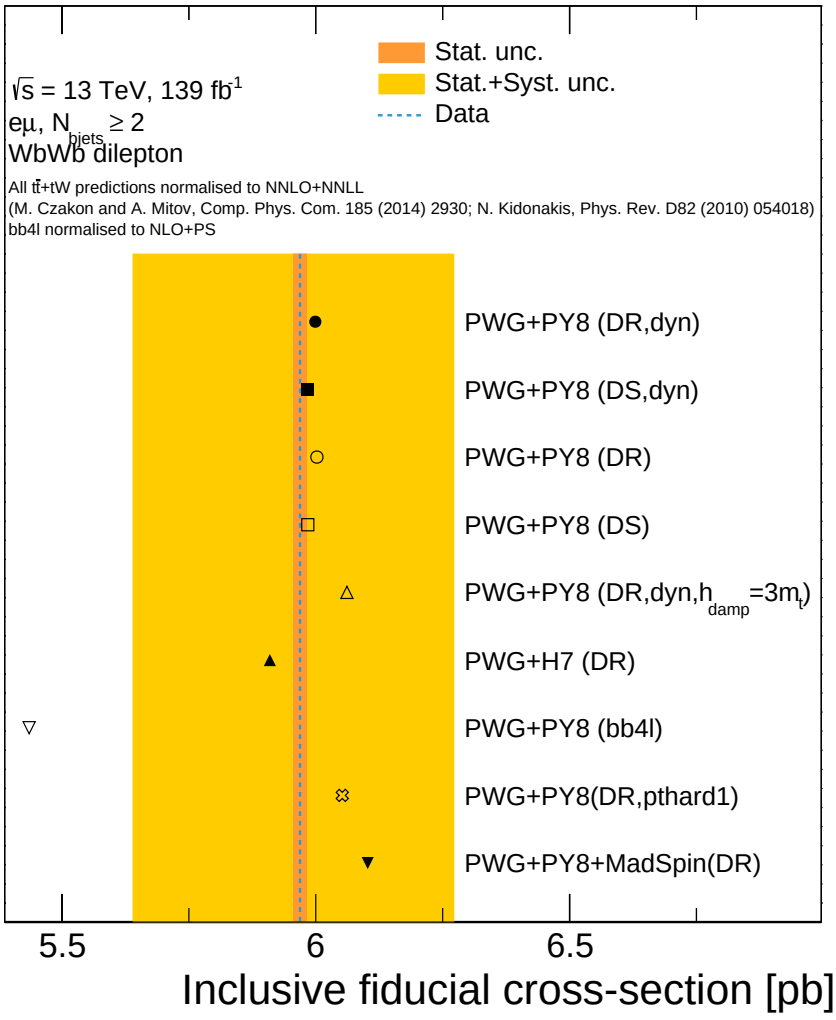

Figure 5.13: Measurement of the inclusive cross section in the fiducial phase space (green dashed line) compared with several predictions, as labeled in the right end side of the plot. The orange and yellow bands provide the statistical and total (statistical $\oplus$ systematic) uncertainties, respectively.

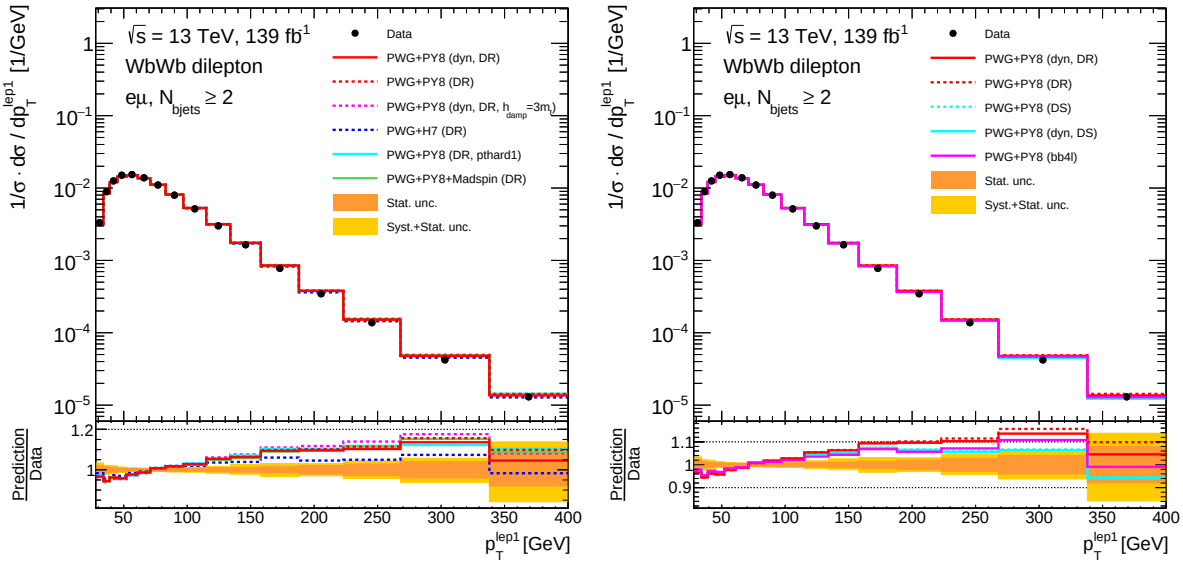

(a) (b)

Figure 5.14: The results of the unfolding procedure described for the relative differential cross-section measurement, as a function of the $p_{\mathrm{T}}^{\mathrm{lep},1}$ variable. The cross section is unfolded at particle level, in the fiducial phase-space. Data points are represented by black dots and are placed at the center of the corresponding bin. A comparison with several alternative predictions is provided, as listed in the box in the top panel. In the bottom panel, the ratio between predictions and data is shown. The orange band represents the statistical uncertainty, while the yellow band shows the combined statistical and systematic uncertainties. On the left hand side, predictions from different generators making use of the DR scheme are presented. On the right hand side, different schemes for the interference are considered, together with the $bb4l$ sample.

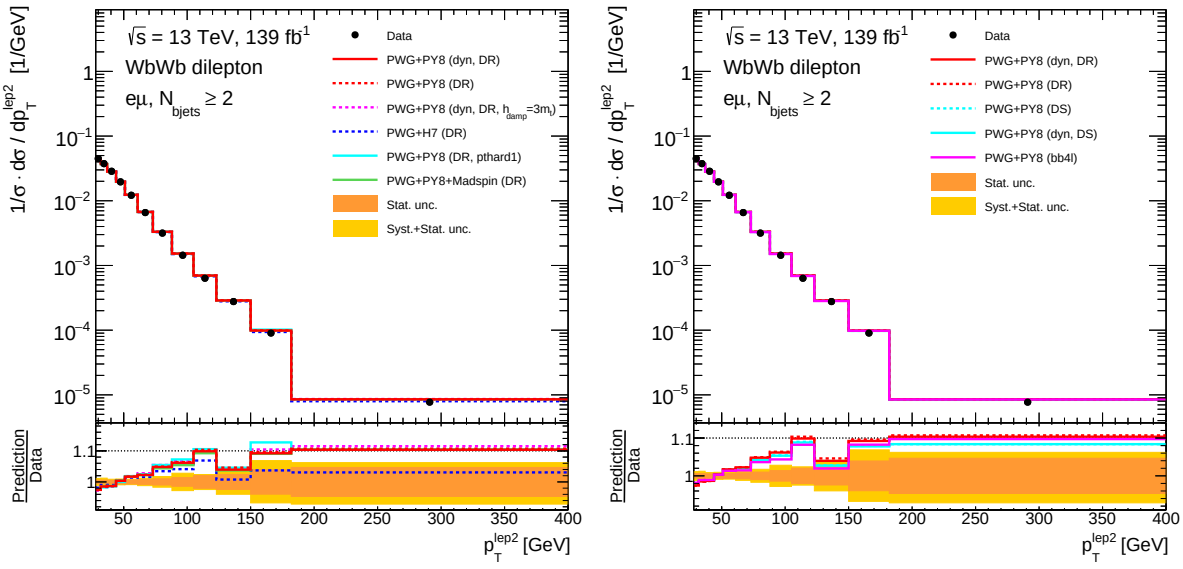

(a) (b)

Figure 5.15: The results of the unfolding procedure described for the relative differential cross-section measurement, as a function of the $p_{\mathrm{T}}^{\mathrm{lep},2}$ variable. The cross section is unfolded at particle level, in the fiducial phase-space. Data points are represented by black dots and are placed at the center of the corresponding bin. A comparison with several alternative predictions is provided, as listed in the box in the top panel. In the bottom panel, the ratio between predictions and data is shown. The orange band represents the statistical uncertainty, while the yellow band shows the combined statistical and systematic uncertainties. On the left hand side, predictions from different generators making use of the DR scheme are presented. On the right hand side, different schemes for the interference are considered, together with the $bb4l$ sample .

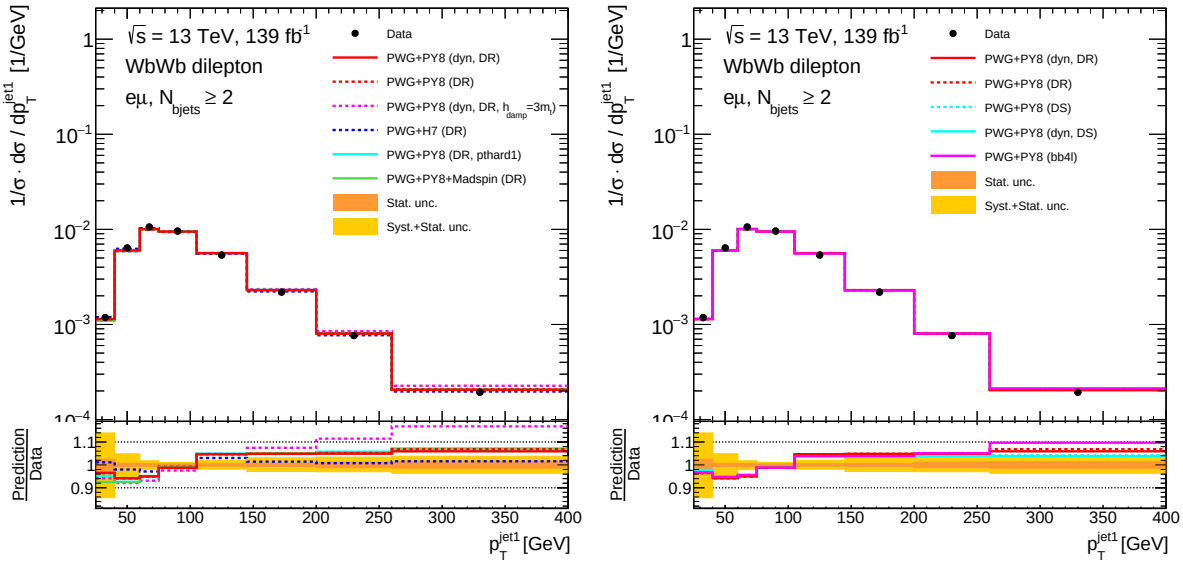

(a) (b)

Figure 5.16: The results of the unfolding procedure described for the relative differential cross-section measurement, as a function of the $p_{\mathrm{T}}^{\mathrm{jet},1}$ variable. The cross section is unfolded at particle level, in the fiducial phase-space. Data points are represented by black dots and are placed at the center of the corresponding bin. A comparison with several alternative predictions is provided, as listed in the box in the top panel. In the bottom panel, the ratio between predictions and data is shown. The orange band represents the statistical uncertainty, while the yellow band shows the combined statistical and systematic uncertainties. On the left hand side, predictions from different generators making use of the DR scheme are presented. On the right hand side, different schemes for the interference are considered, together with the $bb4l$ sample.

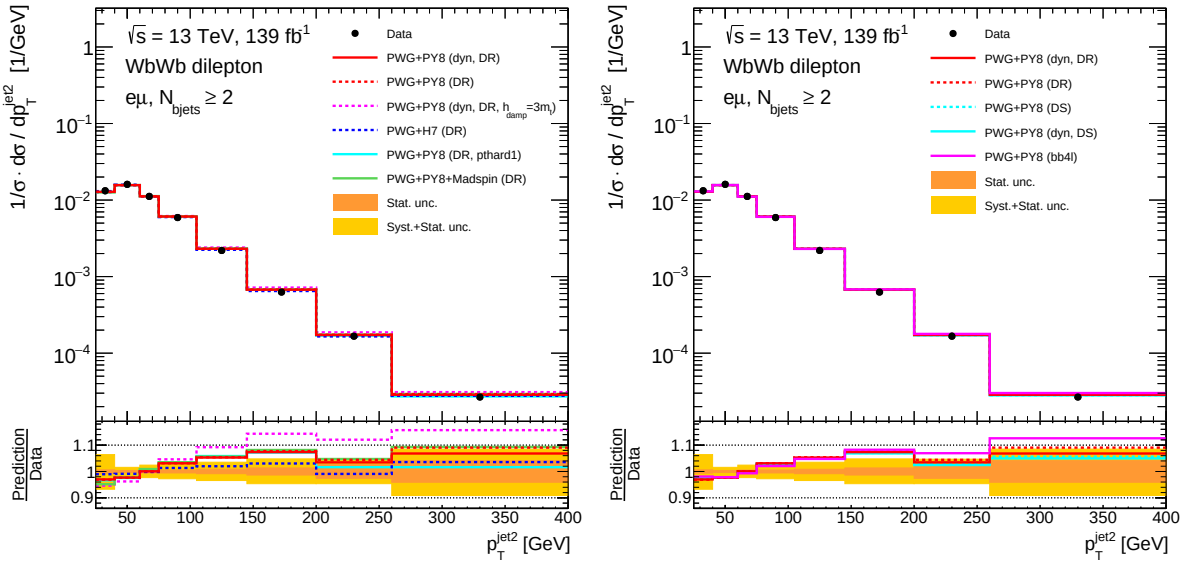

(a) (b)

Figure 5.17: The results of the unfolding procedure described for the relative differential cross-section measurement, as a function of the $p_{\mathrm{T}}^{\mathrm{jet},2}$ variable. The cross section is unfolded at particle level, in the fiducial phase-space. Data points are represented by black dots and are placed at the center of the corresponding bin. A comparison with several alternative predictions is provided, as listed in the box in the top panel. In the bottom panel, the ratio between predictions and data is shown. The orange band represents the statistical uncertainty, while the yellow band shows the combined statistical and systematic uncertainties. On the left hand side, predictions from different generators making use of the DR scheme are presented. On the right hand side, different schemes for the interference are considered, together with the $bb4l$ sample.

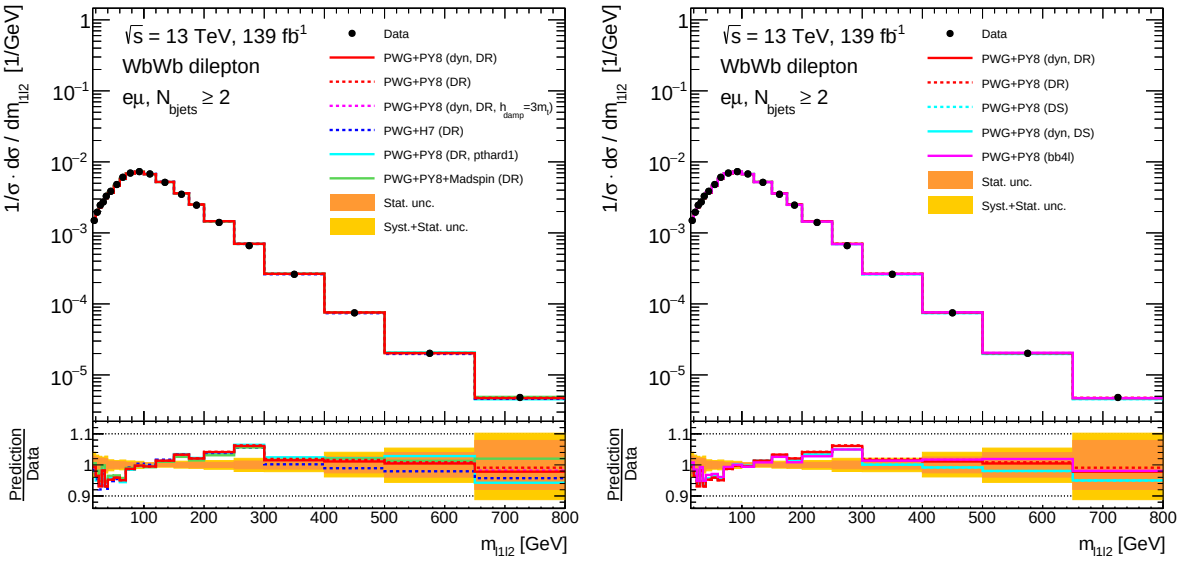

(a) (b)

Figure 5.18: The results of the unfolding procedure described for the relative differential cross-section measurement, as a function of the m_{l1l2} variable. The cross section is unfolded at particle level, in the fiducial phase-space. Data points are represented by black dots and are placed at the center of the corresponding bin. A comparison with several alternative predictions is provided, as listed in the box in the top panel. In the bottom panel, the ratio between predictions and data is shown. The orange band represents the statistical uncertainty, while the yellow band shows the combined statistical and systematic uncertainties. On the left hand side, predictions from different generators making use of the DR scheme are presented. On the right hand side, different schemes for the interference are considered, together with the *bb4l* sample.

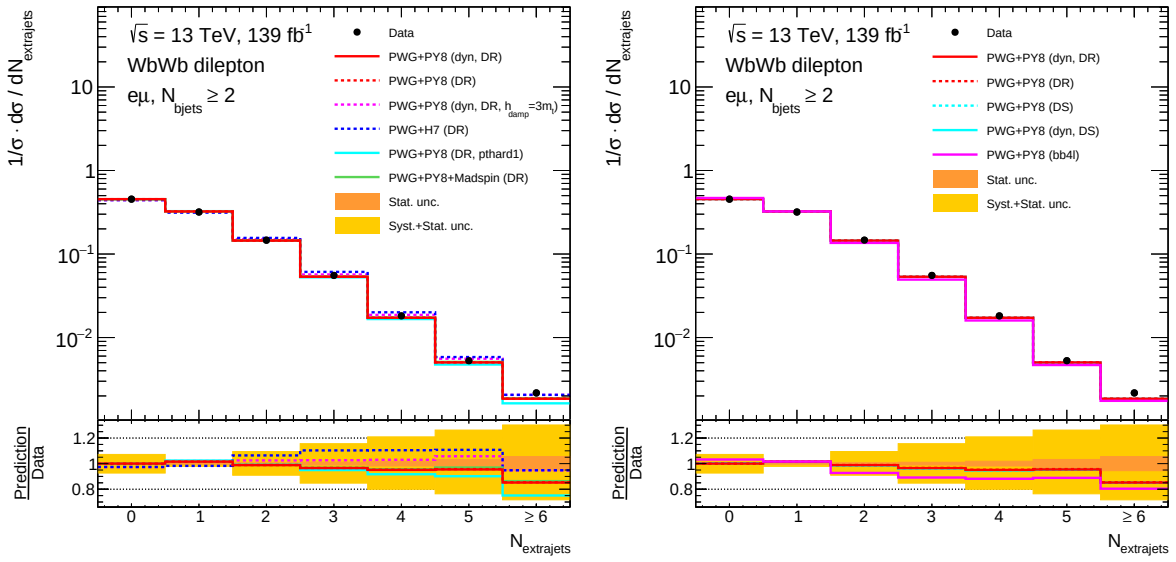

(a) (b)

Figure 5.19: The results of the unfolding procedure described for the relative differential cross-section measurement, as a function of the $N_{\text{extrajets}}$ variable. The cross section is unfolded at particle level, in the fiducial phase-space. Data points are represented by black dots and are placed at the center of the corresponding bin. A comparison with several alternative predictions is provided, as listed in the box in the top panel. In the bottom panel, the ratio between predictions and data is shown. The orange band represents the statistical uncertainty, while the yellow band shows the combined statistical and systematic uncertainties. On the left hand side, predictions from different generators making use of the DR scheme are presented. On the right hand side, different schemes for the interference are considered, together with the $bb4l$ sample.

Chapter 6

Conclusions

In this thesis, the measurement of the $WbWb$ differential cross section as a function of basic kinematic observables, namely $p_{\mathrm{T}}^{\mathrm{lep},1}$, $p_{\mathrm{T}}^{\mathrm{lep},2}$, $p_{\mathrm{T}}^{\mathrm{jet},1}$, $p_{\mathrm{T}}^{\mathrm{jet},2}$, m_{l1l2} and $N_{\mathrm{extrajets}}$, is provided. The measurement is performed using the full ATLAS dataset collected during Run-2, at a center of mass energy $\sqrt{s} = 13$ TeV and an integrated luminosity equal to 139 fb^{-1}. The result was obtain by considering the dilepton opposite sign (OS) channel, for final state leptons $e\mu$, which allowed to reduce the $Z \to ll$ background. Moreover, the obtained differential cross-sections were measured in a fiducial phase space defined according to the requirements introduced in chapter 4, section 4.3. The complete analysis strategy applied in the present thesis can be summarized in the following steps:

- Definition of the fiducial phase space and event selection;
- Control plot production;
- Determination of the systematic uncertainties involved in the measurement;
- Application of the Bayesian Iterative unfolding for the measurement of the differential cross section, as a function of the aforementioned basic kinematic variables;
- Unfolding validation via closure and stress tests;
- Evaluation of the agreement between the measurement and the available MC simulations calculating the χ^2;

The unfolding validation tests provided a good indication on the correctness of the unfolding procedure performed, as observed from the calculated χ^2 in both closure and stress tests.

Concerning the evaluation of the measurements-MC agreement, it was found that the subleading jet transverse momentum presents the best agreement with the predictions. Conversely, the worst agreement is observed when considering the measurement as a function of the leptons invariant mass. Among the available predictions, PWG+H7 is the one which better reproduces the measurements, as shown in tables 5.2 and 5.3. None of the simulations provide a good description of all measurements simultaneously.

An additional measurement of the total cross-section in the fiducial phase space was performed, obtaining

$$\sigma_{fid} = 5.97 \pm 0.01(\text{stat.})^{+0.30}_{-0.33}(\text{syst.})\text{pb}.$$

The choice adopted in the present thesis is to provide only the relative differential cross-section measurements, obtained by normalising the differential cross-section with the total one. This choice is motivated by the fact that many of the systematic uncertainties considered have a small effect on the shape of the distribution and can be cancelled by taking such ratio.

In conclusion, the $WbWb$ differential cross-section was correctly measured, as a function of several basic kinematic observables. Overall, the effect of the quantum interference between $t\bar{t}$ and tW is not as evident as in the dedicated ATLAS measurement, already published, which exploited specifically designed observables aiming to highlight said effect. The results shown in this work may have an impact in the process of future Monte Carlo validations and in constraining the $WbWb$ background in BSM searches, where it is relevant.

Appendix A

Stress tests

In the present appendix, complementing chapter 4, the remaining stress tests performed with the reweighting functions calculated from the $p_{\mathrm{T}}^{\mathrm{lep},1}$ and $p_{\mathrm{T}}^{\mathrm{jet},1}$ are presented, respectively, from figure A.1 to A.4.

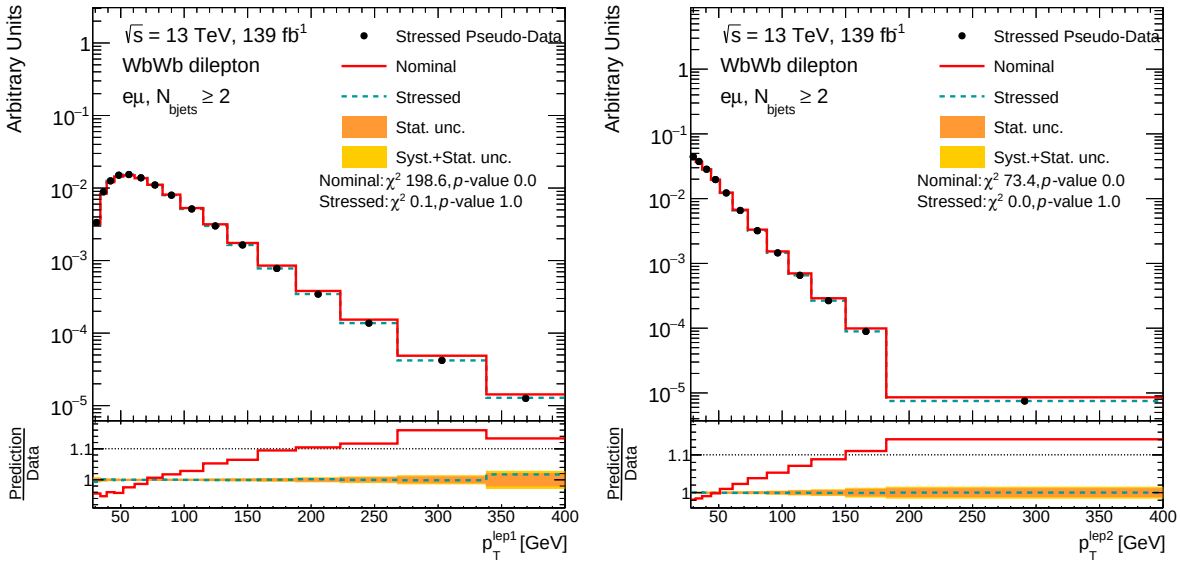

(a) (b)

Figure A.1: $p_{\mathrm{T}}^{\mathrm{lep},1}$ (a) and $p_{\mathrm{T}}^{\mathrm{lep},2}$ (b) variables, using a reweight function based on the $p_{\mathrm{T}}^{\mathrm{lep},1}$ variable distribution. A comparison between the stressed and nominal predictions is provided. In the bottom panel, the prediction/data ratio as a function of the variable is shown. The statistical and total uncertainty bands are shown in yellow and orange respectively.

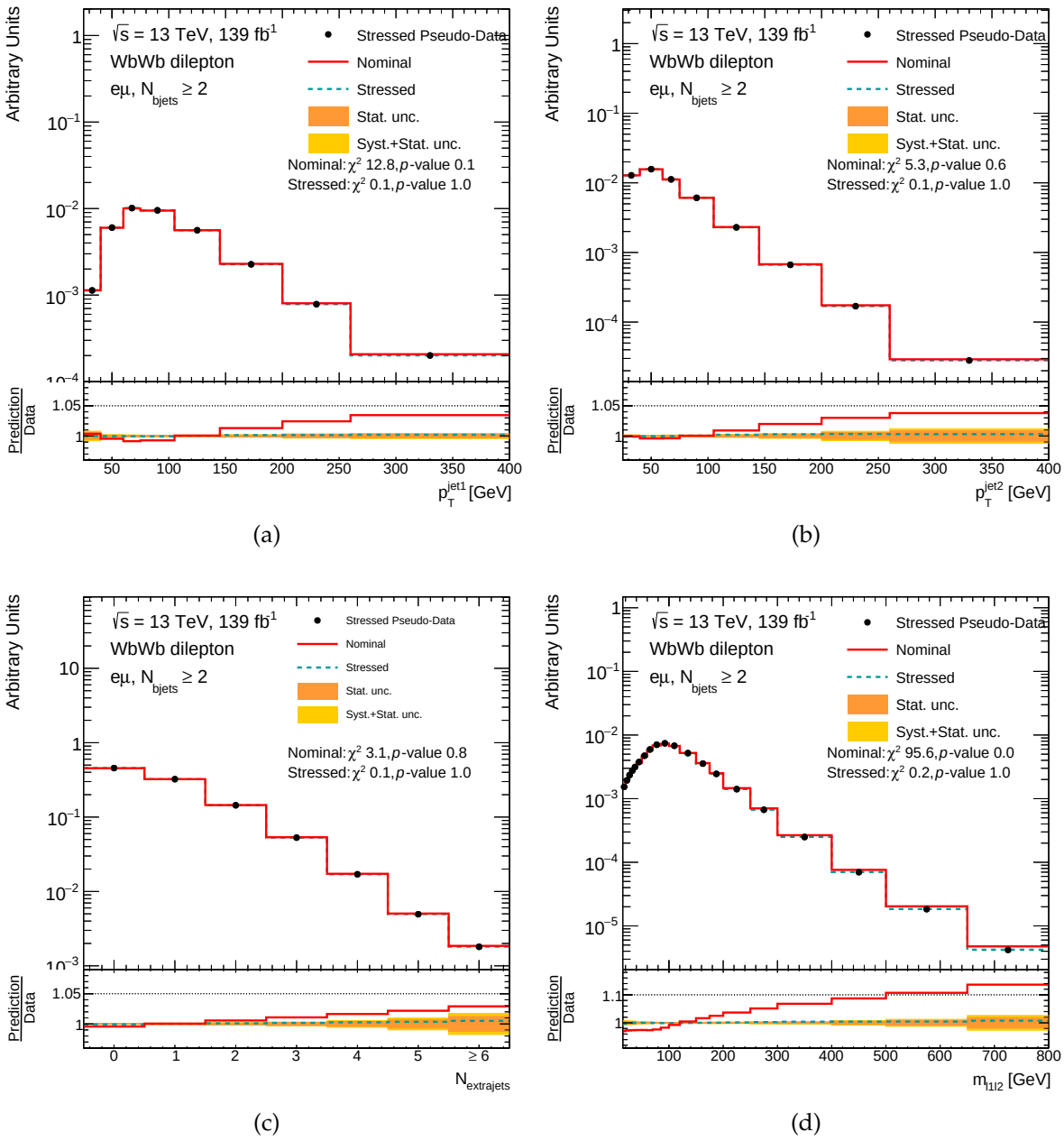

Figure A.2: $p_{\mathrm{T}}^{\mathrm{jet},1}$ (a) and $p_{\mathrm{T}}^{\mathrm{jet},2}$ (b), $N_{mathrmextrajets}$ (c) and m_{l1l2} (d) variables, using a reweight function based on the $p_{\mathrm{T}}^{\mathrm{lep},1}$ variable distribution. A comparison between the stressed and nominal predictions is provided. In the bottom panel, the prediction/data ratio as a function of the variable is shown. The statistical and total uncertainty bands are shown in yellow and orange respectively.

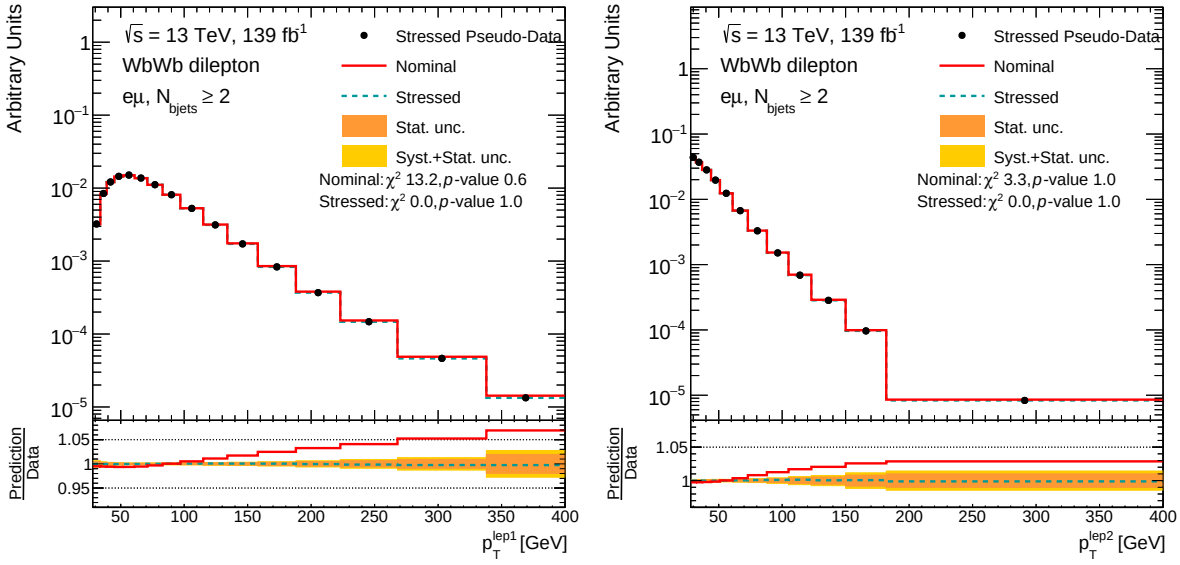

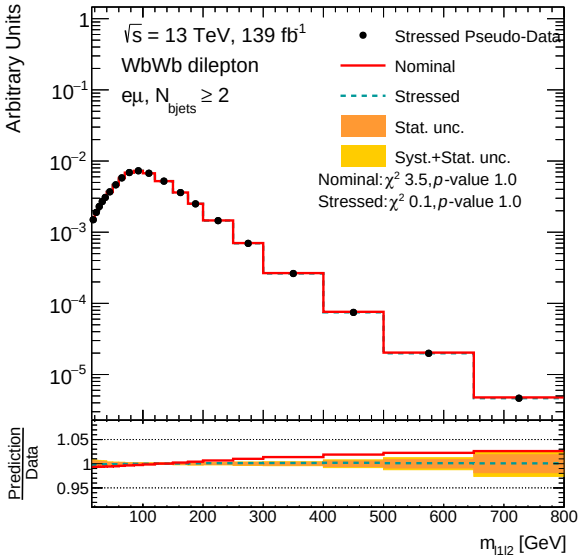

Figure A.3: $p_{\mathrm{T}}^{\mathrm{lep},1}$ (a) and $p_{\mathrm{T}}^{\mathrm{lep},2}$ (b) and (c) and m_{l1l2} variables, using a reweight function based on the $p_{\mathrm{T}}^{\mathrm{jet},1}$ variable distribution. A comparison between the stressed and nominal predictions is provided. In the bottom panel, the prediction/data ratio as a function of the variable is shown. The statistical and total uncertainty bands are shown in yellow and orange respectively.

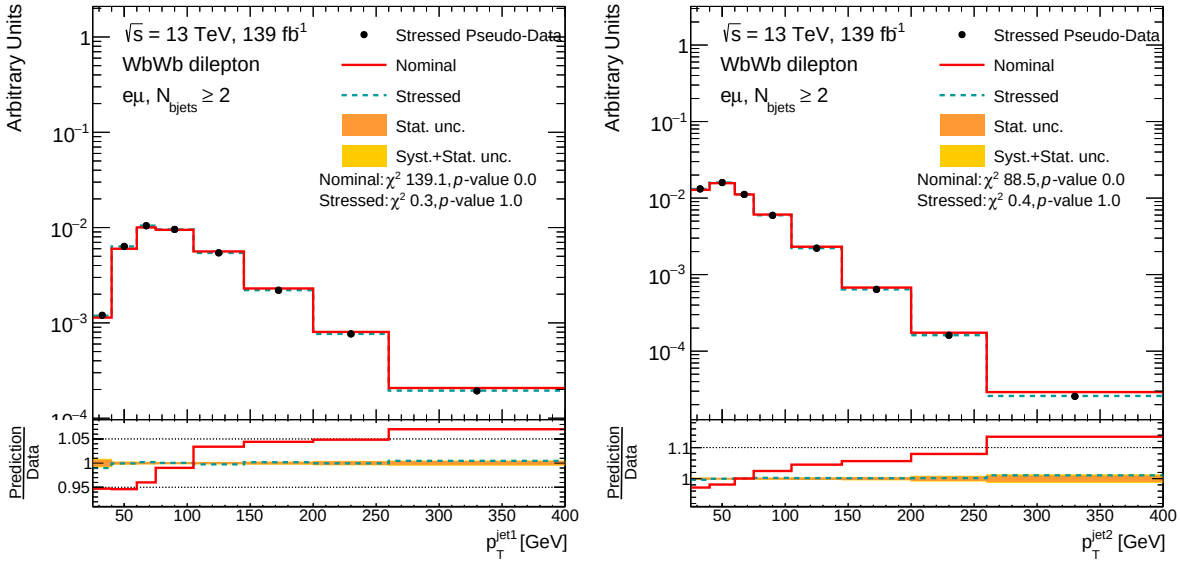

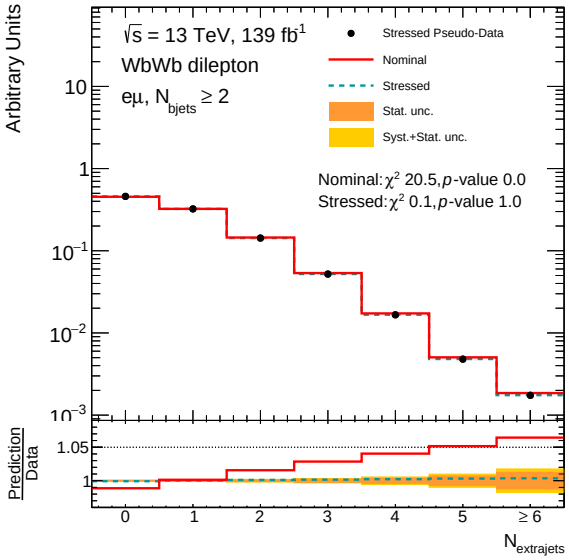

Figure A.4: $p_{\mathrm{T}}^{\mathrm{jet},1}$ (a) and $p_{\mathrm{T}}^{\mathrm{jet},2}$ (b), and $N_{mathrmextrajets}$ (c) variables, using a reweight function based on the $p_{\mathrm{T}}^{\mathrm{jet},1}$ variable distribution. A comparison between the stressed and nominal predictions is provided. In the bottom panel, the prediction/data ratio as a function of the variable is shown. The statistical and total uncertainty bands are shown in yellow and orange respectively.

Appendix B

Covariance and correlation matrices

In this appendix, the correlation and covariance matrices evaluated in the analysis are presented in figures B.1 to B.4. Correlation matrices were computed by applying:

$$Corr_{ij} = \frac{Cov_{ij}}{\sqrt{Cov_{ii} \cdot Cov_{jj}}}$$

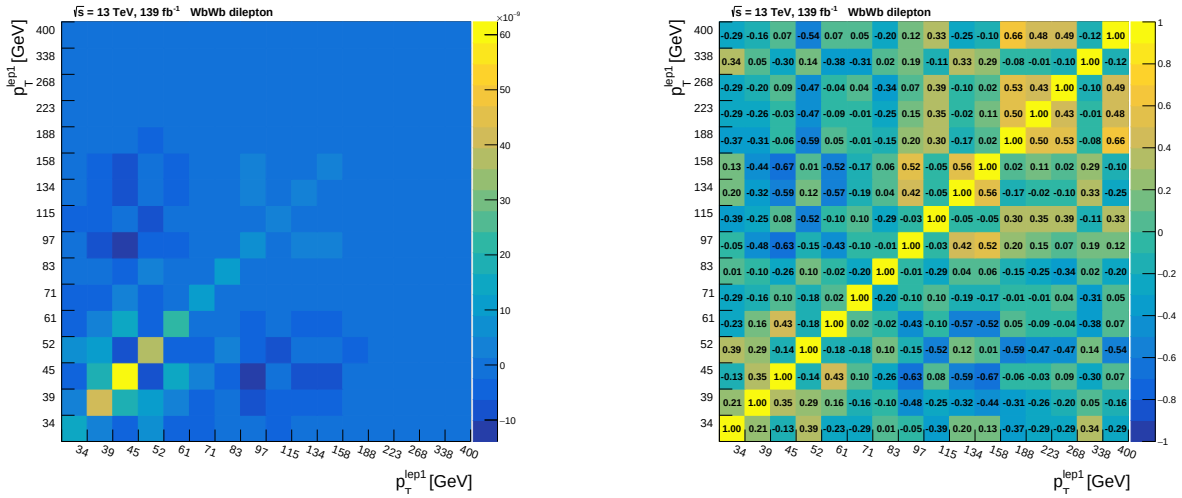

(a) (b)

Figure B.1: Covariance (a) and correlation (b) matrices for the relative differential cross section measurement, as a function of the $p_{\mathrm{T}}^{lep,1}$.

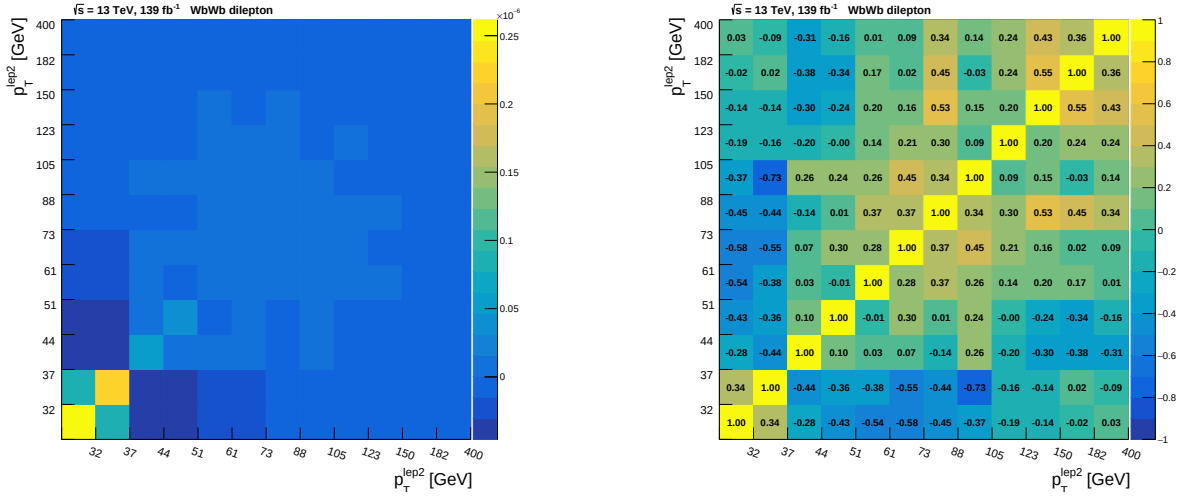

(a) (b)

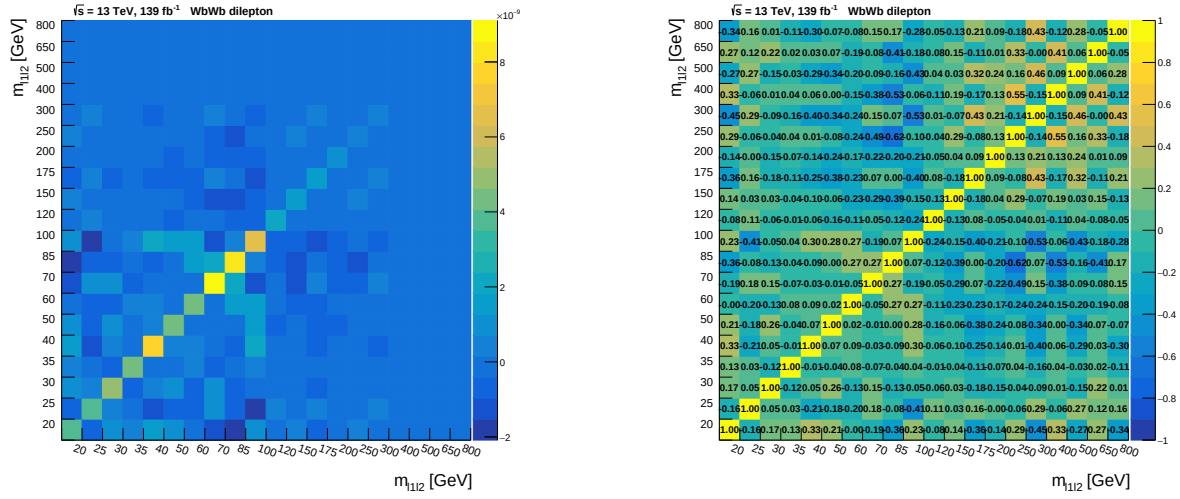

(c) (d)

Figure B.2: From left to right, top to bottom: Covariance and correlation matrices for the relative differential cross section measurement, as a function of the $p_{\mathrm{T}}^{lep,2}$ ((a) and (b)) and m_{l1l2} ((c) and (d)) variables.

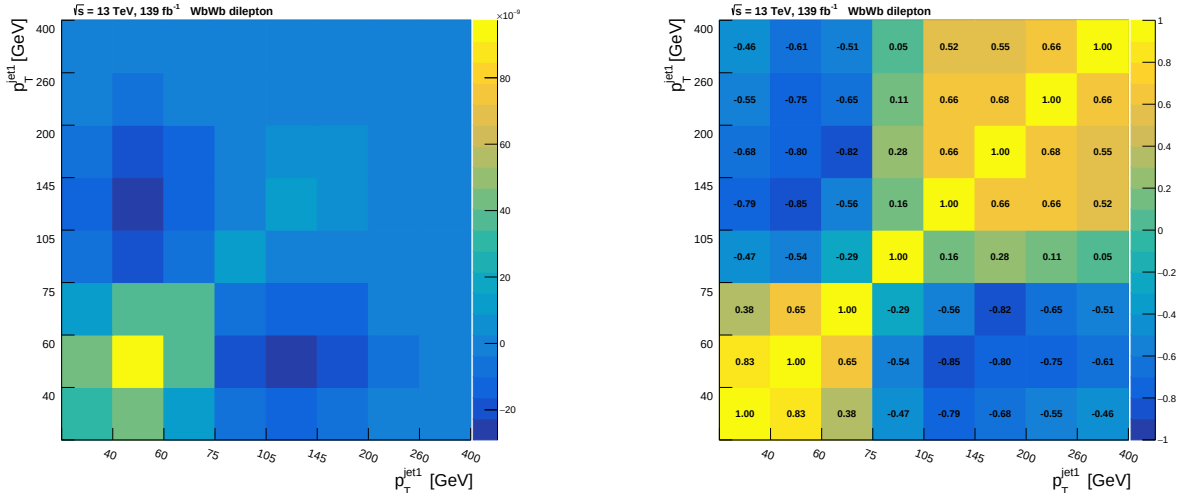

(a) (b)

(c) (d)

Figure B.3: From left to right, top to bottom: Covariance and correlation matrices for the relative differential cross section measurement, as a function of the $p_{\mathrm{T}}^{jet,1}$ ((a) and (b)) and $p_{\mathrm{T}}^{jet,2}$ ((c) and (d)) variables.

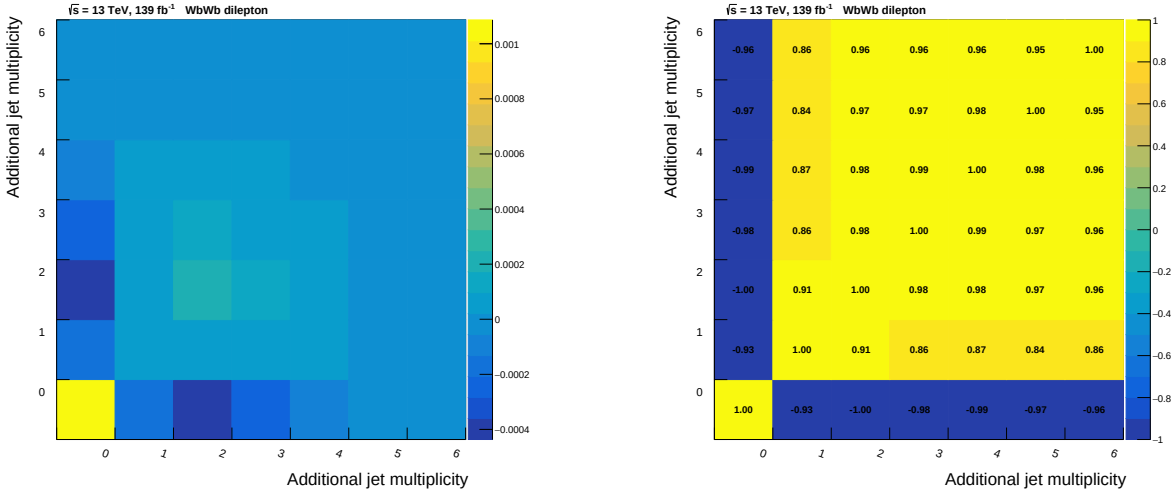

(a) (b)

Figure B.4: Covariance (a) and correlation (b) matrices for the relative differential cross section measurement, as a function of the $N_{\text{extrajets}}$ variable.

Bibliography

[1] The CDF collaboration, *Physical Review Letters* **1995**, *74*, 2626–2631.

[2] The DØ collaboration, *Physical Review Letters* **1995**, *74*, 2632–2637.

[3] The ATLAS Collaboration, *Journal of Instrumentation* **2008**, *3*, S08003–S08003.

[4] R.L. Workman et al, *PTEP* **2022**, *2022*, 083C01.

[5] P. Skands in Searching for New Physics at Small and Large Scales, WORLD SCIENTIFIC, **2013**.

[6] C. S. Wu, E. Ambler, R. W. Hayward, D. D. Hoppes, R. P. Hudson, *Phys. Rev.* **1957**, *105*, 1413–1415.

[7] M. Gallinaro, *Journal of Physics: Conference Series* **2013**, *447*, 012012.

[8] U. Husemann, *Progress in Particle and Nuclear Physics* **2017**, *95*, 48–97.

[9] Top working group cross-section summary plots, November 2022, tech. rep., Figure at https://atlas.web.cern.ch/Atlas/GROUPS/PHYSICS/PUBNOTES/ATL-PHYS-PUB-2022-051, CERN, Geneva, **2022**.

[10] S. Frixione, E. Laenen, P. Motylinski, C. White, B. R. Webber, *Journal of High Energy Physics* **2008**, *2008*, 029–029.

[11] M. Baak, J. Cúth, J. Haller, A. Hoecker, R. Kogler, K. Mönig, M. Schott, J. Stelzer, *The European Physical Journal C* **2014**, *74*, DOI 10.1140/epjc/s10052-014-3046-5.

[12] G. Degrassi, S. D. Vita, J. Elias-Miró, J. R. Espinosa, G. F. Giudice, G. Isidori, A. Strumia, *Journal of High Energy Physics* **2012**, *2012*, DOI 10.1007/jhep08(2012)098.

[13] M. C. Smith, S. S. Willenbrock, *Phys. Rev. Lett.* **1997**, *79*, 3825–3828.

[14] Zyla P. A. et al (Particle Data Group), *Progress of Theoretical and Experimental Physics* **2020**, *2020*, 083C01, DOI 10.1093/ptep/ptaa104.

[15] The ATLAS collaboration, *Eur. Phys. J. C*, DOI https://doi.org/10.1140/epjc/s10052-020-8181-6.

[16] A. Denner, S. Dittmaier, S. Kallweit, S. Pozzorini, *Physical Review Letters* **2011**, *106*, DOI 10.1103/physrevlett.106.052001.

[17] G. Bevilacqua, M. Czakon, A. van Hameren, C. G. Papadopoulos, M. Worek, *Journal of High Energy Physics* **2011**, *2011*, DOI 10.1007/jhep02(2011)083.

[18] G. Heinrich, A. Maier, R. Nisius, J. Schlenk, J. Winter, *Journal of High Energy Physics* **2014**, *2014*, DOI 10.1007/jhep06(2014)158.

[19] F. Cascioli, S. Kallweit, P. Maierhöfer, S. Pozzorini, *The European Physical Journal C* **2014**, *74*, DOI 10.1140/epjc/s10052-014-2783-9.

[20] F. Demartin, B. Maier, F. Maltoni, K. Mawatari, M. Zaro, *Eur. Phys. J. C* **2017**, *77*, 34.

[21] C. D. White, S. Frixione, E. Laenen, F. Maltoni, *JHEP* **2009**, *11*, 074.

[22] The ATLAS collaboration, *Phys. Rev. Lett.* **2018**, *121*, 152002.

[23] G. Bianco, **2021**, DOI 10.1393/ncc/i2022-22002-3.

[24] L. Evans, P. Bryant, *Journal of Instrumentation* **2008**, *3*, S08001–S08001.

[25] CERN, The accelerator complex, https://home.cern/science/accelerators/accelerator-complex.

[26] Xabier Cid Vidal, Ramon Cid Manzano, Taking a closer look at LHC: LHC Pb collisions, https://www.lhc-closer.es/taking_a_closer_look_at_lhc/0.lhc_pb_collisions.

[27] L. Evans, *Annual Review of Nuclear and Particle Science* **2011**, *61*, 435–466.

[28] CERN, A vacuum as empty as interstellar space, https://home.cern/science/engineering/vacuum-empty-interstellar-space.

[29] CERN, High-Luminosity LHC, https://home.cern/science/accelerators/high-luminosity-lhc.

[30] The ALICE Collaboration, *Journal of Instrumentation* **2008**, *3*, S08002–S08002.

[31] The CMS Collaboration, *Journal of Instrumentation* **2008**, *3*, S08004–S08004.

[32] A. A. Alves, Jr. et al., *JINST* **2008**, *3*, S08005.

[33] CERN, The HL-LHC project, https://hilumilhc.web.cern.ch/content/hl-lhc-project.

[34] P. L. Rocca, F Riggi, *Journal of Physics: Conference Series* **2014**, *515*, 012012.

[35] J. T. Boyd, *CERN Yellow Rep. School Proc.* **2022**, *5*, (Eds.: C. Duhr, M. Mulders), 247.

[36] CERN, ATLAS, https://home.cern/science/experiments/atlas.

[37] J. Pequenao, "Computer generated image of the whole ATLAS detector", **2008**.

[38] CERN, ATLAS magnet system, https://atlas.cern/Discover/Detector/Magnet-System.

[39] The ATLAS collaboration, *JINST* **2019**, *14*, P09011. 36 p.

[40] The ATLAS collaboration, *The European Physical Journal C* **2016**, *76*, DOI 10.1140/epjc/s10052-016-4120-y.

[41] P. Hamal, Physics prospects with the ALFA and AFP detectors, tech. rep., **2013**.

[42] G Avoni, M Bruschi, G Cabras, D Caforio, N Dehghanian, A Floderus, B Giacobbe, F Giannuzzi, F Giorgi, P Grafström, V Hedberg, F Lasagni Manghi, S Meneghini, J Pinfold, E Richards, C Sbarra, N Semprini Cesari, A Sbrizzi, R Soluk, G Ucchielli, S Valentinetti, O Viazlo, M Villa, C Vittori, R Vuillermet, A Zoccoli, *JINST* **2018**, *13*, P07017. 33 p.

[43] L Adamczyk, E Banaś, A Brandt, M Bruschi, S Grinstein, J Lange, M Rijssenbeek, P Sicho, R Staszewski, T Sykora, M Trzebiński, J Chwastowski, K Korcyl, Technical Design Report for the ATLAS Forward Proton Detector, tech. rep., **2015**.

[44] S. Abdel Khalek et al, *Journal of Instrumentation* **2016**, *11*, P11013–P11013.

[45] The ATLAS collaboration, *The European Physical Journal C* **2017**, *77*, DOI 10.1140/epjc/s10052-017-4852-3.

[46] P. Jenni, M. Nessi, M. Nordberg, K. Smith, *ATLAS high-level trigger, data-acquisition and controls: Technical Design Report*, CERN, Geneva, **2003**.

[47] The ATLAS collaboration, *Journal of Instrumentation* **2020**, *15*, P10004–P10004.

[48] The ATLAS collaboration, *The European Physical Journal C* **2017**, *77*, DOI 10.1140/epjc/s10052-017-5225-7.

[49] R. Frühwirth, *Nuclear Instruments and Methods in Physics Research Section A: Accelerators Spectrometers Detectors and Associated Equipment* **1987**, *262*, 444–450.

[50] T Cornelissen, M Elsing, I Gavrilenko, W Liebig, E Moyse, A Salzburger, *Journal of Physics: Conference Series* **2008**, *119*, 032014.

[51] The ATLAS collaboration, *The European Physical Journal C* **2017**, *77*, DOI 10.1140/epjc/s10052-017-4887-5.

[52] The ATLAS collaboration, *The European Physical Journal C* **2019**, *79*, DOI 10.1140/epjc/s10052-019-7140-6.

[53] The ATLAS collaboration, *Journal of Instrumentation* **2019**, *14*, P12006.

[54] R. Ospanov, R. T. Roberts, T. R. Wyatt, Tagging non-prompt electrons and muons, tech. rep., CERN, Geneva, **2016**.

[55] The ATLAS collaboration, *The European Physical Journal C* **2016**, *76*, DOI 10.1140/epjc/s10052-016-4120-y.

[56] The ATLAS collaboration, *Eur. Phys. J. C* **2021**, *81*, 578.

[57] S. Rettie, Muon identification and performance in the ATLAS experiment, tech. rep., CERN, Geneva, **2018**.

[58] M. Cacciari, G. P. Salam, G. Soyez, *Journal of High Energy Physics* **2008**, *2008*, 063–063.

[59] The ATLAS collaboration, *The European Physical Journal C* **2017**, *77*, DOI 10.1140/epjc/s10052-017-5031-2.

[60] The ATLAS collaboration, *The European Physical Journal C* **2016**, *76*, DOI 10.1140/epjc/s10052-016-4395-z.

[61] Tagging and suppression of pileup jets with the ATLAS detector, tech. rep., CERN, Geneva, **2014**.

[62] The ATLAS collaboration, *Eur. Phys. J. C* **2021**, *81*, 689.

[63] The ATLAS collaboration, *The European Physical Journal C* **2019**, *79*, DOI 10.1140/epjc/s10052-019-7450-8.

[64] Optimisation and performance studies of the ATLAS *b*-tagging algorithms for the 2017-18 LHC run, tech. rep., CERN, Geneva, **2017**.

[65] The ATLAS Collaboration, ATLAS flavour-tagging algorithms for the LHC Run 2 *pp* collision dataset, **2022**.

[66] S. Agostinelli et al., *Nucl. Instrum. Meth. A* **2003**, *506*, 250–303.

[67] S. Frixione, G. Ridolfi, P. Nason, *Journal of High Energy Physics* **2007**, *2007*, 126–126.

[68] P. Nason, *Journal of High Energy Physics* **2004**, *2004*, 040–040.

[69] S. Frixione, P. Nason, C. Oleari, *Journal of High Energy Physics* **2007**, *2007*, 070–070.

[70] S. Alioli, P. Nason, C. Oleari, E. Re, *Journal of High Energy Physics* **2010**, *2010*, DOI 10.1007/jhep06(2010)043.

[71] R. D. Ball, V. Bertone, S. Carrazza, C. S. Deans, L. D. Debbio, S. Forte, A. Guffanti, N. P. Hartland, J. I. Latorre, J. Rojo, M. Ubiali, *Journal of High Energy Physics* **2015**, *2015*, DOI 10.1007/jhep04(2015)040.

[72] ATLAS Pythia 8 tunes to 7 TeV data, tech. rep., CERN, Geneva, **2014**.

[73] R. D. Ball, V. Bertone, S. Carrazza, C. S. Deans, L. D. Debbio, S. Forte, A. Guffanti, N. P. Hartland, J. I. Latorre, J. Rojo, M. Ubiali, *Nuclear Physics B* **2013**, *867*, 244–289.

[74] D. J. Lange, *Nuclear Instruments and Methods in Physics Research Section A: Accelerators Spectrometers Detectors and Associated Equipment* **2001**, *462*, BEAUTY2000, Proceedings of the 7th Int. Conf. on B-Physics at Hadron Machines, 152–155.

[75] M. Czakon, A. Mitov, *Computer Physics Communications* **2014**, *185*, 2930–2938.

[76] J. Butterworth, S. Carrazza, A. Cooper-Sarkar, A. D. Roeck, J. Feltesse, S. Forte, J. Gao, S. Glazov, J. Huston, Z. Kassabov, R. McNulty, A. Morsch, P. Nadolsky, V. Radescu, J. Rojo, R. Thorne, *Journal of Physics G: Nuclear and Particle Physics* **2016**, *43*, 023001.

[77] E. Re, *The European Physical Journal C* **2011**, *71*, DOI 10.1140/epjc/s10052-011-1547-z.

[78] N. Kidonakis, *Physical Review D* **2010**, *82*, DOI 10.1103/physrevd.82.054018.

[79] M. Czakon, D. Heymes, A. Mitov, *Journal of High Energy Physics* **2017**, *2017*, DOI 10.1007/jhep04(2017)071.

[80] J. Bellm, S. Gieseke, D. Grellscheid, S. Plätzer, M. Rauch, C. Reuschle, P. Richardson, P. Schichtel, M. H. Seymour, A. Siódmok, A. Wilcock, N. Fischer, M. A. Harrendorf, G. Nail, A. Papaefstathiou, D. Rauch, *The European Physical Journal C* **2016**, *76*, DOI 10.1140/epjc/s10052-016-4018-8.

[81] M. Bähr, S. Gieseke, M. A. Gigg, D. Grellscheid, K. Hamilton, O. Latunde-Dada, S. Plätzer, P. Richardson, M. H. Seymour, A. Sherstnev, B. R. Webber, *The European Physical Journal C* **2008**, *58*, 639–707.

[82] M. H. Seymour, A. Siódmok, *Journal of High Energy Physics* **2013**, *2013*, DOI 10.1007/jhep10(2013)113.

[83] L. A. Harland-Lang, A. D. Martin, P. Motylinski, R. S. Thorne, **2015**, *75*, DOI 10.1140/epjc/s10052-015-3397-6.

[84] P. Artoisenet, R. Frederix, O. Mattelaer, R. Rietkerk, *Journal of High Energy Physics* **2013**, *2013*, DOI 10.1007/jhep03(2013)015.

[85] T. Ježo, J. M. Lindert, P. Nason, C. Oleari, S. Pozzorini, *The European Physical Journal C* **2016**, *76*, DOI 10.1140/epjc/s10052-016-4538-2.

[86] T Gleisberg, S Höche, F Krauss, M Schönherr, S Schumann, F Siegert, J Winter, *Journal of High Energy Physics* **2009**, *2009*, 007–007.

[87] S. Höche, F. Krauss, M. Schönherr, F. Siegert, *Journal of High Energy Physics* **2012**, *2012*, DOI 10.1007/jhep09(2012)049.

[88] F. Cascioli, P. Maierhöfer, S. Pozzorini, *Physical Review Letters* **2012**, *108*, DOI 10.1103/physrevlett.108.111601.

[89] M. Cacciari, G. P. Salam, G. Soyez, *Journal of High Energy Physics* **2008**, *2008*, 005–005.

[90] G. Cowan, *Conf. Proc. C* **2002**, *0203181*, (Eds.: M. R. Whalley, L. Lyons), 248–257.

[91] G. Cowan, *Statistical Data Analysis*, OUP, **1998**.

[92] M. Romano, *Measurement of the differential cross section of $t\bar{t}$ pairs in pp collision at $\sqrt{s} = 7$ TeV with the ATLAS detector at the LHC*, **2013**.

[93] G. D'Agostini, A multidimensional unfolding method based on Bayes' Theorem, tech. rep., DESY, Hamburg, **1994**.

[94] L. Brenner, R. Balasubramanian, C. Burgard, W. Verkerke, G. Cowan, P. Verschuuren, V. Croft, *International Journal of Modern Physics A* **2020**, *35*, 2050145.

[95] The ATLAS collaboration, *Journal of Instrumentation* **2019**, *14*, P12006–P12006.

[96] The ATLAS collaboration, *The European Physical Journal C* **2016**, *76*, DOI 10.1140/epjc/s10052-016-4120-y.

[97] Tagging and suppression of pileup jets with the ATLAS detector, tech. rep., CERN, Geneva, **2014**.

[98] Studies on top-quark Monte Carlo modelling with Sherpa and MG5_aMC@NLO, tech. rep., CERN, Geneva, **2017**.

[99] ATLAS simulation of boson plus jets processes in Run 2, tech. rep., CERN, Geneva, **2017**.

[100] Luminosity determination in pp collisions at $\sqrt{s} = 13$ TeV using the ATLAS detector at the LHC, tech. rep., CERN, Geneva, **2019**.

[101] F. Halzen, A. D. Martin, *Quarks and Leptons: An Introductory Course in Modern Particle Physics*, **1984**.

[102] C. Quigg, *Gauge Theories of the Strong, Weak, and Electromagnetic Interactions: Second Edition*, Princeton University Press, **2013**.

[103] M. Thomson, *Modern particle physics*, Cambridge University Press, **2013**.